UNIVERSIDADE FEDERAL DE PERNAMBUCO
CENTRO DE TECNOLOGIA E GEOCIÊNCIAS
DEPARTAMENTO DE OCEANOGRAFIA
PROGRAMA DE PÓS-GRADUAÇÃO EM OCEANOGRAFIA

Thiago Luiz do Vale Silva

Ocean-atmosphere processes and easterly waves in the generation and development of extreme events in the Eastern Northeast of Brazil

Recife

2018

Thiago Luiz do Vale Silva

Ocean-atmosphere processes and easterly waves in the generation and development of extreme events in the Eastern Northeast of Brazil

Thesis presented to the postgraduate program in oceanography of the Departmento of Oceanography of the Federal University of Pernambuco, as a requirement to obtain a doctorate degree in oceanography.

Main area: Abiotic Oceanography.

Supervisor: Prof. Dr^{a}. Dóris Regina Aires Veleda

Recife

2018

Catalogação na fonte
Bibliotecária Maria Luiza de Moura Ferreira, CRB-4 / 1469

S586o Silva,Thiago Luiz do Vale.
Ocean-atmosphere processes and easterly waves in the generation and development of extreme events in the Eastern Northeast of Brazil/Thiago Luiz do Vale - 2018.
102folhas, il.;tab., abr., sigl. e simb.

Orientadora: Profª.Drª. Dóris Regina Aires Veleda.
Tese (Doutorado) – Universidade Federal de Pernambuco. CTG.Programa de Pós-graduação em Oceanografia, 2018.
Inclui Referências.
Texto em inglês.

1.Oceanografia.2. Camada limite atmosférica marinha.3.Camada de inversão térmica dos ventos Alísios.4. Piscinas quentes do Atlântico tropical sul (SAWP).I.Veleda,Dóris Regina Aires(Orientadora).II. Título.

UFPE

551.46CDD (22. ed.) BCTG/2018-271

Thiago Luiz do Vale Silva

Ocean-atmosphere processes and easterly waves in the generation and development of extreme events in the Eastern Northeast of Brazil

Thesis presented to the postgraduate program in oceanography of the Departmento of Oceanography of the Federal University of Pernambuco, as a requirement to obtain a doctorate degree in oceanography.

Work approved. Recife, 26 March 2018:

Dóris Regina Aires Veleda
Supervisor

Carmen Medeiros Limongi

Rita Marques Alves

Washington Luiz Félix Correia Filho

Gbekpo Aubains Hounsou-gbo

Recife
2018

Dedico à minha família e em memória de Marta Guimarães

ACKNOWLEDGEMENTS

I thank to my family who gave me all kinds of educational, financial and affectionate supports.

I thank to my parents and grandmother for moral, disciplinary and human constitution that I have.

To my wife Elis Guimarães for all your love and companionship at all times, whether bad or good.

To my advisor Profa. Dr. Dóris Veleda, for the teachings and guidance during doctorate. And thank you for the opportunity and trust.

To the Prof. Dr. Moacyr Araújo for his guidance.

To the Prof. Dr. Alexandre Costa (CER) for the trust and opportunity in the participation of the projects and in the computational supports.

To HPC4E - High Performace Computing for Energy Program project for the opportunity to expand my vision as a researcher.

To the friend Dr. Pedro Tyançã for the talks, advice and for offering his computer "state of the art" to carry out the experiences of this thesis.

To my colleagues, who in bad times, raised my self-esteem.

To the friends, who in bad times always raised my self-esteem.

To the teachers from DOCEAN.

To the colleagues from DOCEAN.

Patrice Oliveira, APAC's manager, who helped me during the doctoral period.

To GMMC / APAC colleagues in the days of struggle, of joy, of sadness, each in his own way, but all together and mixed together.

My great thanks to everyone.

"Sempre em Frente!"

The author.

ABSTRACT

The coupled ocean-atmosphere wave and sediments transport (COAWST) model was used to simulate periods with intense rainfalls events at the eastern Northeast Brazil (ENEB). The simulations aimed to investigate the ocean-atmospheric interaction under Easterlies Waves Disturbances (EWD) conditions, which lead to intense rainfalls events over the ENEB. In June 2010 the sea surface temperature (SST) was warmer than 28.5 °C, in the western tropical South Atlantic (WTSA), with persistent anomalies above 1 °C, characterizing a southern Atlantic warm pool (SAWP). The sensible and latent heat fluxes acted to moisten the lower troposphere and affect the height of trade winds inversion layer (TWIL). The meteorological system, that occurred in low to medium levels during the period, favored the weakening, even to a break of the TWIL. These atmospheric disturbances were associated to convergence, cyclonic vorticity and upward water vapor motion to the medium troposphere levels. The disturbances when reached the ENEB coast, favored the convection and the intense rainfall over the region. The vertical structure of Marine Atmospheric Boundary Layer (MABL) was a key factor to triggering the occurrence of these synoptic activities with a deep convection. The sea-air interaction is important for understanding the climatic variability, due to heat, momentum and moisture exchange. Therefore the SAWP region is an important region to increasing meteorological systems over ENEB leading the variability and intense episodes of rainfall. In this work it was performed experiments with the Weather Research and Forecasting (WRF) and Regional Oceanic Model System (ROMS) in a two-way coupled mode. The goal was verify the improvements of coupled models in forecasting and characterizing the interactions between the ocean-atmosphere dynamics under different SAWP conditions which led intense rainfalls at the ENEB. The results evidenced the importance of the application of ocean-atmosphere coupled models in forecasting improvement compared to only atmospheric models, also the SAWP presented direct influence in the ENEB intense rainfall.

Keywords: Marine atmospheric boundary layer. Trade winds inversion layers. Southern Atlantic warm pool (SAWP).

RESUMO

O modelo coupled ocean-atmosphere wave and sediments transport (COAWST) foi utilizado para simular períodos de eventos intensos de precipitação sobre o leste do Nordeste Brasileiro (ENEB). As simulações tiveram como objetivo investigar as interações oceânicas e atmosféricas em condições de Distúrbios Ondulatórios de Leste (DOLs) os quais ocasionaram precipitações intensas no ENEB. Em junho de 2010 a temperatura superficial do mar (SST) registrada esteve acima de 28.5 °C, representando uma warm pool no Atlântico tropical sul (SAWP). Os calores sensíveis e latente agiram para umidificar anomalamente a baixa troposfera e afetar a altura da base das inversões térmicas dos Alísios (TWIL). O sistema meteorológico, o qual ocorreu de baixos a médios níveis durante o período, favoreceu o enfraquecimento, até a possível quebra da TWIL. Os DOLs são associadas a convergência, vorticidade ciclônica e vapor de água ascendente para a média troposfera. Os distúrbios ao chegar sobre a costa do ENEB, favoreceu convecção e precipitações extremas sobre a região. A estrutura vertical da Camada Limite Atmosférica Marinha (MABL) foi um fator chave para o gatilho da convecção profunda sobre a região. O entendimento sobre a interação oceano-atmosfera é importante para entender as variabilidades climáticas, devido aos fluxos de calor, momento e umidade. Portanto a região da SAWP é uma importante região para o aumento na intensidade dos sistemas meteorológicos sobre o ENEB gerando variabilidades climáticas e intensos episódios de chuvas. Neste trabalho foram feitas simulações com os modelos Weather Research and Forecasting (WRF) e o Regional Oceanic Model System (ROMS) em um modo acoplado em two-way. O objetivo foi avaliar o aperfeiçoamento das previsões e a analizar as características dinâmicas das interações entre oceano e atmosfera sobre diferentes condições na SAWP as quais levaram a intensas precipitações no ENEB. Os resultados mostraram um melhoramento das resoluções numéricas das previsões com modelos acoplados, ainda pôde observar influências diretas da SAWP nos eventos intensos de chuva.

Palavras-chave: Camada limite atmosférica marinha. Camada de inversão térmica dos ventos Alísios. Piscinas quentes do Atlântico tropical sul (*SAWP*).

LIST OF FIGURES

LIST OF TABLES

LIST OF ABBREVIATIONS AND ACRONYMS

AD	Atlantic Dipole
AESA	*Agência Executiva de Gestão das Águas da Paraíba*
AGC	Atmospheric Global Circulation
APAC	*Agência Pernambucana de Águas e Clima*
ARW	Advanced Research in WRF
AVHRR	Advanced Very High-Resolution Radiometer
CNEB	Central Northeast Brazil
COARE	Coupled Ocean-Atmosphere Response Experiment
COAWST	Coupled Ocean-Atmosphere-Wave-Sediment Transport
CPTEC	*Centro de Previsão do Tempo e Estudos Climáticos*
cSEC	Central South Equatorial Current
CSET	Cloud Systems Evolution in the Trades
DCP	Data Collect Platform
EMPARN	*Empresa de Pesquisa Agropecuária do Rio Grande do Norte*
ENEB	Eastern Northeast Brazil
EUMETSAT	European Organisation for the Exploitation of Meteorological Satellites
EWD	Easterly Wave Disturbance
FNL	(Final) Operational Global Analysis Data
GOES	Geostationary Operational Environmental Satellite
INEMA	*Instituto do Meio Ambiente e Recursos Hídricos*
INMET	*Instituto Nacional de Meteorologia*
INPE	*Instituto Nacional de Pesquisas Espaciais*
ITCZ	Inter Tropical Convergence Zone
LSM	Land Soil Model

MABL	Marine Atmospheric Boundary Layer
MCT	Model Coupling Toolkit
MMAB	Marine Modeling and Analysis Branch
MPI	Message Passing Interface
MYNN	Mellor-Yamada Nino Nakanishi
NBC	North Brazilian Current
NBCR	North Brazil Current Retroflection
NBUC	North Brazilian Undercurrent
NCEI	National Center for Environmental Information
NCEP	National Centers for Environmental Prediction
NEB	Northeast Brazil
NNEB	Northern Northeast Brazil
NOAA	National Oceanic and Atmospheric Administration
nSEC	Northern South Equatorial Current
OML	Ocean Moisture Layer
PBL	Planetary Boundary Layer
PIRATA	Prediction and Research Moored Array in the Tropical Atlantic
ROMS	Regional Oceanic Model System
RRTMG	Rapid Radiative Transfer Model
RTG-SST	Real-time, global, sea surface temperature
SACZ	Southern Atlantic Convergence Zone
SAWP	Southern Atlantic Warm Pool
SEC	Southern Equatorial Current
SF	Surface Physics
sSEC	Southern South Equatorial Current
SNEB	Southern Northeast Brazil

SST	Sea Surface Temperature
TSA	Tropical South Atlantic
TWIL	Trade Winds Inversion Layer
UTCV	Upper Troposphere Cyclonic Vortex
WPS	WRF preprocessing system
WRF	Weather Research and Forecasting
WTSA	Westernmost Tropical South Atlantic

LIST OF SYMBOLS

d_i	Model Error
X_{is}	Simulated variable
$\bar{X_{is}}$	Simulated variable average
X_{os}	Measured Variable
$\bar{X_{os}}$	Measured variable average
ME	Mean error
MAE	Mean absolute error
MSE	Mean squared error
$RMSE$	Root mean squared error
IA	Index of agreement
ρ_a	Surface air density
c_{pa}	Dry air specific heat
C_h	Transfer heat exchange coefficient
S	Mean wind Speed
T_s	Surface temperature
θ	Potential temperature
L_c	Evaporation latent heat
C_e	Transfer moisture exchange coefficient
q_s	Near surface moisture rate
q	Water vapour
C_d	Transfer wind stress exchange coefficient
u_s	Surface ocean stream flow
u	u-wind component
e_s	Saturation air pressure

q_{sfc}	Near surface water vapour
RM_{sfc}	Near surface moisture rate
P_{sfc}	Surface pressure
$FLQC$	Moisture coefficient of exchange
ρ	Air density
M_{avail}	Available humidity
U^*	u^* in similarity theory
κ	Von Karman constant
$PSIQ$	Humidity resistance
Q_{fx}	Upward motion of water vapour
q_v	First η level above surface Water Vapour
LHV	Water Evaporation Latent Heat
θ_{gb}	Near ground potential temperature
$FLHC$	Heat coefficient of exchange
HFX	Upward heat flux

CONTENTS

1 INTRODUCTION AND OBJECTIVES

The Northeastern Brazilian region (NEB) covers the area between 47°W-35°W; 18°S-1°S (RAO; LIMA; FRANCHITO, 1993) and is divided into different climatic regions. The NEB presents pronounced space-time rainfall variability as a result of different atmospheric forcing (RAO; LIMA; FRANCHITO, 1993; HASTENRATH, 2012; HÄNSEL et al., 2016). This inter annual variability in rainfall is mainly controlled by the sea-surface temperature (SST) of the tropical Pacific, associated with El Niño/La Niña events, (ARAGÃO, 1998; ANDREOLI; KAYANO, 2006; ANDREOLI; KAYANO, 2007) and Atlantic (MOURA; SHUKLA, 1981; MOURA et al., 2009; SILVA; GUEDES, 2012), as well the action of both oceans (ANDREOLI; KAYANO, 2006; ANDREOLI; KAYANO, 2007) causing extreme drought/rainfall in this region.

The rainfall variability in the Northern and central semiarid regions of the NEB is associated with the north-south migration of the Inter Tropical Convergence Zone (ITCZ) (MOSCATI; GAN, 2007; HASTENRATH, 2012; RODRIGUES et al., 2011; MARENGO et al., 2017). In the southern, western and central regions of the NEB, the South Atlantic Convergence Zone (SACZ) brings rainfall to the semiarid region during austral spring and summer (NOGUES-PAEGLE; MO, 2002). During January and February there is the occurrence of Upper Troposphere Cyclonic Vortex (UTCVs). In the eastern NEB (ENEB) the precipitation is modulated by Easterly Waves Disturbances (RAMOS, 1975; TORRES; FERREIRA, 2011; KOUADIO et al., 2012; GOMES et al., 2015) with maximum rainfall between May and July, with annual average rainfall above than 1500 mm.

In 2010, a succession of intense rainfall events given rise to floods in the eastern rivers of the Pernambuco and Alagoas States. The World Bank report and the government of Pernambuco (2010), registered a total of 67 damaged cities, 20 deaths, almost 30,000 homeless and an economic loss of approximate $ 1 billion. In that year, it was possible to observe positive SST anomalies in the Westernmost Tropical South Atlantic (WTSA) which exceeded 1°C in relation to the climatology between February and June, recorded in the Prediction and Research Moored Array in the Tropical Atlantic (PIRATA) (SERVAIN et al., 1998) buoy located at 8°S 30°W, as well as the SST data from the Advanced Very High-Resolution Radiometer AVHRR (http://oceanwatch.pifsc.noaa.gov).

There is a positive correlations between SST over the westernmost TSA regions and the variability of NEB precipitations (MOURA et al., 2009). These correlations are connected to water vapour transport from ocean to land (CAVALCANTI; GANDU; AZEVEDO, 2002), heat and moisture exchange between ocean and atmosphere (FOLTZ; MCPHADEN, 2006; CINTRA et al., 2015; HOUNSOU-GBO et al., 2015) and instabilities over warm waters (WANG; ENFIELD, 2001). Climatically the WTSA thermal seasonality has a small variation (±2 °C) as well as low average monthly anomalies (±0.3 °C) (HOUNSOU-GBO et al., 2015). Due to SST

anomalies exceed 28.5∘C in period from February to June in WTSA, these regions were similar to a Warm Pool or Southern Atlantic Warm Pool (SAWP) (WANG; ENFIELD, 2001; WANG et al., 2006; WANG; LEE, 2007).

Oceanic Warm Pools are regions with temperatures above 28.5 ∘C with well defined seasonal patterns in terms of time and space (WANG; ENFIELD, 2001). In these regions, oceanic dynamics favours low pressure on the surface, moisture convergence, increasing the water vapour content, atmospheric instabilities and convective cloudiness. Besides, intensifying the meteorological systems that will modulate the rainfall in continental regions adjacent to the warmer surface waters (BROWN; ZHANG, 1997; WANG et al., 2006; KOUADIO et al., 2012; HOUNSOU-GBO et al., 2015).

Over the entire trade winds regions around the Earth, there is a stable layer in the low troposphere resulted from the equilibrium between subsidence and the surface fluxes, which isolates the well mixed Marine Atmospheric Boundary Layer (MABL) from the free atmosphere above and inhibits the vertical motion (LINDZEN; NIGAM, 1987). This layer is called Trade Winds Inversion Layer (TWIL), and it is characterised by a strong increase of the stable vertical gradient of potential temperature and a high decrease of the mixing ratio (JOHNSON et al., 1999). This dynamics are presented either in Tropical South Atlantic and NEB region.

The trade winds inversion height is controlled horizontally by averaged values of sea surface temperature, atmospheric divergence and above-inversion atmospheric structure (SCHUBERT et al., 1995). Due to this, in regions over oceanic warm pools it is common found higher TWIL base, where can be found in 925 to 800 hPa (SCHUBERT et al., 1995; CARRILLO et al., 2015), and these effect cause many of convective rainfall over regions nearby warm waters (JOHNSON et al., 1999). Hence, convective precipitation over the ENEB has a direct correlation with the height of the base of the thermal inversion layer, which, in turn, is correlated with the SST on WTSA.

The interaction between air and sea, in SAWP region, is important for understanding the climatic variability over ENEB, due to heat, momentum and moisture exchange between these two media (BOURRAS et al., 2004). Ocean surface fluxes are determined by ocean surface temperature as well near-surface air temperature, humidity and wind speed, all of which are explicitly linked to MABL processes (ZENG et al., 2004). As the MABL interact with more warmer (colder) waters, both latent and sensible heat fluxes increases (decreases), the TWIL weakens (strengthens) and there are higher (smaller) well mixed MABL (PYATT et al., 2005).

The vertical structure of MABL is a key factor to triggering the occurrence of some synoptic activities such as deep convection (PENG et al., 2016). The warmer SST over SAWP region is directly related to rainfall variability over Recife (ENEB) (HOUNSOU-GBO et al., 2015). But, such as the warmer (colder) and large (small) warm pool is linked to more (less) intensity and formation of hurricanes in the North Atlantic (WANG et al., 2006), the SAWP region, also, can be an important region to intensify meteorological systems over ENEB leading

to extreme rainfall.

The Easterly Waves Disturbances, which modulates the ENEB rainfall are observed during entire year, but have more capability to generate rainfalls in the austral winter, giving rise to high daily precipitations (KOUADIO et al., 2012; GOMES et al., 2015). The ascending humidity from low to medium levels of the atmosphere occurs due to the presence of upward movements, moisture convergence, thermal fluctuation, and cyclonic vorticity in the 850 hPa, 700 hPa and even 500 hPa levels (KOUADIO et al., 2012; GOMES et al., 2015). Due to these synoptic-scale meteorological disturbances there is a weakening, or breaking, of the TWIL which allows the well mixed MABL provide moisture to mid and higher levels of the atmosphere (GRAY, 1968; LINDZEN; NIGAM, 1987; KORACIN; ROGERS, 1990; SCHUBERT et al., 1995; JOHNSON et al., 1999; PYATT et al., 2005).

Due to a lack of data set over TSA, it is difficult to study the air-sea interactions over the SAWP region during meteorological disturbances, which cause extreme rainfall episodes in the ENEB. To fill this gap, simulations with regional coupled atmosphere and ocean models can be performed. Three-dimensional coupled atmosphere-ocean models have been developed and applied to idealised and realistic scenarios, in order to predict the interactions between a tropical cyclone and the ocean (WARNER et al., 2010). Also, the expectations in coupling atmosphere and oceanic models are the well resolved interactions between the physics in either MABL and Ocean Mixed Layer (OML) to generate more precisely intense weather conditions to the forecast (RENAULT et al., 2012).

The Coupled Ocean-Atmosphere-Wave-Sediment Transport (COAWST) is comprised of several components that include models for the ocean, atmosphere, surface waves, sediment transport, a coupler to exchange the data fields, and a method to regridding (WARNER et al., 2010). The system has interactivity with all components, exchanging prognostic variables between them, allowing more realistic resolving in air-sea feedback interaction than only an atmospheric model which uses static SST (WARNER et al., 2010; RENAULT et al., 2012).

The main objective of this work is to investigate the sea-air interaction processes over the SAWP and the relationship with extreme rainfall events. Also, there is a interest in verify the capability of the coupled model to predict intense rainfall over the ENEB. Identify the effects of ideal different SST conditions in the model convection. Quantify the impacts in atmospheric thermodynamics under different SAWP conditions. Verify the influence of SAWP in different real conditions.

2 THE STUDY AREA CHARACTERISATION

2.1 GEOGRAPHIC DOMAINS

2.1.1 Northeast Brazil

The Northeast Brazil is sited in tropical region between 1 °S - 18 °S Latitude ; 35 °W - 47 °W Longitude. In all its extension, the northeast covers localities with rainfall above 1500 mm, in coastal areas, and regions with rainfall climatology about 400 mm annually (KOUSKY, 1979; KOUSKY, 1980; RAO; LIMA; FRANCHITO, 1993). Due to climatic and physical discrepancy, the NEB has humid and semi-arid climates (also, *Sertão*), with transition regions known as *Agreste*. Due to topographic features (Figure 1), there are local circulation factors (FEREIRA; MELO, 2005) that may generate micro climates in higher topography regions, such as the *Chapada Diamantina* and *Chapada do Araripe*, which are humid climates in semiarid border regions. Figure 1 shows the Brazilian topography.

The high variability of NEB is characterised by different atmospheric synoptic activity, leading three (in average) areas with different rainfall climatology (KOUSKY, 1979) as shown in Figure 2. In the northern and central semiarid regions of the NEB the north-south migrations of the Inter Tropical Convergence Zone (ITCZ) reach the maximum precipitation between February and May (MOSCATI; GAN, 2007; HASTENRATH, 2012; RODRIGUES et al., 2011; MARENGO et al., 2017). The hydric excess in the northern NEB (NNEB) is correlated with the ENSO cold phase (ANDREOLI; KAYANO, 2006; ANDREOLI; KAYANO, 2007) and with negative Atlantic Dipole (AD), which means positive Tropical South Atlantic (TSA) SST anomalies (MOURA; SHUKLA, 1981; KOUADIO et al., 2012; HOUNSOU-GBO et al., 2015).

In the southern (SNEB), western (WNEB) and central (CNEB) regions of the NEB, the cold fronts (KOUSKY, 1979) and the South Atlantic Convergence Zone (SACZ) brings rainfall to the south of semiarid region during austral spring and summer (NOGUES-PAEGLE; MO, 2002). The SACZ is characterised by an organised Convective Cloud-Band (CCB) that generally extends from the Amazon to the Atlantic Ocean in a northwest-southeast axis (ROBERTSON; MECHOSO, 2000).

In the eastern NEB (ENEB) the precipitation is modulated by Easterly Waves Disturbances (EWD) (RAMOS, 1975; TORRES; FERREIRA, 2011; KOUADIO et al., 2012; GOMES et al., 2015) with maximum rainfall between May and July, with annual average rainfall above than 1500 mm. The TSA regions near the east coast of the NEB are responsible for the supply of water vapour, which are carried by the southeast trade winds (CAVALCANTI; GANDU; AZEVEDO, 2002) into the continent. Thus, the ENEB has a positive correlation between the rainfall anomalies and the Western South Tropical Atlantic (STA) SST anomalies (HOUNSOU-GBO et al., 2015).

Figure 1 – Northestern Brazil topography. Near coastal areas elevation in 0 - 200m height, meanwhile central areas varying from 200 - 1200m in height.

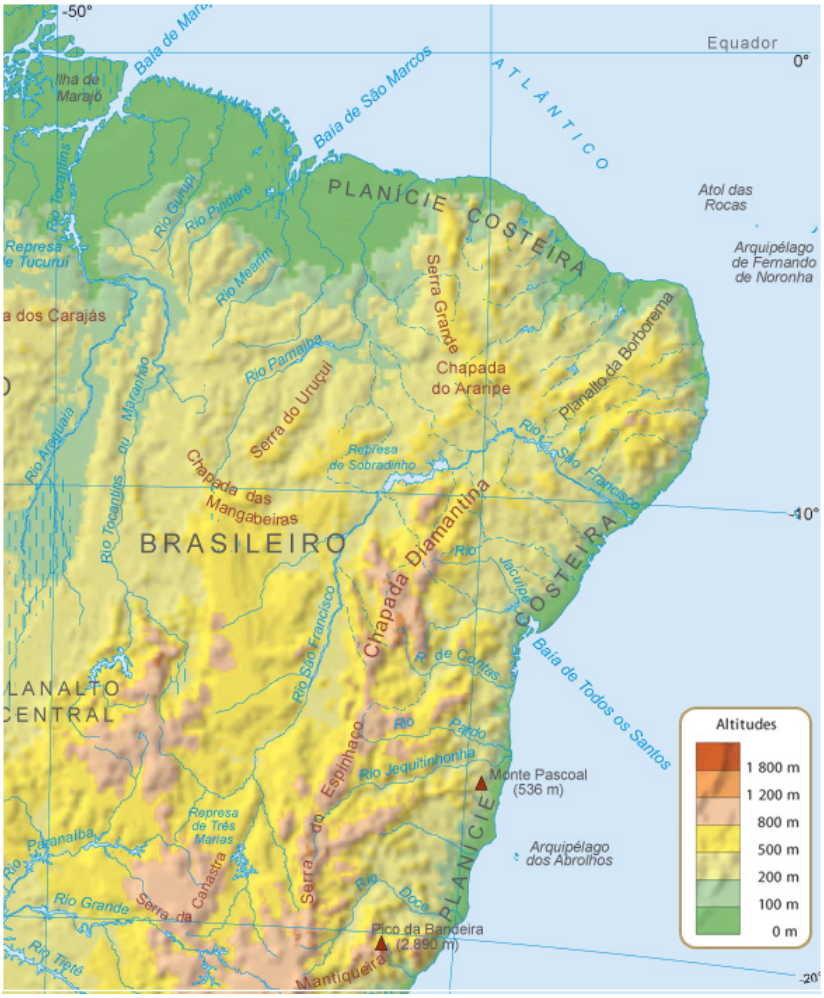

Source: Instituto Brasileiro de Geografia e Estatística - IBGE

During December to February there is the occurrence of Upper Troposphere Cyclonic Vortex (UTCVs). These vortex are formed and/or intensified downstream from strongly amplifying mid-latitude frontal systems, and are maintained by a direct thermal circulation, with cold air sinking in the centre and relatively warm air rising on the periphery (FEREIRA; MELO, 2005). Figure 2 shows the zonal climatology of Brazilian Northeast.

2.1.2 Tropical South Atlantic ocean

In similar manner, the dynamics that control the variability in the western boundary regime of the TSA could be a result of the seasonal changes of the surface wind speed. The ITCZ migrates meridionally, on seasonal time scale, leading to changes in the upper ocean parameter distribution and also in the ocean circulation (STRAMMA et al., 2005). A major portion of variability in the tropical Atlantic currents seems to be driven by large-scale seasonality in the trade wind regime and the latitude of the ITCZ (STRAMMA; ENGLAND, 1999; LUMPKIN;

Figure 2 – Brazilian Northeast rainfall climatology zones. I - Is the Southern Northeast Brazil, with maximum precipitations between November and February; II - Northern Northeast Brazil, with maximum precipitation between February and May; III - Eastern Northeast Brazil, maximum precipitation between May and August.

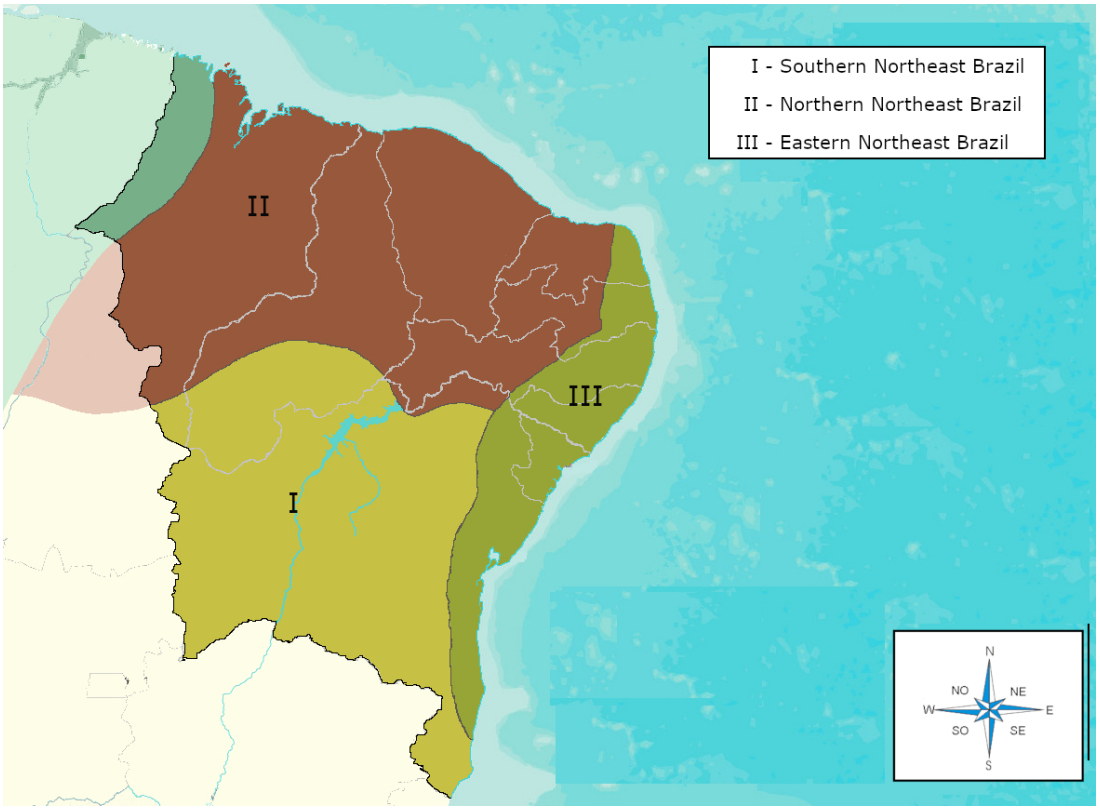

Source: Adapted from IBGE

GARZOLI, 2005).

The Southern Equatorial Current (SEC) forms the northern part of the South Atlantic Ocean subtropical gyre, carrying subtropical waters from the Benguela Current region towards the Brazil shelf region around 14 °S, where it bifurcates into the North Brazil Undercurrent (NBUC), later North Brazilian Current (NBC) to the north and the Brazil Current (BC) to the South (RODRIGUES; ROTHSTEIN; WIMBUSH, 2007). The SEC can be divided into three bands in the South Atlantic. The northern SEC (nSEC), the central SEC (cSEC) and the southern SEC (sSEC) flows (STRAMMA; ENGLAND, 1999). Figure 3 represents the schematic representation of mean current flow in tropical Atlantic.

In particular, the sSEC bifurcation region brings together multiple oceanic weather and climate interactions of great importance. Among these interactions they can be enumerated: (i) transfers of heat and mass between different layers of the tropical Atlantic subsurface; (ii) exchanges of heat and fresh water between the ocean and the atmosphere on the tropical Atlantic surface; (iii) links between climatic variability of the SST and the heat content of the upper layers of the tropical Atlantic and related atmospheric systems, which controls precipitation on

Figure 3 – Schematic representation of mean zonal and meridional currents are indicated: The upper ocean northward NBUC flow (red solid line), and the deepest southward transport by the DWBC (blue dashed line). The sSEC bifurcation at 100m depth (solid line); between 200m and 500m depth (dashed line); between 500m and 1200m depth (pointed line), according with (STRAMMA; ENGLAND, 1999).

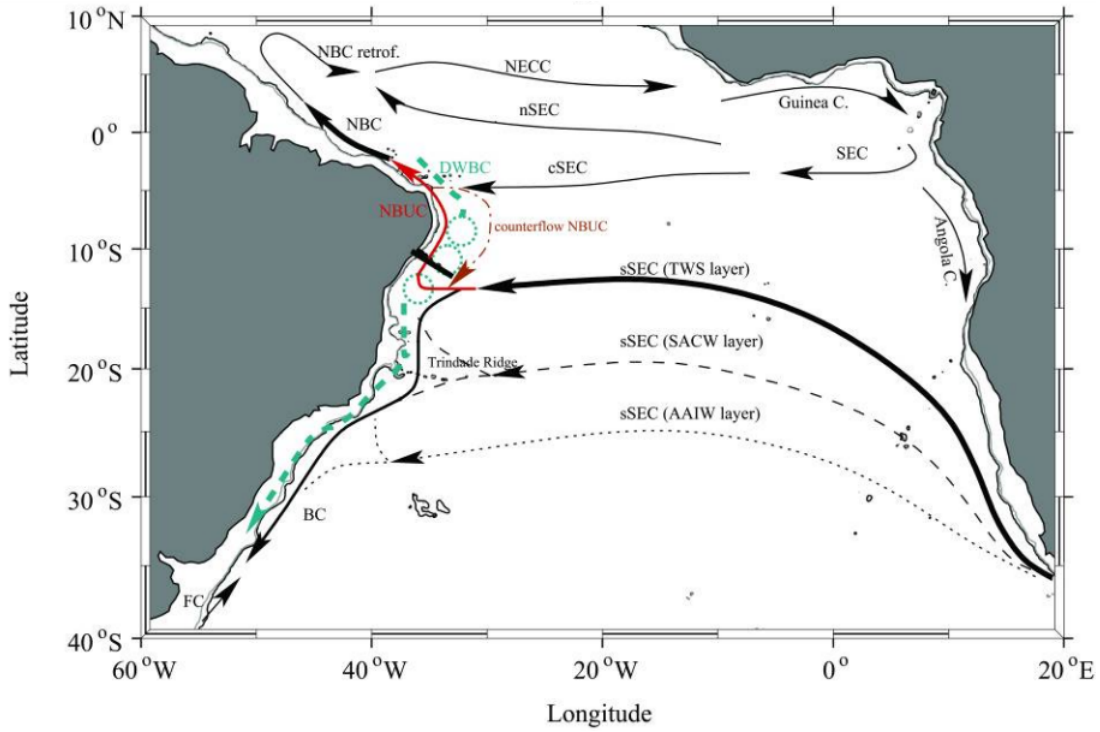

Source: Veleda, 2008

the NEB.

These circulation characteristics lead to a thermal climatology over TSA. The ocean water are colder in eastern side of basin due to upwelling and a warmer water in western side due to downwelling. The seasonal cycle of temperature shows values varying from about 25.5 ° to 28.0 ° from September to April in longitude near 34 °W. After reach the maximum temperature, there is a decreasing, reaching the minimum in Semptember with temperatures near then 25.5 °. In longitude near 20 °W, the same patterns are presented but temperatures are colder with thermal amplitude of 23.5 °C to 26.5 °C. The pattern of cooling of western basin of TSA are due to latent heat losses (FOLTZ; MCPHADEN, 2006), and coincide with the most rainfall period in ENEB (CINTRA et al., 2015) which are, also, direct related with rainfall anomalies in this areas (MOURA et al., 2009; KOUADIO et al., 2012; HOUNSOU-GBO et al., 2015).

2.2 TRADE WINDS INVERSION LAYER

The Atmosphere Global Circulation (AGC) is caused by solar irradiance which cause a meridional gradient of temperature, where are warm areas near the equator and cold areas in the poles.

Due to the equator receive more heat then high latitudes regions, there is a upward motion of the air and a surface low pressure. At the Equatorial region in the top of troposphere, the air diverges and generates a poleward wind flow descending at the middle latitudes.

The subsidence at mid Latitude generates a surface high pressure, causing a pressure gradient between mid latitudes and equator generating wind flows equatorward.

Then, the Coriolis effect turns the wind due to earth circulation, causing persistent wind at surface with southeast (northeast) direction in south (north) hemisphere called Trade Winds.

The thermodynamics of trade winds shows a inversion layer, in trade wind belt, caused by descendent branch of Hadley cell and local thermodynamics patterns (SCHUBERT et al., 1995; CARRILLO et al., 2015) here called Trade Winds Inversion Layer (TWIL) as shown in Figure 4. The base of TWIL is characterised by a strong increase of the stable vertical gradient of potential temperature and a high decrease of the mixing ratio (JOHNSON et al., 1999). These inversions acts as a barrier layer preventing upward motion of humidity and high vertical cloudiness from a moist and buoyant Marine Atmospheric Boundary Layer (MABL) (LINDZEN; NIGAM, 1987).

Therefore TWIL regions are connected to clear or cumulus humilis clouds types over warm waters and to high stratiform cloud cover over cold waters (CARRILLO et al., 2015) as exemplified Figure 4. It's verified warm rains in regions influenced by trade winds surrounded by warm waters due to development of tower cumulus (LIU; ZIPSER, 2009), similar to ENEB commonly daily rainfall. In fact, where the warm water are presents and a deep TWIL is observed, cumulus towers can appears with the cloud top height limited to the TWIL base.

Over the oceans where the SST gradients are present, the TWIL shows an important characteristic. Since over cold waters the shallow and mixed MABL are under influence of a high inversion, there are high stratiform cloud cover. However, crossing the SST gradient, these structure can be broken, by entrainment and turbulence, its make the regions uncoupling stratiform clouds and change to cumuliform. These shallow culuniform clouds when crossing the warm ocean acquires energy from ocean being more high developed (Tower Cumulus) limited by base of TWIL (PYATT et al., 2005; CARRILLO et al., 2015).

The example of how it occurs are show in the Figure 5. Near Africa west coast are present stratiform clouds in cold waters region. In Central South Atlantic there is a decoupling region, with stratiforms and cumuliform clouds. Near the East coast of Brazil, the tower cumulus near land.

2.3 EASTERLIES WAVE DISTURBANCES

Easterlies Wave Disturbances (EWD) are atmospheric disturbances which travels in trade winds easterlies and in the easterlies of equatorial through (also known as ITCZ). EWD are responsible to brings huge quantity of moisture, tropical instability and upward motions causing development of cumulus cloudiness and responsible to module the rainfall regime over

Figure 4 – Trade Wind inversion layer Structure

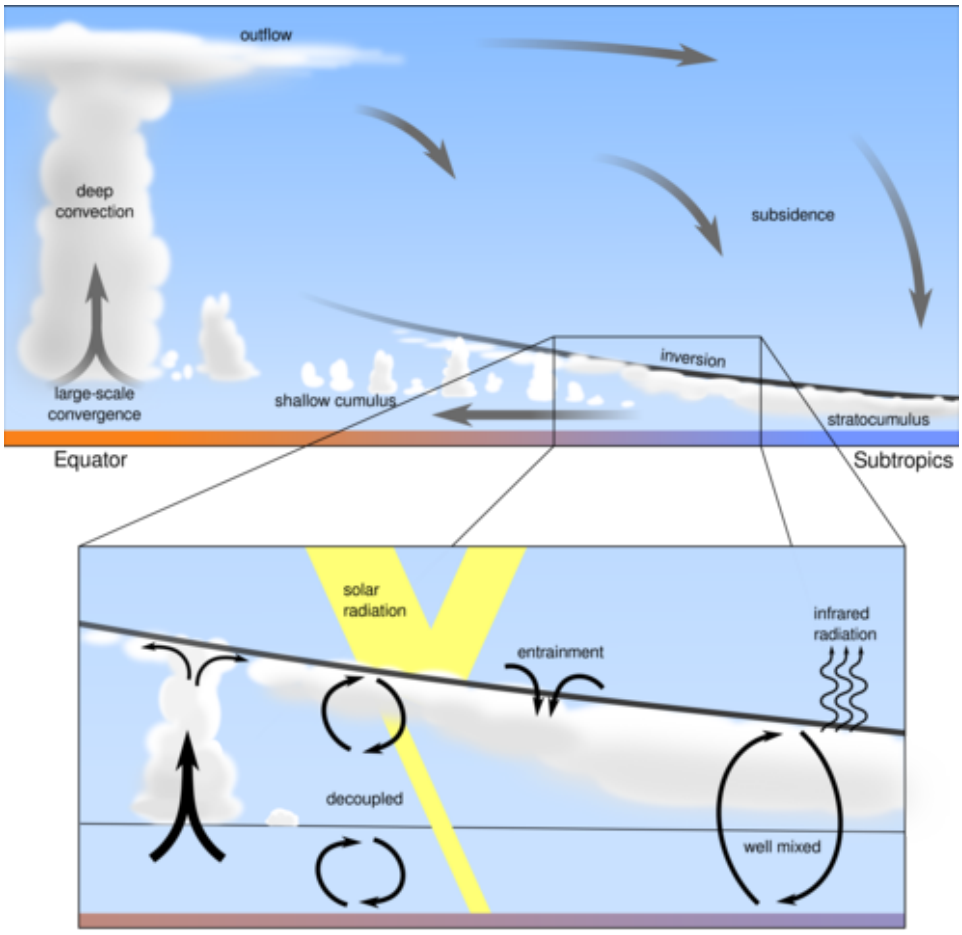

Source: Cloud Systems Evolution in the Trades - CSET

Figure 5 – Satellite image. Day 08 January 2018 at 0000UTC.

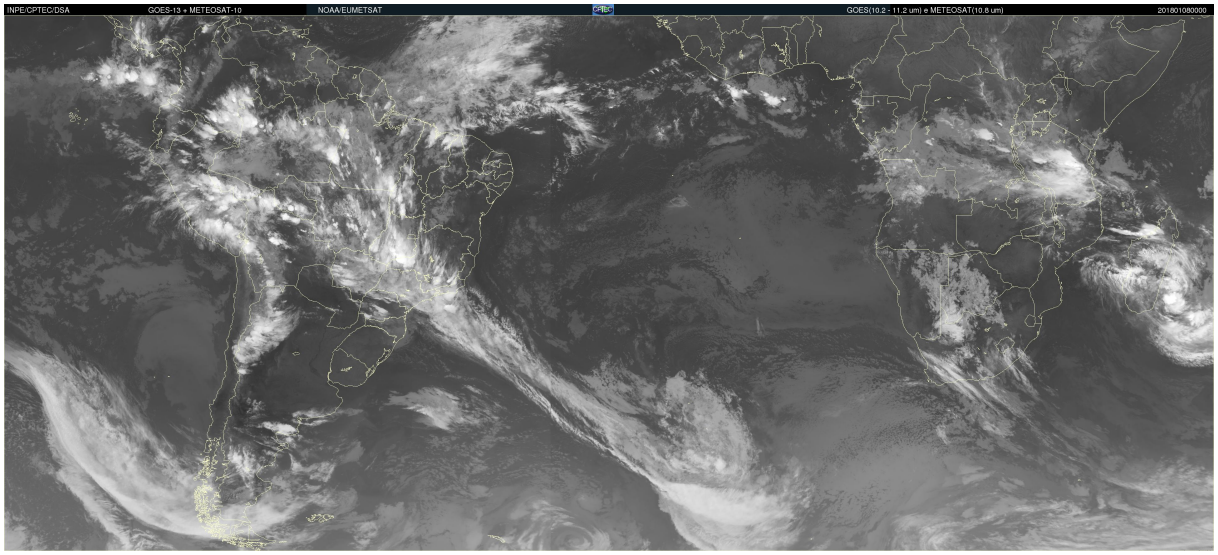

Source: *Centro de Previsão do Tempo e Estudos Climáticos* - CPTEC

the influenced regions. (FRANK, 1969; REED; NORQUIST; RECKER, 1977; DIEDHIOU et al., 1998; KAYANO, 2003; TORRES; FERREIRA, 2011; GOMES et al., 2015).

In the dynamical structure and synoptic-scale pattern, the EWD presents convergence (divergence) in low levels in vicinity of through (ridge), high (low) relative humidity and upward (downward) motion over the trough (ridge) (CARLSON, 1969; REED; RECKER, 1971; REED; NORQUIST; RECKER, 1977; TAI; OGURA, 1987; DIEDHIOU et al., 1998; KAYANO, 2003; DIEDHIOU; MACHADO; LAURENT, 2010; TORRES; FERREIRA, 2011; GOMES et al., 2015). Over the through, linked to upward motion, there is a pattern of convective cloudiness in shape of inverted "V" in northern hemisphere, opposite in south hemisphere, and cloud blobs (FRANK, 1969).

These characteristics persists over the entire tropical regions and make possible to identify these disturbances in many ways, such as: Satellite composite (CARLSON, 1969; FRANK, 1969; YAMAZAKI; RAO, 1977), Wind and satellite composite (REED; RECKER, 1971; REED; NORQUIST; RECKER, 1977; REED; KLINKER; HOLLINGSWORTH, 1988; DIEDHIOU et al., 1998; GOMES et al., 2015), Spectral analysis (DIEDHIOU et al., 1998; KAYANO, 2003; DIEDHIOU; MACHADO; LAURENT, 2010), Dynamical diagrams (Hovmuller) (NEVES; ALCÂNTARA; SOUZA, 2016) and others techniques (THORNCROFT; HODGES, 2001; BERRY; THORNCROFT; HEWSON, 2007; SERRA; KILADIS; HODGES, 2010; TORRES; FERREIRA, 2011).

There is EWD over entire tropical areas in the entire world but they vary seasonally in strength and intensity (CARLSON, 1969) and have more records in northern than southern hemisphere (YAMAZAKI; RAO, 1977; TAI; OGURA, 1987). Some of the EWD are responsible to develop the tropical cyclonic around the world, such as Hurricane in the North America and Typhoon in the the West Pacific basin. The African Easterlies Waves (AEW) is an example of these tropical disturbances (CARLSON, 1969; FRANK, 1969; BURPEE, 1972; REED; NORQUIST; RECKER, 1977).

The AEW are disturbances developed in Saharan continent and crosses the Tropical North Atlantic ocean (FRANK, 1969; BURPEE, 1972), and many of those AEW develop Central and North America tropical storms and hurricanes (CARLSON, 1969). In western Pacific the EWD are less intense than AEW, but the occurrence and the displacement occurs in the same way, crossing tropical Pacific reaching the Eastern coast of continents in the West Pacific region, sometimes developing to a Typhoon (TAI; OGURA, 1987).

The influences of EWD in Tropical South Atlantic (TSA) was observed by (YAMAZAKI; RAO, 1977) with satellite composite and noticed seasonal types of clouds moving eastward by trade winds, but with less intensity than another places in earth. Also using Longitude x time diagrams from meridional wind component, is possible to perceive the presence of the EWD over the ENEB (NEVES; ALCÂNTARA; SOUZA, 2016). These disturbance can occur in every seasons, but to appear more organized during March-April-May (MAM) and June-

July-August (JJA) where there is more variations in meridional wind, there is more activity of EWD in this period (COUTINHO; FISCH, 2007; DIEDHIOU; MACHADO; LAURENT, 2010), coinciding with the wet season over the ENEB (KOUSKY, 1979; KOUSKY, 1980; RAO; LIMA; FRANCHITO, 1993).

Each EWD over STA, as well around the world, have different dynamical patterns compared to each other. For example, the EWD moving around equator have more phase speed than southern ones, the period can vary season to season where the double of records can be observed between dry and wet season (COUTINHO; FISCH, 2007), also the high and deepens of through where the trough can be found on 925, 850, 700 or 500 hPa and wavelength (KAYANO, 2003; COUTINHO; FISCH, 2007; GOMES et al., 2015), and this cause variations in the intensity of rainfall under EWD influence.

2.4 OCEAN ATMOSPHERE INTERACTION

The ocean and the atmosphere has a strictly relationship to control the climate on Earth. Heated by the sun's radiation, the ocean and land surface evaporate water, which then moves around with wind in the atmosphere, condenses to form clouds, and falls back to Earth's surface as rain or snow, with the flow to oceans via rivers completing the hydrology cycle (TRENBERTH, 2011).

The ocean is an important component of the climate system. It provides the surface temperature boundary condition for the atmosphere over 70% of the globe. It absorbs over 97% of solar radiation incident on it from zenith angles less than 50°. It provides 85% of the water vapour in the atmosphere. It exchanges, absorbs and emits a host of radiative important gases. It is a major natural source of atmospheric aerosols. Thus, even a static ocean would significantly influence the climate. However, the ocean is dynamic and its surface properties will vary on all time scales, allowing great scope for feedback between the ocean and atmosphere (BIGG et al., 2003).

The Marine Atmospheric Boundary Layer (MABL) over the Earth's ocean plays a critical role in regulating the surface energy and moisture fluxes and in controlling the convective transfer of energy and moisture to the free atmosphere (KLOESEL; ALBRECHT, 1989; PYATT et al., 2005). Ocean surface fluxes are determined by ocean surface temperature as well as near-surface air temperature, humidity and wind speed, which is explicit linked to the MABL (ZENG et al., 2004). So, the structure of MABL, which contains most of water vapor and energy flux in atmosphere column, is one of the key factor that trigger the occurrence of some synoptic activities, such deep convection (KLOESEL; ALBRECHT, 1989; PENG et al., 2016).

Across the ocean, the tropical western basin are warmer than eastern side due the mid-latitude gyre and air-sea interactions, mainly subtropical high (CLEMENT; SEAGER; MURTUGUDDE, 2005). Its cause a downwelling (upwelling) of waters lead to regions generally

covered by waters warmer (colder) in west (east) ocean basins. Sometimes, where ocean basins reaches temperatures higher than 28.5°C, its called Warm Pools (WANG; ENFIELD, 2001). The process of the formation and maintenance of warm pools is the ocean-atmosphere feedback, such as convective activity and cloudiness resulting less net long-wave radiation loss (CLEMENT; SEAGER; MURTUGUDDE, 2005; WANG; ENFIELD, 2003).

Warmer SST are associated with warmer and moister troposphere, reducing Sea Level Pressure (SLP), weaker easterlies winds, less vertical wind shear, and weakened subsidence aloft. Years with well developed warm pool, these conditions lead to generally greater summer rainfall over Intra American Sea (IAS), Central America (WANG; ENFIELD, 2003) and rainfall regimes over Western Pacific Regions (BROWN; ZHANG, 1997), and the opposite also occurs (WANG; ENFIELD, 2003; BROWN; ZHANG, 1997), the cold water generate dry summer in these regions.

There is two key factors to lead the storm genesis and intensification. Due to favourable effects of latent and sensible heat fluxes, derived from the ocean surface layers, and the vertical wind shear in the troposphere (DAILEY et al., 2009). These factor are present in warmer warm pool conditions. For example, the North Atlantic Warm Pool largely reduces the troposphere vertical wind shear and increases latent heat losses during August to October (WANG; LEE, 2007). Also the tropical cyclone intensity increases when more heat content are available in deeper ML (CHAN; DUAN; SHAY, 2001).

Also, the track and intensity of hurricanes are modulated by chain of warm SST. The influence of landfall precipitation between tropical disturbances and storms in different places in United States of America (USA), shows the amount and route of storms are variants in cool and warm SST North Atlantic. Even so, the hurricanes developed over Gulf of Mexico in cool SST are weaker then eastern Atlantic warm waters due to short pathways of warm waters (DAILEY et al., 2009).

However, the structure of MABL and the TWIL height also perform important issues to climate modulation over tropical regions. For example, the displacement speed of TC is responsible to modify his structure. In the presence of a strong advective flow, the TC has less time to be cooled by the ocean, and thus the TC becomes more intense (CHAN; DUAN; SHAY, 2001). Also, the height of TWIL is a limiting factor to the development of high cumulus clouds (SCHUBERT et al., 1995). These convective clouds patterns limited by TWIL are associated with develops of warm rains (LIU; ZIPSER, 2009).

Analogously to TC dynamics, the atmospheric disturbances over south Atlantic have more convective activity over the ENEB in the presence of warmer waters over Westernmost Tropical South Atlantic (WTSA) (MOURA et al., 2009; KOUADIO et al., 2012; HOUNSOU-GBO et al., 2015). In the rainy period of ENEB, when EWDs interact with local circulation, low-level convergence can be increased, leading to high amount of precipitation (GOMES et al., 2015). These low-level convergence is increased by warmer waters surface in WTSA (KOUADIO

et al., 2012).

The EWDs has high frequency in the layers in the 850-700 hPa layers during the rainy season (COUTINHO; FISCH, 2007). The propagation of EWDs to the ENEB is associated with center of moist and upward motion associated to a humidity convergence in low levels (GOMES et al., 2015). These 850-700 hPa layers is common to find the base of TWIL (SCHUBERT et al., 1995). So these disturbances in 850-700 hPa acts to provide low level moisture to mid-levels, above the inversion layer, which can favors to the deep convection.

Therefore in periods where anomalies of surface waters in WTSA is higher than 28.5° the west basin acts as a warm pool, its commonly named as SAWP (HOUNSOU-GBO et al., 2015). The MABL structure, the air-sea interaction over SAWP and the influence in the rainfall over ENEB is important due to impacts in flash floods in this regions. In scenario with climate change, the characterization of MABL, in the coupled ocean atmosphere forecasting models, can be a tool for mitigating the negative effects of extreme rainfalls.

2.5 OCEAN ATMOSPHERE MODELLING

Due to the climate vulnerability of ENEB, improvements in atmospheric modeling techniques are constantly employed (TORRES; FERREIRA, 2011). Because it has a direct relationship with the TSA, it is also well known that the numerical resolutions of the atmosphere ocean interface is a strategy for better predictions of intense rainfall episodes.

With the growing of computational power, the coupled modeling approach can provides means to develop multidisciplinary application with more robustness. The coupled model is capable to interact in two-way between the models either operating on different scales, or simulating different set of interdependent processes (WARNER; PERLIN; SKYLLINGSTAD, 2008).

The coupled ocean–atmosphere–wave and sediment transport (COAWST) modeling system is comprised of several components that include models for the ocean, atmosphere, surface waves, sediment transport, a coupler to exchange data fields, and a method for remapping, using all publicly available components (WARNER et al., 2010).

The model coupling toolkit (MCT) is an open software library for constructing parallel coupled models from individual parallel models. This application contains multiple instances of the MxN problem, the problem of transferring data between two parallel programs running on disjoint sets of processors. MCT was created as a generalized solution to handle these and other common functions in parallel coupled models (JACOB et al., 2005).

The structure built (Figure 6) consists of a main program that serves to control the flow and processor allocation of the coupled model system, called **Master**. This **Master** program was coded for run simultaneously on several different processors. At execution, the **Master** driver program distributes the total number of processors allocated for the job to the individual models,

Figure 6 – A flow chart of the coupled code forming a single-executable modeling system running in concurrent mode.

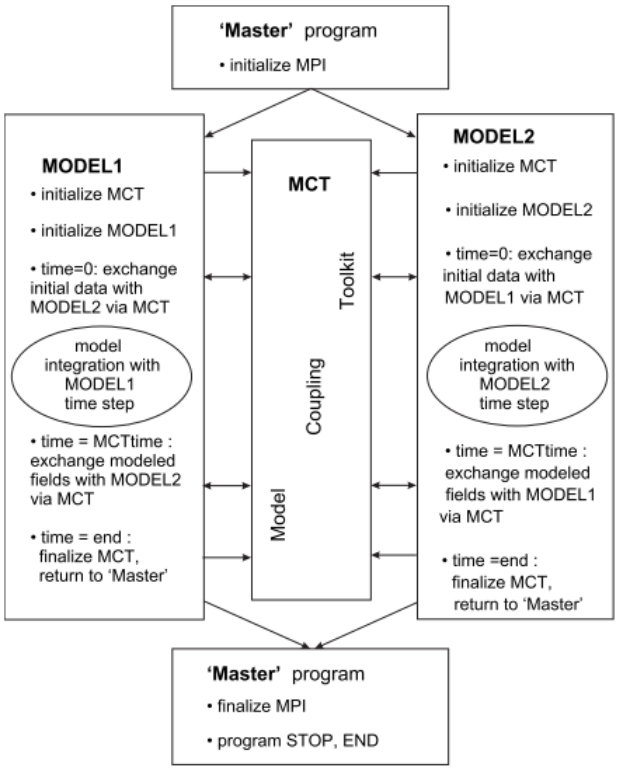

Source: (WARNER; PERLIN; SKYLLINGSTAD, 2008)

and calls each model component with an initialize, run where is defined the synchronization point, and finalize structure (WARNER; PERLIN; SKYLLINGSTAD, 2008). Figure 6 summarize the flows of routines in single-executable modeling system. This represent a layout of how the coupling model works.

To allow the models to exchange data fields on different grids we use the spherical coordinate remapping interpolation package (SCRIP) to compute interpolation weights (WARNER; PERLIN; SKYLLINGSTAD, 2008). The SCRIP provides a mechanism for computing remapping weights for both first- and second-order remapping. Use of these weights provides remapping that are up to second-order accurate and conservative to machine accuracy (JONES, 1999).

Because the method is completely general, weights can be computed for any type of grid on a sphere, allowing developers of component models in a coupled model context to use whatever grid is appropriate for a given component and not be constrained by compatibility with other component model (JONES, 1999).

The build scripts for the individual systems were modified such that the COAWST is compiled to produce one single executable. The modeling system runs in message passing interface (MPI) and before execution the user sets the number of processors that will be allocated for each model (ocean, atmosphere, and wave) (WARNER et al., 2010).

During initialization each processor from each model initializes with MCT, which is identified the distribution of model components on all the processors. MCT can then determine the grid distributions. During execution the models will advance in time until they reach a user defined synchronization point (WARNER et al., 2010). At that time each model fills its attribute vector to exchange prognostic variables through MCT to other models. The variables that are exchanged are shown in Figure 7.

The atmosphere model provides 10-m surface winds ($U10wind$, $V10wind$) to the wave and ocean models. The atmosphere also provides to the ocean model the atmospheric pressure ($Patm$), relative humidity (RH), atmospheric surface temperature ($Tair$), cloud fraction ($cloud$), precipitation ($rain$), shortwave ($SWrad$) and longwave ($LWrad$) net heat fluxes (WARNER et al., 2010).

The ocean model uses atmosphere model parameters in the coupled ocean atmosphere response experiment (COARE) algorithm (FAIRALL et al., 1996) to compute ocean surface stresses and ocean surface net heat fluxes. But, the fluxes calculated in both parameters can be inconsistent, to avoid this, the heat and moisture fluxes are calculated by atmospheric model and give to ocean model (ZAMBON; HE; WARNER, 2014). The ocean model provides SST to the atmosphere model. The ocean provides surface currents (us, vs), free surface elevation (g), and bathymetry ($bath$) to the wave model (WARNER et al., 2010).

The surface currents are averaged using a formulation of (KIRBY; CHEN, 1989) that integrates the near-surface velocity over a depth controlled by the wave number. The wave model provides significant wave height ($Hwave$) and wave length ($Lwave$) to the atmosphere and the ocean models. The atmosphere model uses these wave values to compute an enhanced sea surface roughness (WARNER et al., 2010).

The wave model also provides to the ocean model wave direction ($Dwave$), surface and bottom periods ($Tsurf$, $Tbott$), percent wave breaking (Qb), wave energy dissipation ($Wdissip$), and bottom orbital velocity (Ub). These parameters are used by the ocean model in the COARE algorithm to provide an increased surface roughness and in the sediment transport algorithms for bed load transport and bottom stress mobilization (WARNER et al., 2010).

The wave parameters are also available to compute wave-driven flows. The sediment model can provide spatially-varying bottom roughness as different grain sizes are mobilized and transported. The varying roughness is fed back to the ocean and wave models. The model uses the momentum and buoyancy fluxes computed by Weather Research and Forecasting (WRF) to directly drive the ocean model (ZAMBON; HE; WARNER, 2014). Figure 7 shows the possible configurations of data fields exchanged. Lower right panel (case D) shows all the fields that can be distributed. However, for this works, only WRF and ROMS interaction are activated, so for this work the chart flow are the Figure7b.

The WRF Model is a numerical weather prediction (NWP) and an atmospheric simulation

Figure 7 – A flow chart of the coupled code forming a single-executable modeling system running in concurrent mode.

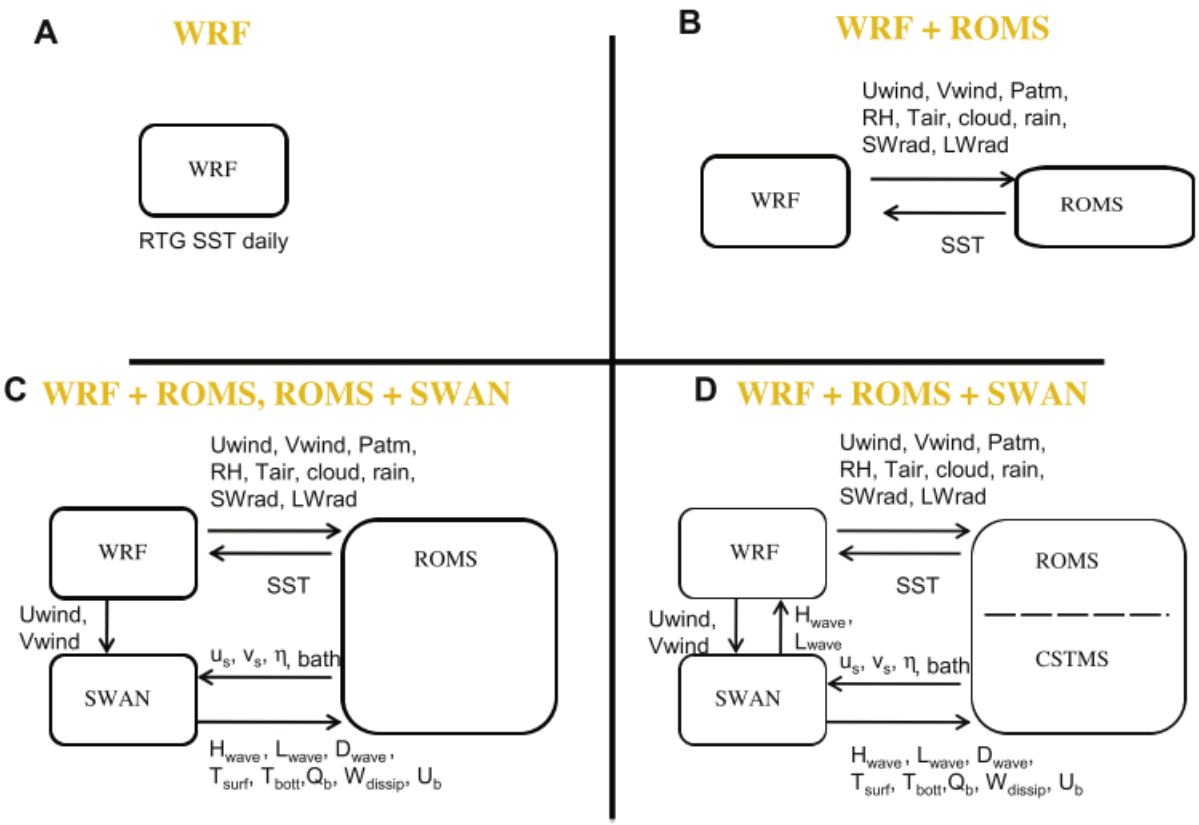

Source: (WARNER et al., 2010)

system designed for both research and operational applications. WRF reflects flexible, state-of-art, portable code that is efficient in computing environments ranging from massively-parallel supercomputers to laptops.

The Advanced Research in WRF (WRF-ARW) solver implements fully compressible Eulerian nonhydrostatic equations, with prognostic variables such as the u and v velocity components in Cartesian coordinates; vertical velocity w, potential temperature θ, geopotential ϕ and surface pressure perturbations; a terrain-following, dry hydrostatic-pressure, with vertical grid stretching permitted vertical coordinate η (ETA), horizontal grid based in Arakawa-C grid staggering; time integration in 2^{nd}- or 3^{rd}-order Runge-Kutta time-split integration scheme with smaller time steps for acoustic and gravity-wave modes; 2nd to 6th-order advection options in horizontal and vertical spatial discretization; turbulent mixing and model filters with sub-grid scale turbulence formulation in both coordinate and physical space, divergence damping, external-mode filtering, vertically implicit acoustic step off-centering and explicit filter option; one-way interactive, two-way interactive and moving nests, multiple levels and integers ratios for nesting options (SKAMAROCK et al., 2008).

The WRF physics options fall into several categories, each containing several choices.

Figure 8 – Flowchart of parameterization information exchange in WRF.

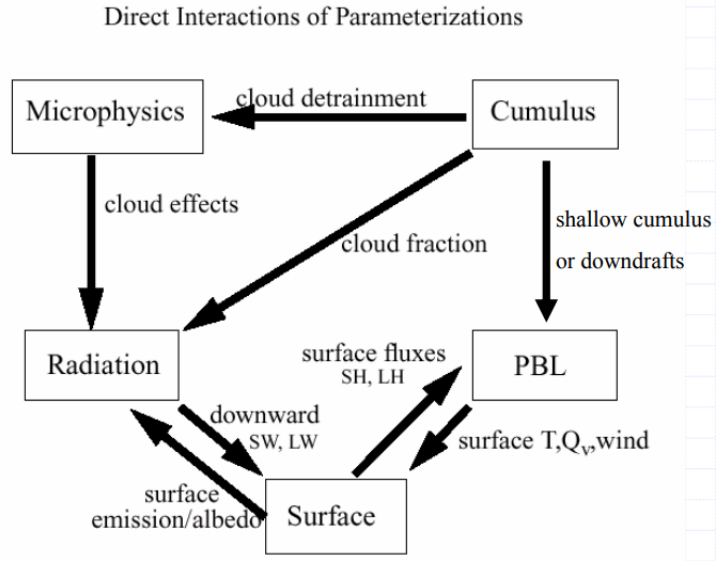

Source: Jimmy Dudhia

The physics categories are (1) microphysics, (2) cumulus parameterization, (3) planetary boundary layer (PBL), (4) land-surface model, and (5) radiation. Physics packages compute tendencies for the velocity components (un-staggered), potential temperature, and moisture fields (SKAMAROCK et al., 2008).

The directly influence of the COAWST in WRF solving is in the surfaces physics. However, this directly influence cause the chain effect for the entire atmosphere simulation, by sequence of information exchange as in Figure 8. The surfaces physics will provide the predicted variables to PBL and Radiation physics which in turn will have a feedback process with other parameterizations.

The ROMS solves the free surface primitive equations in a rotational earth-centered environment, based on the classical Boussinesq approximation and the vertical momentum hydrostatic balance (SHCHEPETKIN; MCWILLIAMS, 2005). The model considers the coast lines and coordinates that accompany the terrain, which allows to minimize the number of blind spots in the computational solution. The boundary conditions for the model are therefore appropriate for an irregular oceanic bathimetry and shorelines.

Boundary data include the influences of surface wind stress, heat and mixing fluxes, coastal river influences, bottom trawling, and radiative loss in the open ocean and nudging over the specific circulation in the basin. The model has previous adaptations in different regions of the globe (HAIDVOGEL et al., 2000; SHE; KLINK, 2000; PENVEN et al., 2000; PENVEN et al., 2001; MACCREADY; GEYER, 2001; LUTJEHARMS; PENVEN; ROY, 2003) Vertical advections in ROMS are treated with a third-order scheme that enhances the solution by generating abrupt gradients as a function of a given grid size (SHCHEPETKIN; MCWILLIAMS, 1998).

Unresolved processes of vertical sub-grid scales are parameterized by an adaptation of the planetary boundary layer scheme of the K profile (LARGE; MCWILLIAMS; DONEY, 1994). A full description of the model can be found in Haidvogel et. al. (2000).

3 DATA AND METHODS

3.1 DOMAIN CONFIGURATION AND DATA USED

The domain studied (45°W - 10°E; 20°S - 5°N), extends from the west coast of Africa to the east coast of the South American continent. It comprised the easternmost area of the Brazilian Northeast (ENEB), selected by the blue line (40.5°W - 35°W; 15.5°S - 4°S) (Figure 9). The western oceanic area (34°W - 25°W; 12.5°S - 4°S) characterise the Southern Atlantic Warm Pool (SAWP) region, selected by hatched square; and the 20°W - 10°E; 20°S - 8°S domain, is the region of thermal gradients of the South Atlantic in larger squared with crosses hatched.

The meteorological fields were analysed by Geostationary Operational Environmental Satellite (GOES) from National Oceanic and Atmospheric Administration (NOAA) and MeteoSAT from European Organisation for the Exploitation of Meteorological Satellites (EUMETSAT) satellite images, as well sounding profiles of the Recife city - PE (35.1°W; 8.5°S), from *Instituto Nacional de Meteorologia* (INMET). Precipitation data were available from *Agência Pernambucana de Águas e Clima* (APAC), yellow dots; the *Agência Executiva Gestão das Águas da Paraíba* (AESA), magenta dots; the *Empresa de Pesquisa Agrícola do Rio Grande do Norte* (EMPARN), blue dots; the *Instituto de Meio Ambiente e Recursos Hídricos* (INEMA).

Other meteorological observations are from the Data Collection Platforms, or DCPs, monitored by INMET (Figure 9 - red dots). For ocean modeling, we use in situ data from the oceanographic buoys of the PIRATA (Figure 9 - green dots) (SERVAIN et al., 1998) (available at: http://www.pmel.noaa.gov/Pirata/), located in the domain of study.

For the atmospheric modeling, two different databases were used, the boundary data were the NCEP FNL (Final) Operational Global Analysis Data (NCEP, 2000), with a resolution of 1° x 1° and the ERA-Interim Global Atmospheric Reanalysis (DSS / CISL / NCAR / UCAR / ECMWF 2005) with resolution of 0.7km (N128) (http://www.ecmwf.int), both every 6 hours.

When the coupled model between the ROMS model and the WRF was used, the variables of temperature, salinity and currents for the oceanic model were given by the Hybrid Coordinate Ocean Model (HYCOM), with resolution of 0.08° x 0.08° (WALLCRAFT et al., 2008).

When the coupling between WRF and ROMS was disconnected, the oceanic boundary condition was provided by the "Real-time, global, sea surface temperature (RTG-SST) analysis", developed by the National Centers for Environmental Prediction / Marine Modeling and Analysis Branch (NCEP / MMAB). RTG-SST has a resolution of 0.5° x 0.5° and was interpolated every 6 hours.

Figure 9 – Studied Domain. Squared with lines is the SAWP region. Squared with crosses hatched is the Gradient regions. Greens dots is the PIRATA buoy. Red dots is the INMET PCD. Yellow dots is APAC pluviometers. Magenta dots is AESA pluviometers. Blue dots is EMPARN pluviometers. Shaded color is the Earth elevations (bathymetry and topography).

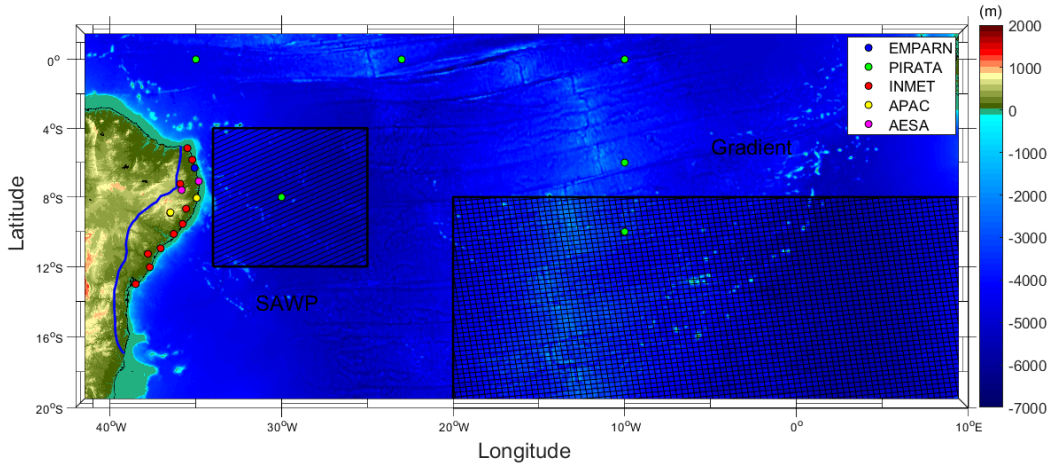

Source: The author. ENEB Region delimited by (RAO; LIMA; FRANCHITO, 1993). Topography and bathymetry by National Center for Environmental Information (NCEI/NOAA).

3.2 PERIOD OF STUDY

The period studied covers the years 2009 to 2016. During this period, floods and water scarcity were recorded throughout the Brazilian northeast (MARENGO et al., 2017).

For example, the year of 2010 had a succession of intense rainfall which cause flood events in the eastern rivers of the Pernambuco and Alagoas States. The World Bank report and the government of Pernambuco (2010), registered a total of 67 damaged cities, 20 deaths, almost 30.000 homeless and an economic loss of approximate $ 1 billion. In that year, it was possible to observe positive SST anomalies in the WTSA which exceeded 1°C in relation to the climatology between February and June, recorded in the Prediction and Research Moored Array in the Tropical Atlantic (PIRATA) buoy located at 8°S;30°W, as well as the SST data from the Advanced Very High-Resolution Radiometer (AVHRR) (http://oceanwatch.pifsc.noaa.gov).

In opposite, the year 2012 to 2016, were one of the driest periods in the Brazilian Northeast, registering droughts in the semiarid, as well as reaching part of the regions considered humid.

In this work we performed simulations for intense rainfalls (> 50 mm) of EWD across the years from 2009 to 2015. In total 16 events of intense rainfalls are simulated in years with high and low anomalies in SAWP SST.

3.3 EXPERIMENTS

3.3.1 Validations and 2010 Extreme Event

In the coupled experiments, the atmospheric model WRF provided atmospheric pressure values, zonal and meridional components of the wind at 10m, air temperature at 2m, fraction of clouds, precipitation, short and long wave radiation, as well heat and humidity fluxes. The ROMS model computes surface fluxes with the COARE bulk algorithm (FAIRALL et al., 1996). The oceanic model provides updated SST values for the atmospheric model (WARNER et al., 2010). The coupled interaction was configured to occur every 10 minutes of time step.

In the non-coupled model simulations, the initial conditions for SST was by the RTG-SST dataset. The update time-step it is 6-hours by interpolation of the initial data. In other words, the SST in WRF for these experiments don't have interaction between air-sea.

The WRF model set-up and physics parameterizations were based on those used in the weather forecasting set-up applied by the APAC. The atmospheric model uses the Single-Moment 6-class scheme, which considers 6-class of hydrometeor setup, including water vapor, clouds and precipitation processes (HONG; LIM, 2006). Cumulus-type cloud parameterization was based on Kain-Fritsch (KAIN, 2004), as well the option of triggered moisture advection (kfeta-trigger) (MA; TAN, 2009) and sub-grid for the effects of convective and shallow clouds. The short and long wave radiation parameterizations used is from rapid radiative transfer model (RRTMG), which responsible for solving the surface energy balance (IACONO et al., 2008).

1. To verify the role of heat and moisture exchange over the TSA region, we disabled the sensible and latent heat fluxes at the water surface in the WRF-ROMS model (WRF-ROMS-E1) and the uncoupled WRF model (WRF-E1). The fluxes are solved only over the continent.

2. In this experiment, we applied the Mellor Yamada Nino Nakanishi (MYNN) parameterization for the resolution of fluxes and final analysis from GFS (FNL) data for initial conditions in the WRF-ROMS-E2 and WRF-E2 cases. This setup is used in the official meteorological service of Pernambuco State. The WRF-E2 will serve as the control simulation.

3. We used the same parameterizations from Experiment 2 but changed the input data to ERA-Interim. The simulations were named WRF-ROMS-E3 and WRF-E3. Another initial condition is used to verify how the heat fluxes respond to the changes in the meteorological fields and how they impact the rainfall simulations.

3.3.2 Test Case

It was performed two SST input data in contrasting years. The first condition used was with HYCOM SST from 10 of June 2010, with the normal conditions. The second with the

SST of HYCOM from 10 of June 2012, with colder SST. The oceanic currents, salinity and meteorological fields to input ROMS remained the same as 2010 conditions.

In the coupled experiments, the WRF provided P_{atm}, $V10_{wind}$ and $U10_{wind}$, T_{air}, fraction of clouds, precipitation, short and long wave radiation, as well heat and humidity fluxes for June 2010. However, the oceanic model provides updated SST values for the atmospheric model every 10 minutes of time step with different SST conditions.

3.4 STATISTICS

Statistical validation was based on objective analysis of errors and concordance indices, as well as accuracy on set of atmospheric measurements compared to simulation results (HALLAK; FILHO, 2011). The tools described offer an alternative to statistical comparisons made in isolation at station points, which often penalise the results of numerical models (ANTHES et al., 1989).

The point-to-point correspondence between numerical simulation and observational measurements of the same variable provides a quantitative test to measure the model's ability (or accuracy) to predict observed data. Thus, if a variable X_{is} and X_os, respectively, simulated and observed at a point in the domain, the fundamental amount for the study of errors is the difference (d_i) in time and space, expressed as:

$$d_i = X_{is} - X_{os} \tag{3.1}$$

Basically, $d_i = 0$, perfect simulation; $d_i \ll or \gg 0$ imperfect simulation. Because it is a simple analysis, the estimate of the gross error does not show many types of errors that can contain a simulation, however derived from this analysis can be found several ways to verify such information.

The BIAS measures the tendency of the model to overestimate or underestimate the analysed variable in relation to the observed one. This trend, also called systematic mean error (ME) is defined as:

$$ME = BIAS = \bar{d} = \frac{1}{N}\sum_{i=1}^{N} d_i \tag{3.2}$$

Bias does not convey information about individual errors and therefore can not be used as a measure of model accuracy. Moreover, while giving an idea of systematic bias or error, bias is affected by the fact that individual positive and negative errors of the same magnitude cancel out in the sum. The average of the absolute errors (Mean Absolute Error $\mid d \mid$ or MAE) circumvents this problem. Because it is less affected by outliers, MAE is more accurate and robust as a measure of models' ability to reproduce reality. The MAE is defined as:

$$MAE = |\bar{d}| = \frac{1}{N}\sum_{i=1}^{N}|d_i| \tag{3.3}$$

One measure often used to verify the accuracy of numerical models is the Mean Square Error (MSE) (WILKS, 2006). Unlike the MAE, the MSE is more sensitive to large errors because it is squared. Therefore we have:

$$MSE = \frac{1}{N}\sum_{i=1}^{N}(d_i)^2 \tag{3.4}$$

In addition to the MSE, the square root of the MSE value can be removed and the values of the model accuracy can be obtained in the units of the variables, thus the RMSE or Root Mean Square Error, defined as:

$$RMSE = \left[\frac{1}{N}\sum_{i=1}^{n}(d_i)^2\right]^{\frac{1}{2}} \tag{3.5}$$

However, the above errors are not limited, not reporting on the relative size of the differences. The index of Agreement (IA), proposed by (WILLMOTT, 1982), has this property ($0 \leq IA \geq 1$) where $IA = 0$ is the worst accuracy and $IA = 1$ the model simulation is identical to observe and can be used, for example, to compare different simulations of the same phenomenon. IA is defined by:

$$IA = 1 - \frac{\sum_{i=1}^{N}(X_{is} - X_{os})^2}{\sum_{i=1}^{N}(|X_{is} - \bar{X}_{os}| + |X_{os} - \bar{X}_{os}|)^2} \tag{3.6}$$

It is worth noting, the realism of a simulation depends on several stochastic factors of the mesoscale simulations, which increases as the spatial scale of the numerical domain decreases (ANTHES, 1983). Verification statistics may indicate a poor outcome, even though the simulations are quite realistic (ANTHES et al., 1989). The simulated and observed data were compared directly on the hourly scale, with no filter or correction applied to the COAWST model.

3.5 PARAMETERS SEQUENCE

The use of ocean-atmospheric coupled models has the premise of improving the numerical resolution and sea-air interaction processes between the atmospheric and the oceanic numerical environment. The coupled WRF-ROMS model in this work was configured to have feedback between predicted variables of both systems in each 10 minutes time-step. At that first moment, the difference in the initial configuration of the simulations is observed. While today the predictions by the WRF model use a static SST during the entire simulation period, in the coupled model, this SST is constantly updated.

The COAWST system exchanges only the predictive variables, while the diagnostic variables are calculated by each separate component (WARNER et al., 2010). Based on this, the WRF model will provide trends to the ROMS of the temperature, relative humidity, wind components, atmospheric pressure, cloud fractions, short and long wave radiations values an net heat values. ROMS in turn, assimilates the predicted data and provides the SST forecast to the WRF (WARNER et al., 2010; ZAMBON; HE; WARNER, 2014).

In general terms, the WRF solves the exchanges of the surface fluxes and the structure of the boundary layers by a set of three parametric routines. Together, the resolutions of the vertical fluxes of heat and humidity, by the transport of vortexes in the Planetary Boundary Layer (PBL); The friction velocity and exchange coefficients allow calculations of heat fluxes in the surface atmosphere over oceanic waters Surface Physics (SF); The variables of state and surface properties, providing heat and moisture fluxes on land surfaces Land Soil Model (LSM) (SKAMAROCK et al., 2008).

Due to this structure the WRF will simulate the lower levels of the atmosphere with direct influence of the ROMS. However, due to the interaction between the PBL and the free atmosphere, it is a fact that the low level interactions will influence the medium levels. Therefore, it is valid to state that the low-level update of SST will influence the high levels of the atmosphere with a connected structure, as presented in other studies (WARNER; PERLIN; SKYLLINGSTAD, 2008; WARNER et al., 2008; RENAULT et al., 2012).

The selected physical surface parameterization (MYNN) will conduce the exchange between atmosphere and ocean interaction, influencing the model's low atmosphere processes over the ocean. It is emphasized that, over land, the resolution of the surface fluxes is given by the parameterization of (LSM) which differs in the resolutions, as well in the experiments without active fluxes. So, to understand the role of update SST differs from traditional simulations, the process to calculate surface fluxes in MYNN are shown. The first moment, the parameterization calculates the saturation pressure e_s by:

$$e_s = 0.611 \exp^{\left(17.67 \frac{(SST-273.15)}{(SST-29.65)}\right)} \tag{3.7}$$

SST - the Sea Surface Temperature.

In this step, the SST is already a fundamental variable to predict the water vapor content and the moisture rate. Thus, the specific humidity for the first level of the atmosphere is obtained by:

$$q_{sfc} = 0.622 \frac{e_s}{(P_{sfc} - 0.378 e_s)} \tag{3.8}$$

and the Moisture Rate

$$RM_{sfc} = 0.622\frac{e_s}{(P_{sfc} - e_s)} \tag{3.9}$$

P_{sfc} - Surface Pressure

After finding the superficial values for moisture, it starts to calculate the dynamic values for the moisture fluxes in the initial layers of the atmosphere, being calculated the moisture coefficient of exchange by:

$$FLQC = \rho M_{avail} U^* \frac{\kappa}{PSIQ} \tag{3.10}$$

ρ - density;

M_{avail} - Available humidity;

U^*- u^* in similarity theory;

κ - Von Karman constant;

$PSIQ$ - Humidity Resistance

At this moment, it is possible to verify the influence of instabilities and dynamical factors for Latent Heat. As an example, there is a U^* - u^* in similarity theory - which is function of the wind speed. In this case, we can see the first influence of update SST and the stability in the PBL. Thus, for the next step, the vertical moisture gradient is verified to find the the upward motion of water vapor (Evaporation):

$$Q_{fx} = FLQC(RM_{sfc} - q_v) \tag{3.11}$$

RM_{sfc} - Surface Moisture Ratio;

q_v - First level above surface Water Vapor

Finally, its possible to find the Latent Heat by multiplying the water evaporation latent heat constant.

$$LH = LHV * Q_{fx} \tag{3.12}$$

LHV - Water Evaporation Latent Heat .

Similar to the q_s, the first value of potential temperature is calculate in half first η level, which is in equilibrium with the near surface ocean air temperature. Due this, the first potential temperature is a function of SST, such as:

$$\theta_{gb} = SST\left(\frac{100.}{P_{sfc}}\right)^{\frac{R}{C_p}} \tag{3.13}$$

After find the first value of potential temperature, it's necessary find the exchange coefficient for heat by:

$$FLHC = c_{pm}\rho U^* \frac{T^*}{(\theta_{\frac{1}{2}\eta} - \theta_{gb})} \tag{3.14}$$

Finally the sensible heat flux:

$$HFX = FLHC(\theta_{gb} - \theta_{\frac{1}{2}\eta}) \tag{3.15}$$

The COAWST model has two types of procedure in resolve heat fluxes. The first one is each model calculating the fluxes with its own parameters, and second one the WRF providing the net heat budget to ROMS (ZAMBON; HE; WARNER, 2014). The first procedure can generate inconsistent values of latent and sensible heat fluxes. Thus, in the first methodology, the ROMS calculates the flux by its own parameters, receiving the forecasted values of the meteorological variables.

According to the computational algorithm of the meteorological variables of the ROMS model, the relationship between surface structure and surface fluxes are strictly related to each other, where higher (lower) temperature loss and humidity to the atmosphere occurs in the environment of higher (lower) gradient (thermal and moisture) between ocean and atmosphere (FAIRALL et al., 1996), in which:

$$H_s = \rho_a c_{pa} C_h S(T_s - \theta) \tag{3.16}$$

$$H_l = \rho_a L_c C_e S(q_s - q) \tag{3.17}$$

$$\tau_l = \rho_a C_d S(u_s - u) \tag{3.18}$$

ρ_a - Air Density

c_{pa} - Dry air specific heat

C_h - Heat transfer coefficient

S - Averaged wind speed

T_s - Surface sea temperature

θ - Potential temperature

L_c - Evaporation latent heat

C_e - Moisture transfer coefficient

q_s - Surface saturated moisture rate

q - Water vapor moisture rate

C_d - Wind stress coefficient transfer

u_s - Surface sea streamflow

u - u-wind component

Due to a possibility to have inconsistent latent and sensible heat fluxes. The second methodology was used. So the net heat budget is calculated in WRF and drives the ROMS SST forecasting.

Therefore there is a feedback procedure in the coupled system in which the fluxes calculated by WRF receive the SST information from ROMS. So, the temperature, relative humidity, wind components, atmospheric pressure, cloud fractions, short and long wave radiation values, forecasted by early SSTs, will be provided to ROMS to forecast the next SST values. With this, the main issues, is to how the coupled model ocean-atmosphere influence in the simulations were healed. However, the question of response time is still open, since the ocean has slower variations than the atmosphere.

However this issue is already explained in Skamarock et al. (2008), for example, after the simulation of the surface variables, the results obtained in each surface parameterization will be sent to other physics, such as in the Planetary Boundary Layer (PBL), Convective (CU), Cloud Microphysics and Radiation (SW and LW) (GOPALAKRISHNAN et al., 2012).

Therefore, the updated SST promoted by WRF-ROMS exchange will have an impact on the resolution of MABL instabilities, cloud formations, radiation, and other processes that act rapidly in the atmosphere, which will impact the simulations of meteorological systems (RENAULT et al., 2012).

4 RESULTS

4.1 VALIDATION

To validate the prognostic variables, three representative points in the domain were chosen. The first point is over the ocean at 8°S 30°W in the PIRATA buoy. The second point in the coastal region, Recife - PE at 8.5° 35° W. The third point is Garanhuns in the *Agreste* (Semiarid Region) of Pernambuco (8.9° 36.5°W), located on the Borborema Plateau with elevation of 830m above sea, and above 230 km from sea.

4.1.1 Air Temperature and Relative Humidity 2m

In the PIRATA buoy, the results obtained show temperature near to the measured in the all experiments (Figure 10a). The BIAS for this region shows a pattern of discrepant values mainly in days under influence of the meteorological system in that area (days 14 to early 18 of June), and days with temperature peaks in 11, 20 and 21 of June (Figure 10b).

In the coastal area represented by Recife *Plataforma de Coleta de Dados* (DCP) Station (Figure 10c) we can see good agreement with WRF-ROMS 2, WRF 2, WRF-ROMS 3 and WRF 3 and a cooler atmosphere in WRF-ROMS 1 and WRF 1. The BIAS in Figure 10d, shows the same characteristics in temperature for the buoy, but with more intensity. In the first discrepancy, there was an influence of a frontal system which took down the maximum temperature in the day 13. This system, at first moment couldn't be simulated for all experiments, and the Bias reached 5° of anomaly. In the next days, the model simulated the real conditions, but the temperature still was overestimating the surface temperature.

In the *Agreste* Region, the values are similar for experiments with fluxes (Figure 10e). In contrast with Recife, the region presented smaller Bias than in the previous station (Figure 10f). The results show that there are peaks of overestimating in the three areas of measurements, mainly due to the influence of the meteorological system. However, the experiments WRF-ROMS 1 and WRF 1 have simulated a cooler atmosphere over the land region. It can be explained due to less amount of water vapour in the atmosphere in absence of fluxes in ocean.

For Relative Humidity, it is possible to verify the drying of atmosphere over the ocean region in the experiments WRF-ROMS 1 and WRF 1. It is explained by the relationship between the warm ocean temperatures (previous result) and low available amount of water vapour (Figure 11a, b). In conditions of warmer air temperature, it is capable to hold more water vapour, in this case, in RH2m there is lower water vapour content. It also explains why Recife (Figure 11c, d) and Garanhuns (Figure 11e, f) have RH2m near to the observed, the colder atmosphere makes the relation close to the measurements.

Figure 10 – Time Series of air temperature in 2m for a) Garanhuns; b) Recife and c) PIRATA Buoy (8°S e 30°W); and Bias (simulated - measured) for d) Garanhuns e) Recife and f) measured at PIRATA buoy (8°S e 30°W)

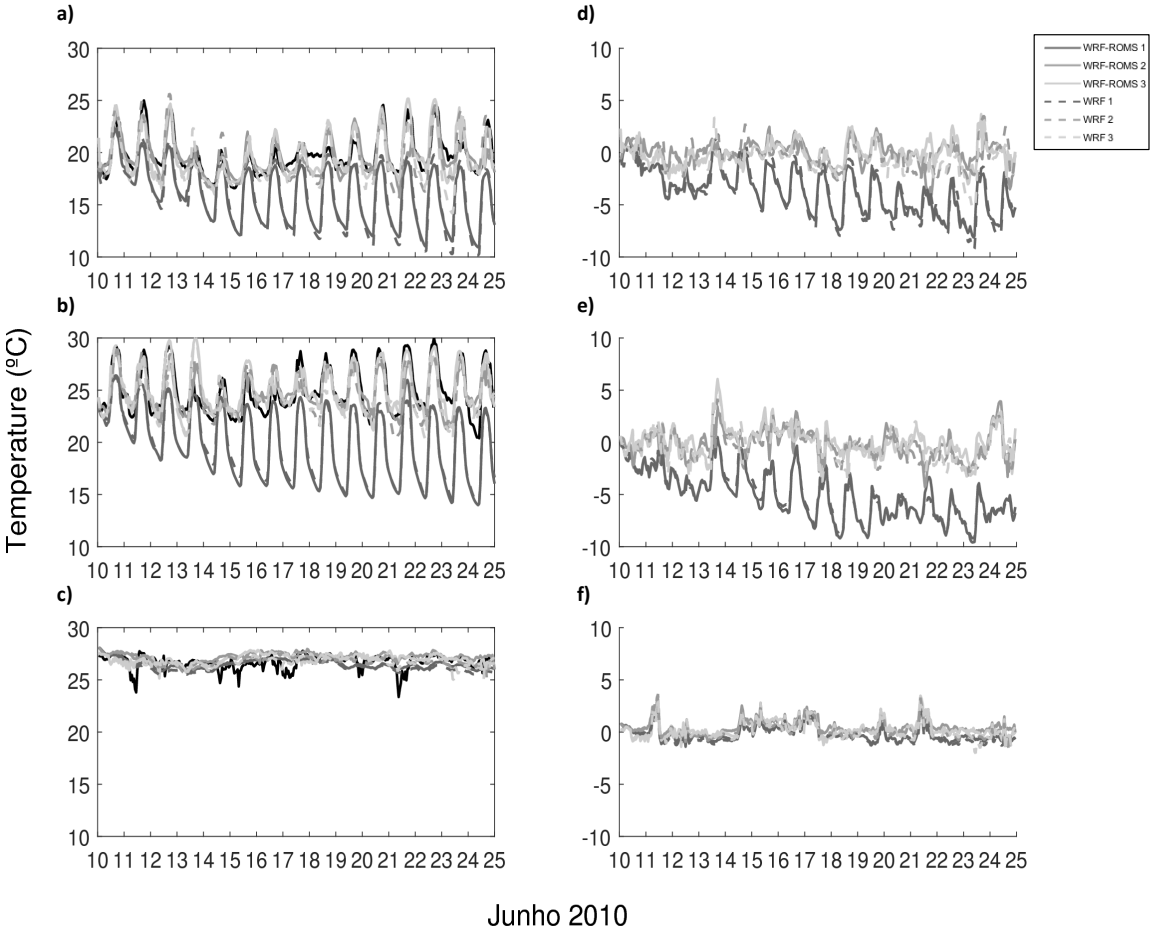

Source: The Author

There is a low Bias for all observed stations. In the oceanic region, in contrast with T2m results, the RH2m presented no discrepancy with observations, under influence of meteorological system over ocean (Figure 11a, b). However, there is a daily and consistent Bias discrepancy for Recife (Figure 11c, d), mainly during the daily period, where this region presented dryer atmosphere than simulated.

For Garanhuns (Figure 11e, f), during the EWD had lower Bias in the WRF-ROMS 2, WRF 2, WRF-ROMS 3 and WRF 3 experiments. The near 100% of the measured values were well represented in the simulated experiments. However, the RH2m values in the experiments WRF-ROMS 1 and WRF 1 were underestimated.

The results for WRF-ROMS 1 and WRF 1 appointed that, the Latent and Sensible heat release, influence on land surface of the atmospheric model, both can be a essential key to improve simulations, not only in the ocean but in the surrounded land region. However, it can be

Figure 11 – Same as Figure 11, but for Relative Humidity

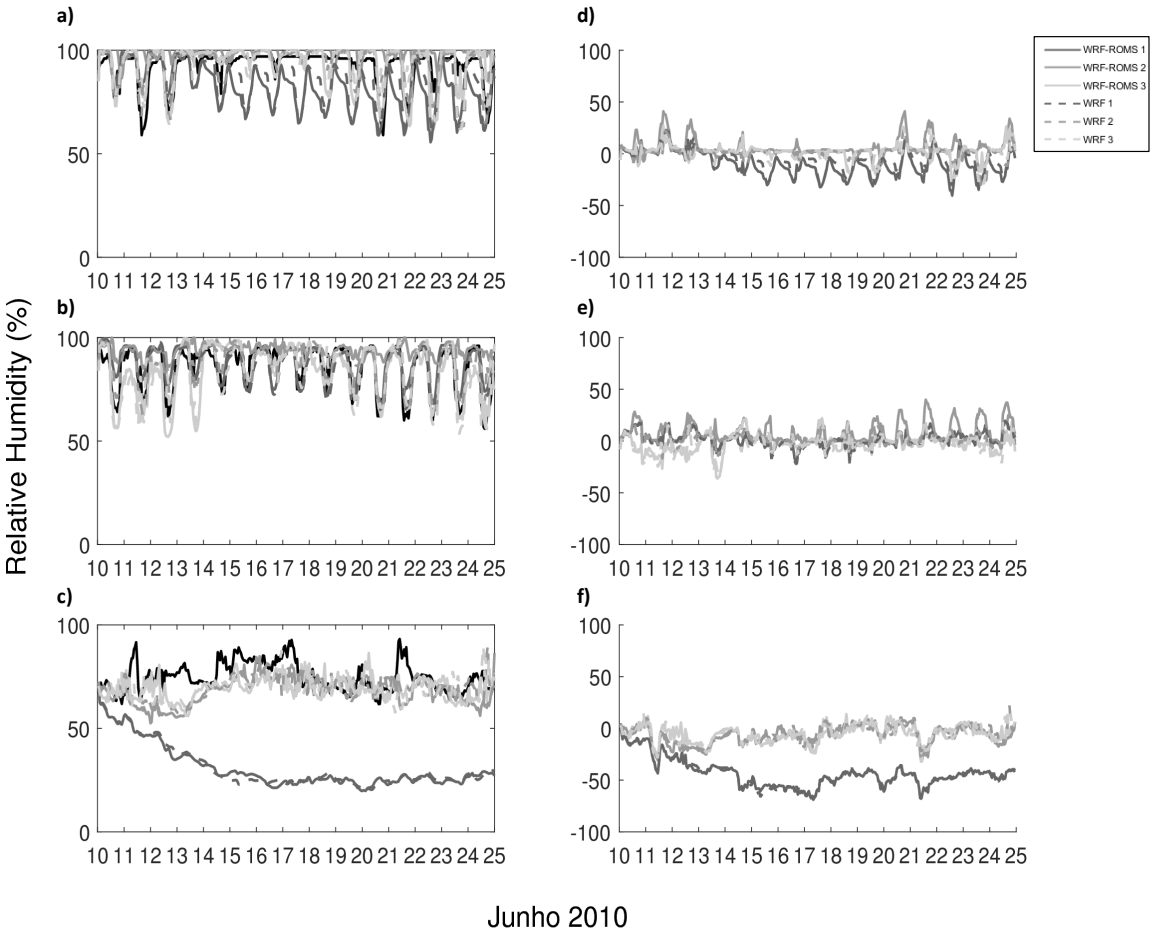

Source: The Author

observed also, similar discrepancy between WRF-ROMS 2 and WRF 2 or WRF-ROMS 3 and WRF 3. It means that the effects of the coupling don't change the entire dynamics of the model, but the resolution of diagnostic fields.

4.1.2 Wind components at 10m

There isn't a direct influence of SST on the WRF parameters resolution, such as the Latent Heat calculation, so the dynamical values are investigated. The values of wind speed drive the intensity of heat fluxes by the U^* parameter, and also its carries water vapour from the ocean to the land. But, in the larger domain, the SST will influence the wind speed, which in turns will affect the heat fluxes exchanges.

For the zonal wind component (u_{10m}), it is possible to verify a pattern similar to the observed in the ocean site (Figure 12a, b). There is a discrepancy in time-series Bias for all experiments with same pattern. WRF-ROMS 1 and WRF 1 don't modify the dynamics, as

Figure 12 – Same as Figure 10, but for u_{wind} speed

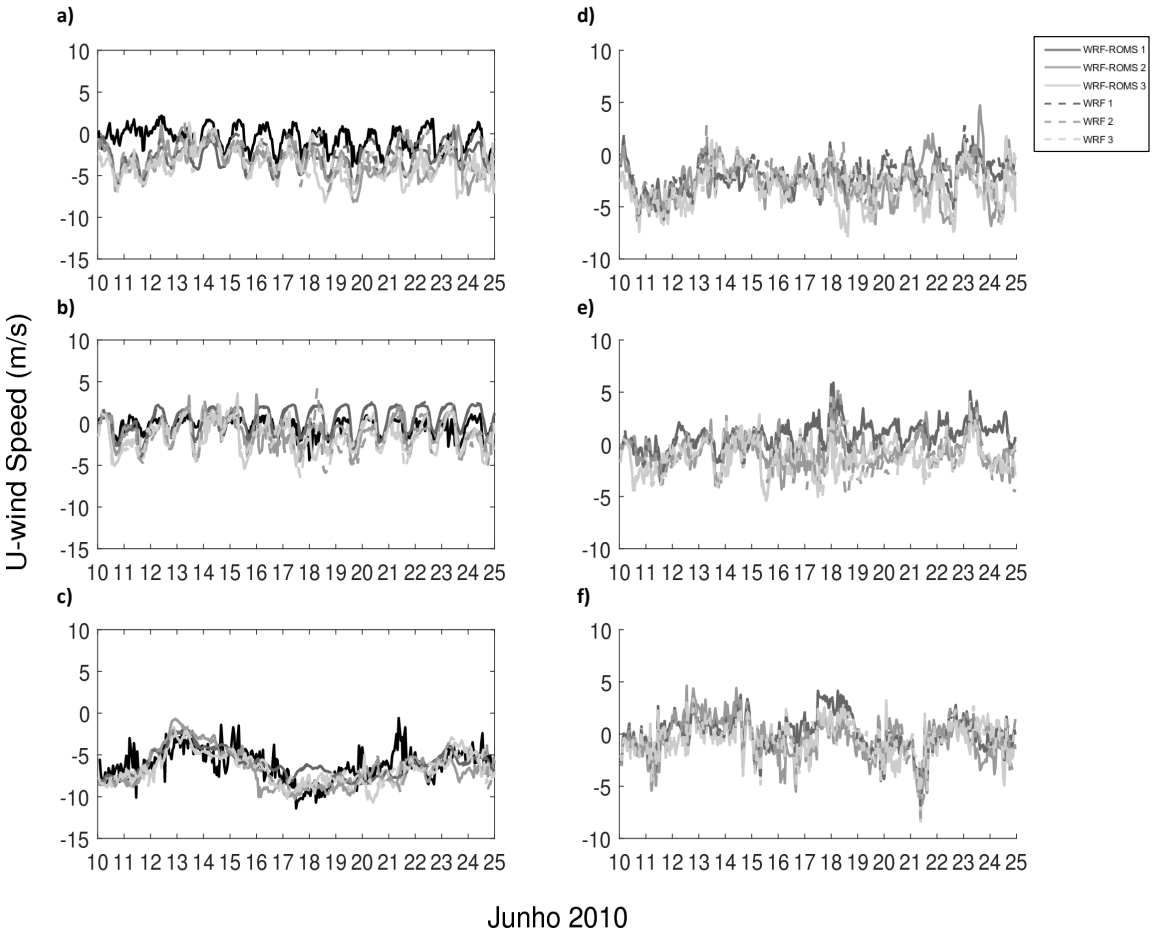

Source: The Author

showed for T2m and RH2m, however, some deviations can be observed for these experiments. For example, in Recife station (Figure 12d) there is higher Bias for WRF-ROMS 1 and WRF 1 after 14 June. Nevertheless its deviation it wasn't observed for the Buoy and for Garanhuns (Figure 12b and 12f respectively).

For Recife there is a small Bias pattern, where the flows are consistent with the measurements in the entire period (Figure 12c, d). But, there is a disagreement between all experiments under influence of meteorological system (days 15 to 18 of June). The patterns of all experiments had changed, showing that the meteorological system influenced the simulations in different ways.

The Garanhuns stations (Figure 12e, f) detected that the system acted with less intensity than in Recife. It is possible to verify a daily deviation for u_{10m} (zonal component) similar in all experiments. Basically there was an overestimating of the westward (negative u_{10m}) flow over the land, which means stronger zonal flux intensity present in all experiments.

Figure 13 – Same as Figure 10, but for v_{wind} speed

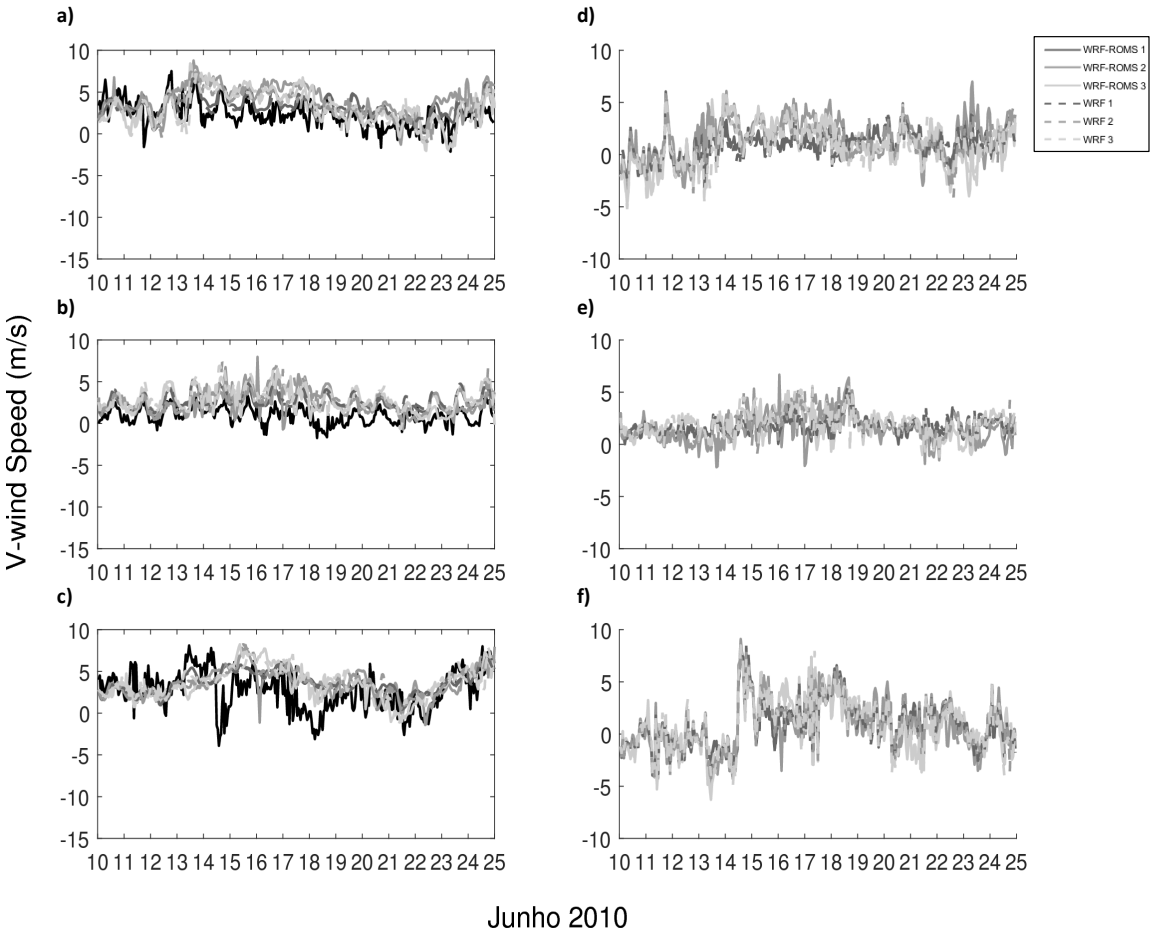

Source: The Author

For the v_{10m} (meridional wind component) over the ocean (Figure 13a, b), it's possible verify more discrepancy between observed and measured values than in the u_{10m}. The highest variation occurred in 15 June, under influence of the meteorological systems. During day 14 to 19 of June, the values of v_{10m} presented higher values of Bias. It means that the model overestimated northward flows of surface winds.

In Recife (Figure 13c, d), similar pattern was also identified. The period between 15 to 19 of June presented an increasing in the anomaly of northward flows (v_{10m}) under influence of the meteorological system. However in days early and after the system, the Bias turn to be overestimated with less intensity.

For Garanhuns (Figure 13e, f), there are lower anomalies in simulations, associated to a weaker meteorological system in this area. But, its is still more intense than Recife in the entire time-series.

We observe underestimated values of the wind speed over oceanic areas (Figure 14a, b),

Figure 14 – Same as Figure 10, but for wind speed

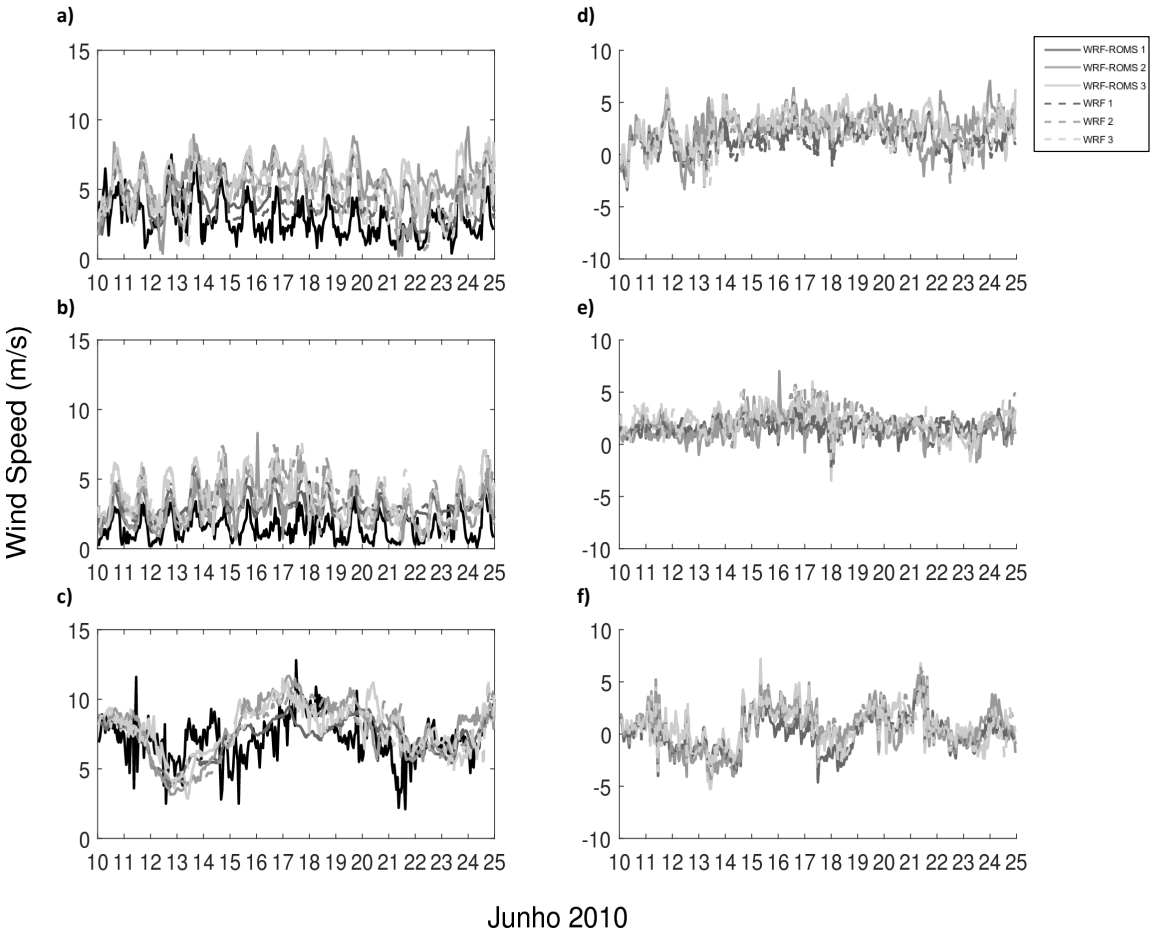

Source: The Author

and overestimated (Figures 14c, d, e, f) over land areas. The main influence of these overestimation is due to high positive anomalies of the v_{10m} component over the land regions. These influence occur mainly in the period between 15 and 19 of June, which correspond to the presence of the meteorological system.

The dynamical pattern of all wind components is in agreement in all experiments. The results show that the heat fluxes in the simulations didn't change the wind forecast, such as the T2m and RH2m. But, it possible to verify small difference in u_{10m}, v_{10m} and in the magnitude of the wind, mainly in daily maximum and minimum, comparing all experiments. It can be explained by feedback effect of the updating SST, changing the fluxes, that will change the MABL structure. This, on the other hand, is an indirect consequence of the SST updating.

Though, it is relevant to emphasise the relationship between U^* and the fluxes. In an environment with high (lower) values of U^* there is a tendency of more (less) heat exchange in MABL. Thus, it is important to verify the pattern of wind components in coupled simulations.

Also, its important to verify the instabilities in the MABL structure which is more turbulent and buoyant due to more latent heat release, affecting the wind speed in the models (CHELTON; XIE, 2010).

4.1.3 Statistics Results

For the analysis of the mean averaged model score, it was used 18 measurement stations, in which 14 are over the land (INMET) and other 4 over the ocean, in the (PIRATA) Buoys. It was made an area average covering different regions, where the ocean is the average for ocean stations (PIRATA), coastal area is for PCD placed near coast and the land regions are stations placed more then 50 km from coast areas. The stations in land is provided from INMET PCDs.

Tables 1, 2 and 3 show the statistical validations of the experiments for T2m and RH2m for Ocean, Land and Coastal areas. The results obtained show small improvements for 2m temperature in ocean regions and small variations in the Index of Agreement (IA) for both variables between coupled and uncoupled experiments.

The ME and RMSE varied more strongly in the simulations with different initial data compared with coupled experiments. This results are in agreement with Gopalakrishnan et al. (2012), which explains that the initial data influences in the meteorological structure which is the control for the simulations.

However, it was found that the coupling experiments also acted in order to vary the ME values. There is an increase of peaks of maximum and minimum values of T2m and RH2m, that were influenced by the coupling effects, as shown in previous results. Also, the larger variations is found for humidity variables for Land and Coastal areas. In Ocean area, lower differences in statistical validations between coupling experiments are presented, however for the coupled and uncoupled these differences increase.

The statistics of the zonal wind (westward flow; Tables 4, 5 and 6) are overestimated in all experiments. However for Ocean areas the flow are near to zero, showing lower discrepancies in all simulations. The statistical results for Coastal areas shows the highest discrepancies with simulations and measures. The IA for u_{10m} indicates similar values for all experiments.

For v_{10m}, northward discrepancies are presented for all experiments and areas. Similar to u_{10m}, the Ocean area presented low BIAS and RMSE for v_{10m}. Thus, the wind components are better resolve in Ocean areas than Land and Coastal areas in simulations, where the initial data are responsible to higher variations in values of BIAS and RMSE.

The westward and northward flow in the atmosphere were stronger in all experiments. The simulated wind speed also was overestimated in magnitude in all experiments. The results suggest systematic error for entire domain. The IA presents consistent values for the entire domain also, showing that the physical (u_{10m}, v_{10m}, W_{spd}) pattern didn't change significantly.

Table 1 – Validations for: 2m air temperature and 2m Relative Humidity for the model experiments in Ocean area

Experiments	T2m			RH2m		
	ME	RMSE	IA	ME	RMSE	IA
WRF-ROMS 1	−0.25	1.06	0.50	−47.10	49.91	0.10
WRF-ROMS 2	−0.18	0.92	0.53	−4.03	6.79	0.52
WRF-ROMS 3	−0.30	0.94	0.52	−2.83	5.87	0.55
WRF 1	−0.63	1.10	0.55	−45.14	47.96	0.11
WRF 2	−0.64	1.00	0.58	−1.31	5.43	0.56
WRF 3	−0.77	1.06	0.54	−1.68	5.18	0.57

Table 2 – Validations for: 2m air temperature and 2m Relative Humidity for the model experiments in Land area

Experiments	T2m			RH2m		
	ME	RMSE	IA	ME	RMSE	IA
WRF-ROMS 1	−2.17	4.36	0.49	−28.17	44.31	0.40
WRF-ROMS 2	0.85	2.44	0.74	2.32	16.46	0.60
WRF-ROMS 3	0.73	2.54	0.72	−1.68	13.06	0.67
WRF 1	−2.48	4.77	0.47	−15.56	28.44	0.54
WRF 2	0.48	2.46	0.72	−0.27	12.86	0.68
WRF 3	0.51	2.46	0.70	−3.03	13.02	0.68

Table 3 – Validations for: 2m air temperature and 2m Relative Humidity for the model experiments in Coastal area

Experiments	T2m			RH2m		
	ME	RMSE	IA	ME	RMSE	IA
WRF-ROMS 1	−3.21	4.58	0.50	−18.83	34.48	0.53
WRF-ROMS 2	0.29	1.90	0.75	1.23	18.54	0.65
WRF-ROMS 3	0.25	1.83	0.75	−1.69	16.85	0.69
WRF 1	−3.91	5.35	0.46	−24.72	29.03	0.58
WRF 2	0.07	1.79	0.75	−1.86	17.03	0.71
WRF 3	0.02	1.86	0.73	−3.39	17.38	0.68

Table 4 – Validations for: u_{10m}, v_{10m} and W_{spd} for the model experiments Ocean area

Experiments	u_{10m}			v_{10m}			W_{spd}		
	ME	RMSE	IA	ME	RMSE	IA	ME	RMSE	IA
WRF-ROMS 1	−0.20	1.63	0.70	0.64	2.18	0.70	0.29	1.50	0.68
WRF-ROMS 2	−0.12	1.76	0.66	0.83	2.46	0.65	0.42	1.76	0.61
WRF-ROMS 3	−0.31	1.60	0.69	0.54	2.15	0.70	0.42	1.52	0.67
WRF 1	−0.19	1.63	0.70	0.65	2.18	0.70	0.29	1.51	0.68
WRF 2	0.06	1.71	0.66	0.84	2.39	0.66	0.28	1.67	0.63
WRF 3	−0.28	1.51	0.71	0.48	2.10	0.71	0.32	1.42	0.69

Table 5 – Validations for: u_{10m}, v_{10m} and W_{spd} for the model experiments Land area

Experiments	U_{10m}			V_{10m}			W_{spd}		
	ME	RMSE	IA	ME	RMSE	IA	ME	RMSE	IA
WRF-ROMS 1	-0.43	2.29	0.55	1.59	2.36	0.54	1.85	2.51	0.54
WRF-ROMS 2	-1.57	2.64	0.52	2.24	3.09	0.45	2.78	3.48	0.43
WRF-ROMS 3	-1.67	2.77	0.50	1.93	3.00	0.47	2.68	3.48	0.43
WRF 1	-0.37	1.98	0.59	2.03	2.88	0.54	1.86	2.57	0.55
WRF 2	-1.27	2.38	0.54	1.81	2.77	0.50	2.26	3.09	0.48
WRF 3	-1.45	2.47	0.52	1.58	2.68	0.51	2.21	3.03	0.48

Table 6 – Validations for: u_{10m}, v_{10m} and W_{spd} for the model experiments Coastal area

Experiments	U_{10m}			V_{10m}			W_{spd}		
	ME	RMSE	IA	ME	RMSE	IA	ME	RMSE	IA
WRF-ROMS 1	-0.56	2.98	0.53	1.40	2.55	0.57	1.89	2.93	0.54
WRF-ROMS 2	-2.28	3.58	0.49	1.56	2.90	0.53	2.45	3.54	0.48
WRF-ROMS 3	-2.48	3.70	0.48	1.59	2.95	0.54	2.71	3.68	0.47
WRF 1	-1.54	3.85	0.49	1.82	2.67	0.56	2.56	3.36	0.50
WRF 2	-2.26	3.59	0.49	1.72	2.96	0.54	2.57	3.61	0.48
WRF 3	-2.40	3.66	0.49	1.66	3.07	0.52	2.65	3.72	0.47

4.1.4 Precipitation

The effects of the coupling between meteorological and oceanic models were observed in the precipitation simulations, as shown in Table 3. The results shows that, the absence of heat and moisture exchange in sea-air interface (WRF-ROMS 1 and WRF 1) was the main responsible to simulate absence of rainfalls in ENEB.

It can be observed that the coupling effect improved the simulations of amount of rainfalls, in which the coupled models presented more realistic results. Also, the FNL data-set generates better results for the simulations, leading to forecasting the high amount of rainfalls.

In the experiments WRF-ROMS 2 and WRF-ROMS 3, a higher amount of precipitation was observed than in the WRF 2 and WRF 3, without coupling, even approaching the values recorded in the meteorological events in the ENEB of the period.

The conclusion of the statistical analysis is that the updating SST, of the coupled model, acts directly in heat exchange and indirectly in the wind components. The exchange of the predict variables between WRF and ROMS interacted in a way to improve the rainfall forecasting.

[1] Source: EMPARN
[2] Source: AESA
[3] Source: APAC
[4] Source: INMET

Table 7 – Difference between simulated and observed values in different rain gauges in the ENEB.

Município	Lat ; Lon	WRF-ROMS 1	WRF 1	WRF-ROMS 2	WRF 2	WRF-ROMS 3	WRF 3
Natal - RN[1]	-5.83 ; -35.20	-131.5	-131.2	15,9	-74.8	-39.7	-100.3
Vila Flor - RN[1]	-6.31 ; -35.07	-144.8	-144.9	8.0	-91.1	-19.4	-107.1
João Pessoa - PB[2]	-7.08 ; -34.83	-174.4	-176.6	27.3	-22.5	-99.9	-92.1
Gado Bravo - PB[2]	-7.59 ; -35.83	-157.0	-152.0	-32.7	-97.7	-63.3	-126.0
Recife - PE[3]	-8.05 ; -34.95	-431.5	-432.1	-54.9	-251.4	-191.9	-346.9
Garanhuns - PE[3]	-8.88 ; -36.48	-194.4	-196.1	-32.9	-65.0	-126.5	-127.1
S. L. do Quitunde - AL[4]	-9.28 ; -35.56	-249.2	-249.6	-65.7	-95.0	-207.9	-188.5

4.2 EXTREME RAINFALL EVENT IN 2010

In the Tropical South Atlantic basin, the thermal characteristics of the ocean surface are influenced by the surface currents forced by the trade winds. The southern branch of the South Equatorial Current (sSEC) acts as a heat transport pathway, from the eastern South Atlantic, near African coast towards western South Atlantic near the Brazilian Northeast coast (HOUNSOU-GBO et al., 2015). In the year of 2010, the registered SSTs in the PIRATA buoys (30°W; 8°S) in the western STA (WTSA) were higher than 28.5°C, resulting in anomalies above 1°C between April and June. As a result, the region behaved similar to a Warm Pool (WANG; ENFIELD, 2001; WANG et al., 2006; WANG; LEE, 2007; HOUNSOU-GBO et al., 2015; CINTRA et al., 2015), hereafter called South Atlantic Warm Pool (SAWP), during this period.

Figure 15 presents the initial and final conditions of SST and surface currents, where we identify, at the beginning of the simulations, the SAWP region with SSTs above 28.5 °C (Figure 15a). In comparison, in the eastern TSA, the SSTs were below 25 °C, developing an intense SST zonal gradient in southeastern Atlantic ocean basin.

In the last time-step of the simulation, a slight cooling of the surface waters in the SAWP region was observed (Figure 15b). In the northeast of the TSA basin, the temperatures decreased with higher intensity than in the SAWP. The SST cooling occurred in the areas with strongest currents in northeast TSA basin. The changes in the SST patterns in the western TSA showed a reduction in area of the SAWP. These changes can be reflected by heat losses to the atmosphere (FOLTZ; MCPHADEN, 2006), which are investigated further in this work.

4.2.1 SAWP

The buoys in TSA, from the PIRATA project, were used to validate the ROMS results. The buoy at 30°W - 8°S was used to verify the capability of WRF-ROMS to simulate the surface, mixed layer and thermocline in the SAWP. It was compared to the simulated values of ocean temperature up to 500m depth in the coupled modeling experiments WRF-ROMS 1, WRF-ROMS 2 and WRF-ROMS 3, as shown in Figure 16. The Hovmöller of temperature show the comparison between in situ and simulations (Figure 16). The simulated temperatures below the mixed layer (100m depth), have similar patterns in the three experiments, with temperatures

Figure 15 – Sea surface temperature and surface currents simulated with the WRF-ROMS 2 experiment, a) in 10 June 2010 at 0000 UTC and b) 25 June 2010 at 0000 UTC.

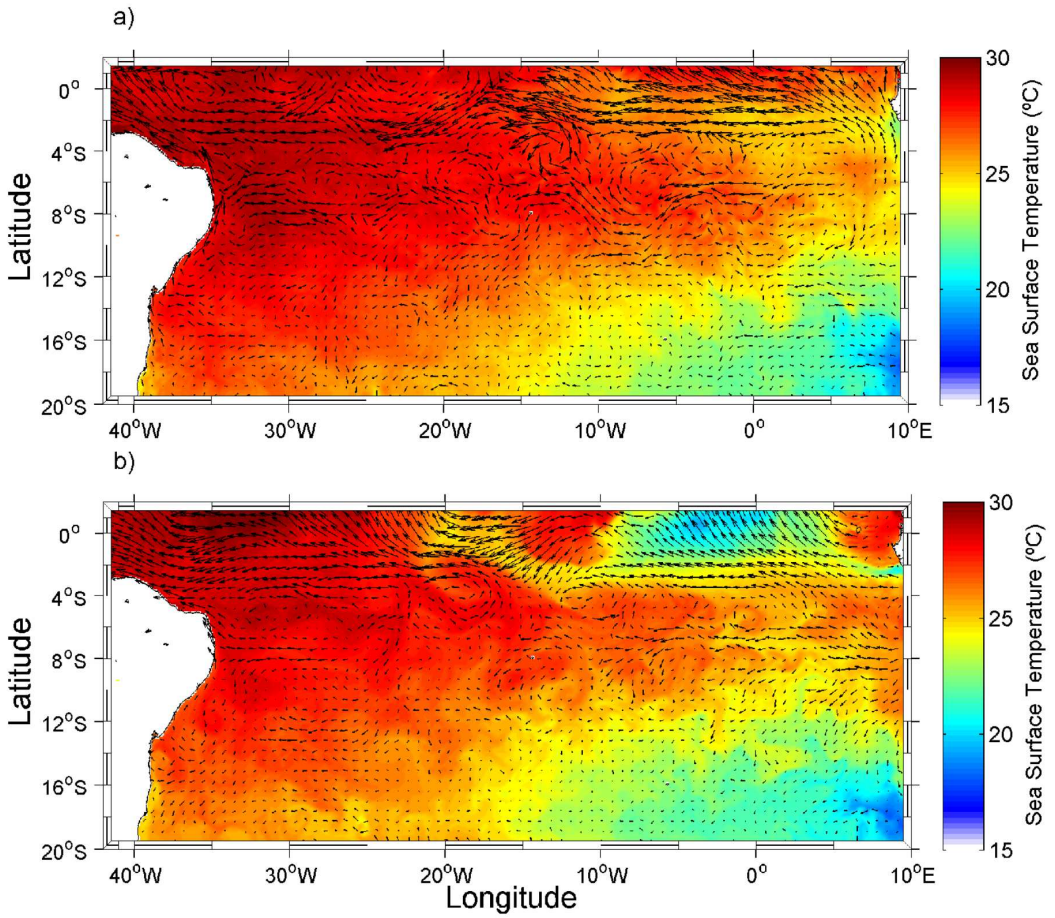

Source: The Author

close to the measurements, verifying that the coupled model was able to represent near real thermal structure conditions (Figure 16).

Below 250m depth, the difference between measurements and simulated temperature results is about -0.4°C. Moreover, near the surface, it was observed that, in the experiment WRF-ROMS 1 there is a warming of the surface waters, whereas in the experiments WRF-ROMS 2 and WRF-ROMS 3 there is a cooling in the ocean mixed layer, showing the SAWP response due to heat fluxes to the atmosphere. This cooling is evidenced in Figure 2, at the end of the simulation, showing the relationship between heat losses and moisture releases to atmosphere in the SAWP region.

The SAWP mixed layer temperatures in WRF-ROMS 2 (Figure 16b) are higher than in WRF-ROMS 3 (Figure 16c), evidencing the impact of the different input databases in the upper ocean. This difference can be interpreted due different atmospheric conditions developed by these different initial conditions (GOPALAKRISHNAN et al., 2012; LI; PU, 2014). Therefore, these simulations are consistent with previously published works (WANG; ENFIELD, 2001; WANG et al., 2006; WANG; LEE, 2007; FOLTZ; MCPHADEN, 2006; HOUNSOU-GBO et al., 2015;

Figure 16 – Hovmöller from ocean temperatures at 8°S 35° W, from the PIRATA buoy (white lines) and a) experiment WRF-ROMS 1, b) experiment WRF-ROMS 2, c) experiment WRF-ROMS 3 (black lines and color shading), from 10 to 25 June 2010.

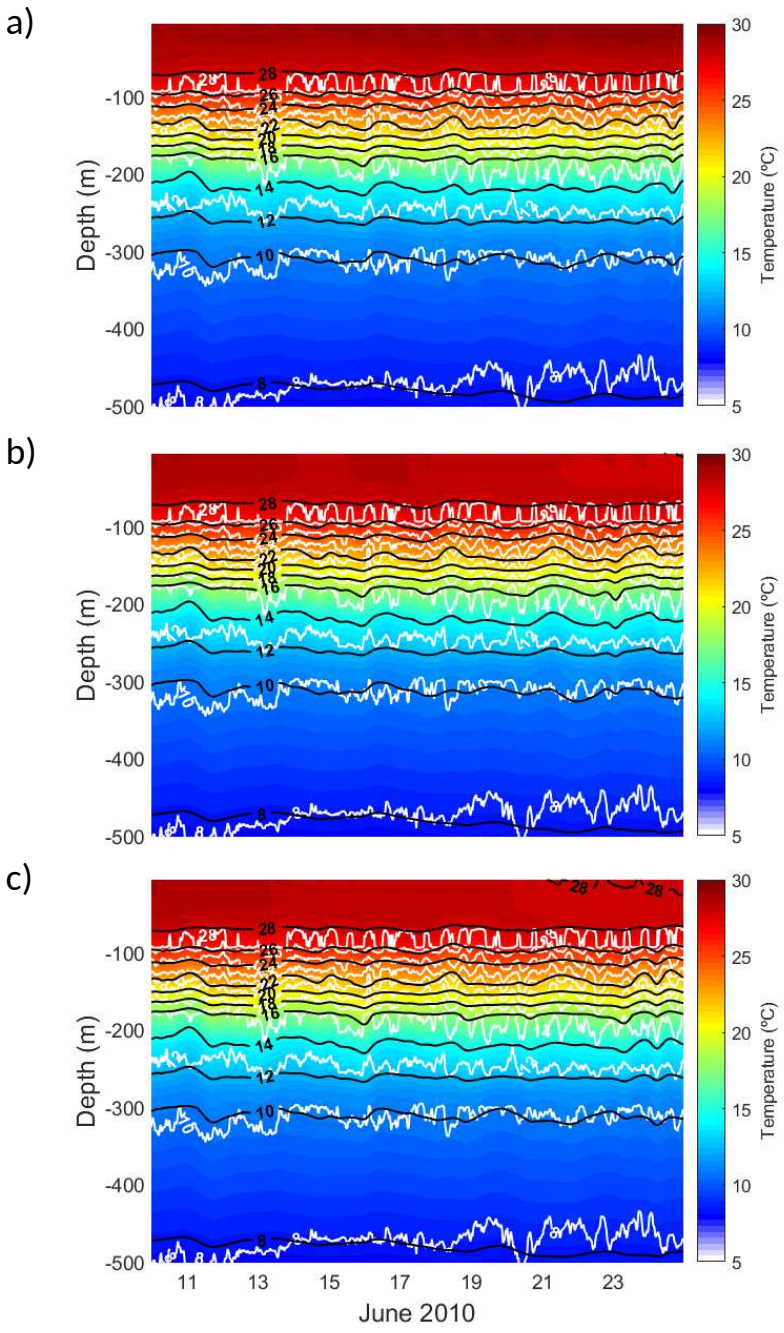

Source: The Author

CINTRA et al., 2015), which show the relation between heat fluxes at the ocean-atmosphere interface and feedback processes, acting as the main mechanism to reduce or increase the thermal variations in the SAWP.

4.2.2 Atmosphere–ocean interactions

The results showed that, the oceanic temperature was influenced by heat and moisture fluxes in the initial data. To verify how these changes acted in the simulated atmospheric structure, we compare the results of the WRF-ROMS with WRF and their respective experiments.

4.2.2.1 Experiments without sensible and latent fluxes

The Figure 17 a, b, c shows a time averaged (10 to 25 June 2010) vertical profile of low-medium troposphere (1000hPa to 600hPa) and ocean depth (0m to 500m), over a integrated area between the 10°S - 5°S and 41°W - 10°E, for WRF-ROMS 1, WRF-ROMS 2 and WRF-ROMS 3 respectively. Figure 17 d,e,f,g shows the difference between WRF-ROMS 1 and WRF 1, WRF-ROMS 2 and WRF 2, WRF-ROMS 3 and WRF 3, and WRF-ROMS 2 and WRF-ROMS 3 respectively.

As a result of the absence of heat exchange and mixing processes between ocean and atmosphere, a low water vapor environment over the Atlantic Ocean was obtained in experiments WRF-ROMS 1 and WRF 1 (Figures 17a and 17d). However, WRF-ROMS 1 simulated a drier atmosphere than only WRF 1, except over the continent. This difference occurs due to warmer atmosphere simulated by WRF-ROMS 1 with absence of upward moisture fluxes. In addition, the WRF-ROMS 1 simulated warmer upper ocean waters over entire longitudinal domain, mainly in the SAWP region, compared with WRF-ROMS 2 and WRF-ROMS 3.

4.2.2.2 Experiments with sensible and latent fluxes

The mean vertical structure of water vapor in the WRF-ROMS 2 and WRF-ROMS 3 corroborate with results in Schubert et al. (1995), where in the western TSA they also found an higher moisture layer over warmer SST. In opposite, in the eastern TSA, the results show less moisture over colder waters (Figure 17b, c). This means that structures of SST and water vapor are directly linked to a deep (shallow) Marine Atmosphere Boundary Layer (MABL) over SAWP (upwelling) regions.

Comparing the WRF-ROMS 2 and WRF-ROMS 3 with WRF 2 and WRF E3, we observe a moister near surface atmosphere over entire longitudinal profile, in both WRF-ROMS 2 and WRF-ROMS 3 than WRF 2 and WRF 3 experiments (Figure 17e, f). The results show that the coupling experiments simulated more moisture in the troposphere, and over the eastern TSA the water vapor is confined in the lower levels.

Therefore, we identify that the activation of heat and moisture fluxes, modify the properties of the troposphere when comparing the coupled and uncoupled models. These differences in the simulations can modify the properties of the MABL (LINDZEN; NIGAM, 1987; KORACIN; ROGERS, 1990; SCHUBERT et al., 1995; CARRILLO et al., 2015) over the SAWP, which can cause differences in the physics of the modeled atmospheric systems between coupled and uncoupled experiments.

4.2.2.3 Coupled modeling experiments with different boundary conditions

The lower troposphere in WRF-ROMS 2 was predominant wetter and the SST was warmer than WRF-ROMS 3. In the layers above 900hPa and near 800hPa the moisture was higher in WRF-ROMS 3 than WRF-ROMS 2, but above 800hPa the moisture was higher in the WRF-ROMS 2. Also, over the continent, the entire column was more humid in WRF-ROMS 2.

The SST in WRF-ROMS 3 presented a strong cooling over the SAWP region (Figure 16c) mainly due to a lower water vapor content in the first levels of the atmosphere (Figure 17c), which favors the evaporation and latent heat losses. Unlike, the WRF-ROMS 2 simulated a moister atmosphere, extending the period with warmer SST (Figure 16b).

4.2.3 Synoptic analysis of the coupled modeling

The continuous SST updating into the atmospheric model directly influences the solving of the heat and latent fluxes, as well the consequence of those in the radiative processes, that act on the thermal structure of the ocean. In this section, we analyse the synoptic patterns of the meteorological systems, with the coupled experiment WRF-ROMS 2.

From 10 to 16 June, the atmosphere over the ENEB was influenced by the extremity of a frontal system (Figure 18), which caused rainfall exceeding 30 mm in Bahia, Sergipe, Alagoas and part of Pernambuco states. The main characteristic of this precipitation was the convergence of moisture and instabilities coming from higher latitudes. The displacement of the frontal system from 12 to 15 June is shown in the vorticity fields and streamlines at 850 and 700 hPa (Figures 18a to d, and 18i to h) and mid-levels water vapour content (Figures 18i to 18l).

During the same period, on 14 June (Figure 18c,g), we observe the development of a trough in 850hPa (Figure 18c), associated to a trough in 700hPa at northeast of the domain (Figure 18g), with atmospheric instabilities, intense convergence and cyclonic vorticity, characterizing easterly waves. The easterly wave propagates westward on following days (Figure 18 d, h and Figure 19). These waves disturbances has coupled with the previous instabilities, caused by frontal system on 15 June, as seen in the water vapour content in mid-levels (Figure 18i, j, k, l).

From 17 to 19 of June, the atmospheric disturbances caused the extreme events of rainfall leading to a flood in Pernambuco and Alagoas. The intense convective cloud system developed due to the easterly waves (Figure 19), characterized by the presence of high moisture content in

Figure 17 – Longitudinal profile, period averaged from 10 - 25 June 2010, of the atmospheric water vapor (upper) and ocean temperature (bottom) in the experiments a) WRF-ROMS 1, b) WRF-ROMS 2c) WRF-ROMS 3, difference between (d) WRF-ROMS 1 and WRF 1, (e) WRF-ROMS 2 and WRF 2, (f) WRF-ROMS 3 and WRF 3and (g) WRF-ROMS 2 and WRF-ROMS 3.

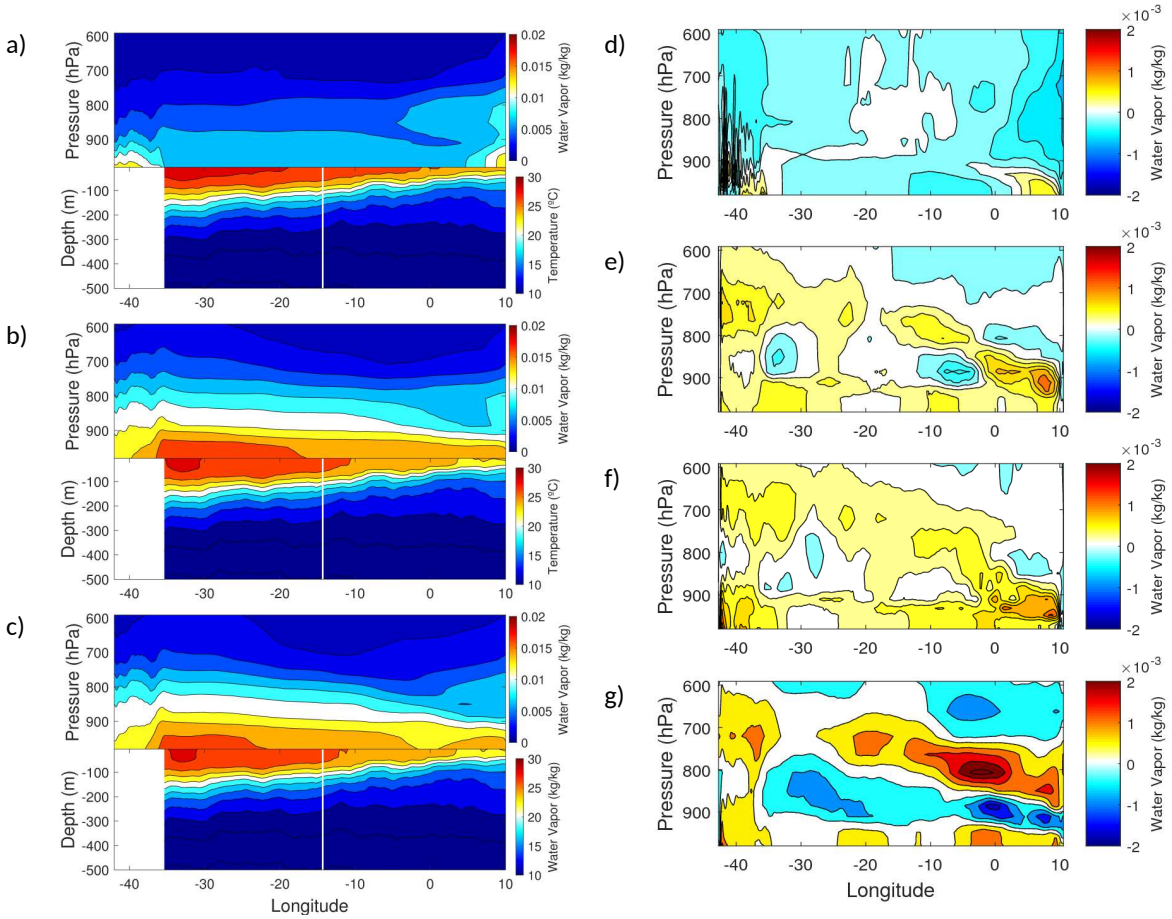

Source: The Author

medium levels (Figure 19k), together with an intense trough between 850 and 700hPa (Figure 19d, h), similar to the characteristics shown in Gomes et al. (2015).

Figure 20 show disturbances from southeast throughout the remaining period, which caused intense rainfall in the ENEB. The development of these systems, from 19 to 25 June, differed from the easterly waves occurred previously. This meteorological system was characterised by disturbances in the trade winds, coming from Southeast, where the core of cyclonic vorticity and moisture convergence were restricted in the low levels of the atmosphere (Figure 20). In these days, despite the intense precipitation, the cumuliform clouds presented low vertical development.

Figure 18 – Streamlines and vorticity from 12 June 2010 at 0000 UTC to 15 June 2010 at 0000 UTC for: 850hPa (a, b, c, d); 750hPa (e, f, g, h); and mid-levels water vapor content (i, j, k, l).

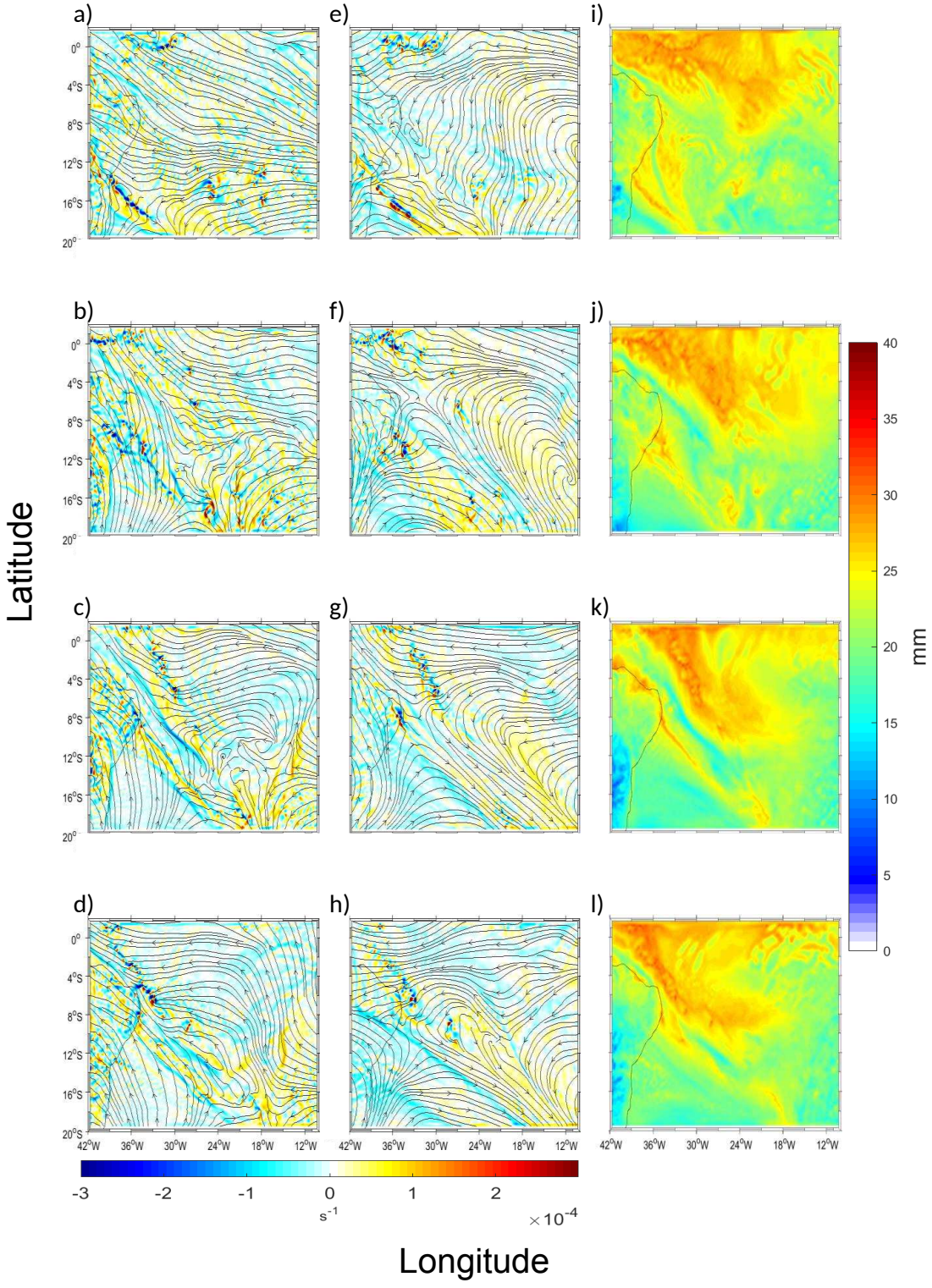

Source: The Author

Figure 19 – Streamlines and vorticity from 16 June 2010 at 0000 UTC to 19 June 2010 at 0000 UTC for: 850hPa (a, b, c, d); 750hPa (e, f, g, h); and mid-levels water vapour content (i, j, k, l).

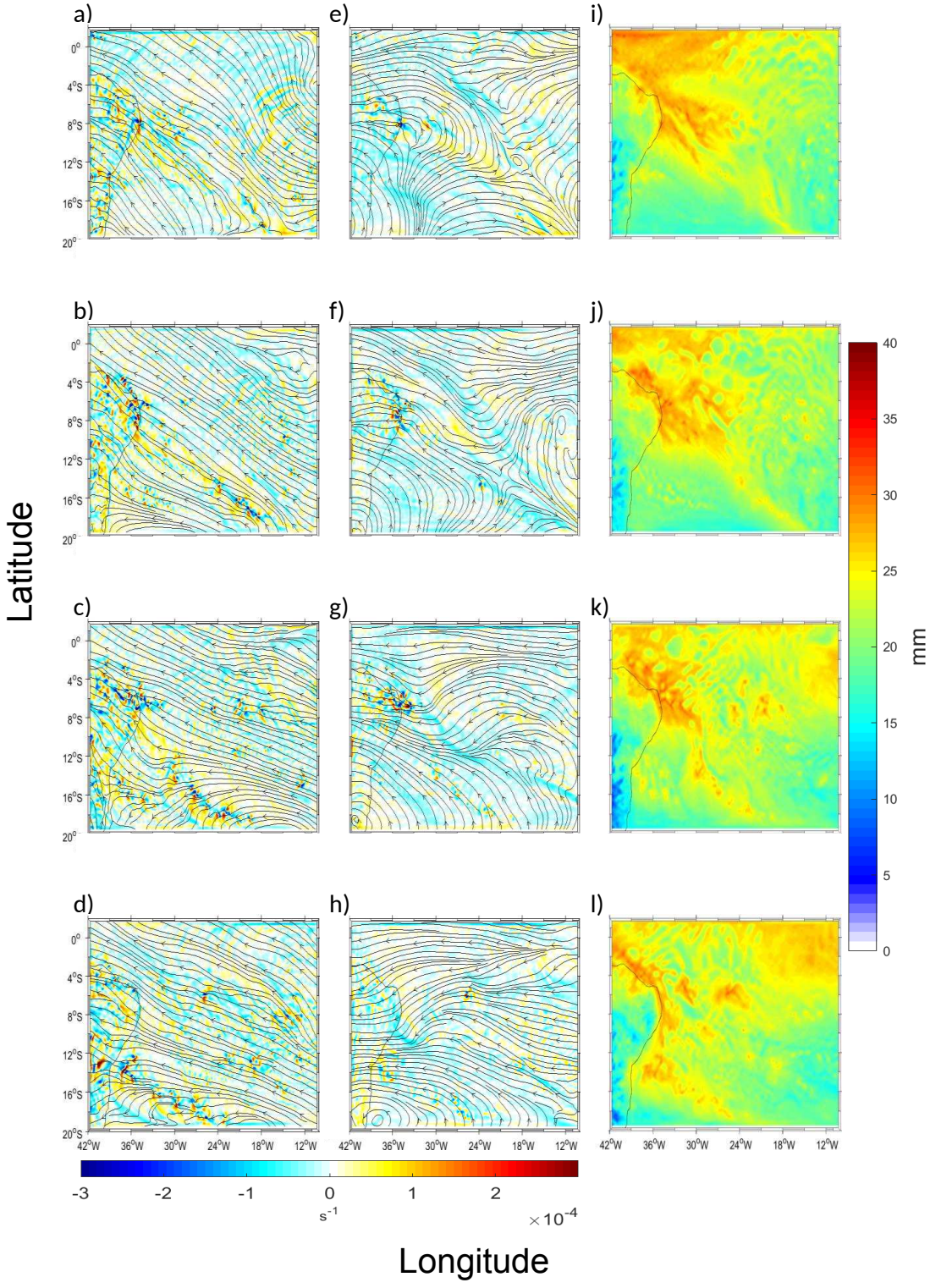

Source: The Author

Figure 20 – Streamlines and vorticity from 21 June 2010 at 0000 UTC to 24 June 2010 at 0000 UTC for: 850hPa (a, b, c, d); 750hPa (e, f, g, h); and mid-levels water vapour content (i, j, k, l).

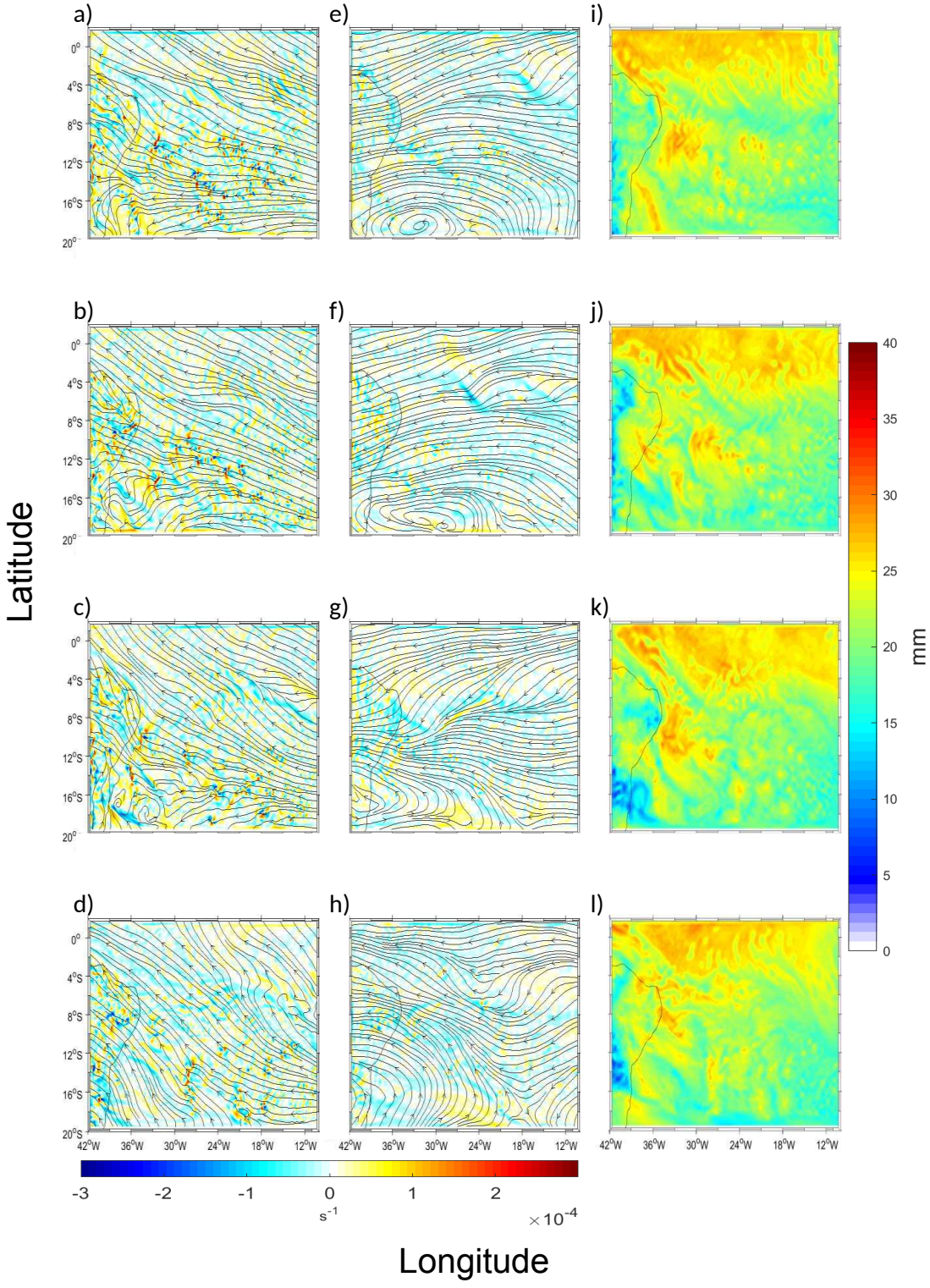

Source: The Author

4.2.4 Zonal water vapour fluxes

The pattern of medium-level moisture is connected with moist convection (BROWN; ZHANG, 1997; HOLLOWAY; NEELIN, 2009), with anomalous wet (dry) periods, showing higher (lower) water vapour variability at medium levels, compared to low levels (BROWN; ZHANG, 1997). Therefore, the zonal water vapour fluxes in the free atmosphere were analyzed between 850 and 500 hPa, to verify the influence and potentiality of the meteorological system in the intense precipitation of the ENEB.

Figure 21 is a latitude x time Hovmöller, at a fixed longitude of 35°W, to verify the Zonal Water Vapor transport (WVT) during the meteorological disturbances in WRF-ROMS 1, WRF-ROMS 2 and WRF-ROMS 3 (Figure 21a) simulations. Also, we verify the difference in WVT in the coupled and uncoupled models (Figure 21b). The negative WVT means that the zonal fluxes are westward, also, the high vapor content in medium levels indicates the presence of meteorological systems in 850 and 750 hPa, during the studied period.

In the simulations with no heat fluxes activated over the ocean (Figure 21a top panel), a westward water vapor transport was observed during the easterly waves propagation, crossing the ENEB. Even if the westward TWV in the WRF-ROMS 1 is weak it also provides moisture to the continent, leading the conclusion that development of the meteorological system between 13 to 18 June is independent of surface latent and heat fluxes.

The experiments with activated fluxes suggest that, they are responsible to increase humidity in medium levels of atmosphere. This occurs mainly when the systems cross the SAWP region. Also, the intense core of water vapor is overlaid with cyclonic vorticity and moisture convergence.

In the 19 to 25 June period, as verified in the synoptic analyzes (Figure 20), the disturbances presented cyclonic vorticity at low levels, as well lower moisture content at mid-levels. In Figure 21a, b (top panel), the experiments without fluxes of both coupled and uncoupled models, were not capable to represent the westward TWV. These results indicate that the development of the systems is related to heat and humidity exchanges between ocean and atmosphere.

In the coupled model, the ocean-atmosphere feedback influenced the magnitude of the WVT in medium levels of the atmosphere (Figure 21b middle and bottom). As well the variability of the SST showing that, the coupling effect of the meteorological and oceanic models optimizes the thermodynamic structure at low and medium levels, similar to that shown in Renault et al. (2012).

4.2.5 Atmospheric vertical structure

In this section we discuss the displacement of the atmospheric systems in a longitudinal profile with WRF-ROMS 2,analyzing the atmospheric water vapor and ocean temperature. The mean period (10 to 25 June) was removed from each water vapor content daily profile to identify

Figure 21 – Hovmöller of water vapor in medium levels, with longitude fixed at 35°W, for the experiments (a - upper panel) WRF-ROMS 1(a - middle panel) WRF-ROMS 2 and (a - bottom panel) WRF-ROMS 3. Difference between WRF-ROMS 1 and WRF 1 (b - upper panel), WRF-ROMS 2 and WRF 2 (b - middle panel), WRF-ROMS 3 and WRF 3 (b - bottom panel).

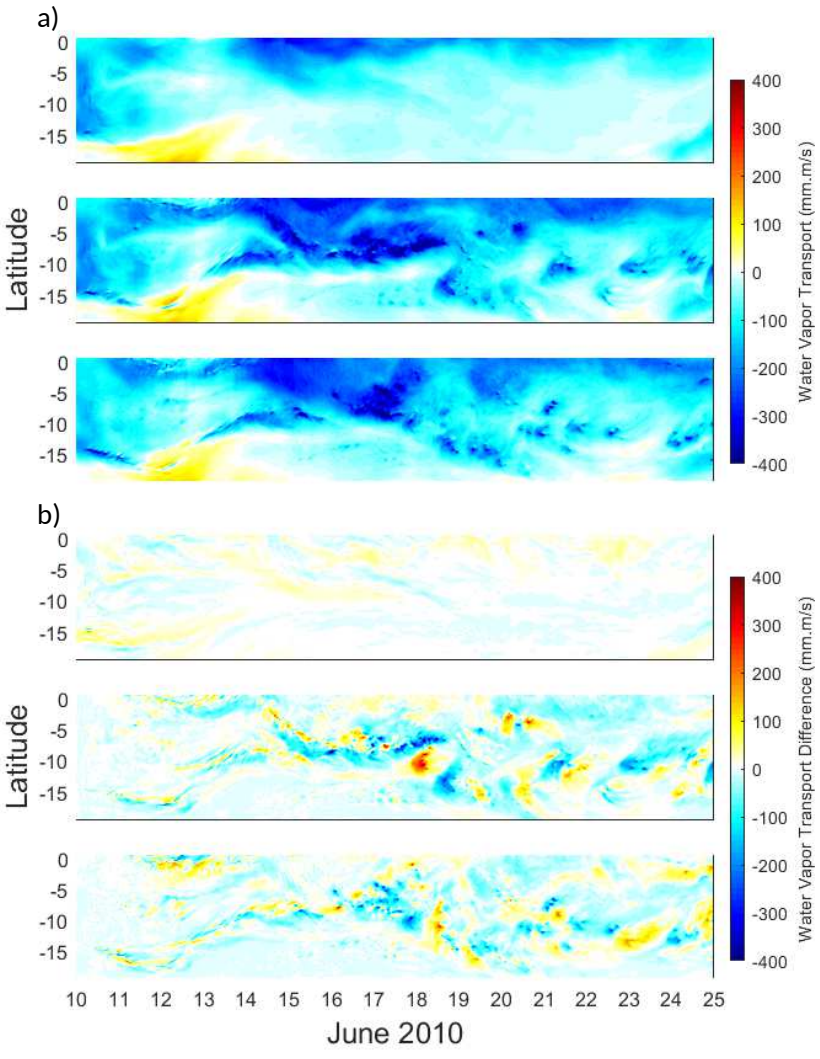

Source: The Author

the systems propagation. Through atmospheric radiosondes (not show) we detected the inversion layer base, which is the isoline of water vapor 0.012 $kg.kg^{-1}$ presented in our analyzes.

In the 12 to 15 June period (Figure 22), an upward flow of water vapor from low to medium levels of the atmosphere occurs. This water vapor increase is coinciding with the low-pressure center, humidity convergence and cyclonic vorticity in medium levels as showed in previous results. A lift of water vapor isoline occurs during the easterly wave propagation.

The core of maximum water vapor content was displaced from 20°W in June 12th to near 33°W in June 15th with about 15.7 $km.h^{-1}$ propagation (3.4 $degree.day^{-1}$). The SST anomaly in the SAWP region intensified the system causing atmospheric instabilities and supporting the presence of convective cloudiness, as identified in previous studies (BROWN; ZHANG, 1997; WANG; ENFIELD, 2001; WANG et al., 2006; KOUADIO et al., 2012; HOUNSOU-GBO et al., 2015).

During the easterly waves proximity to continent in 15 to 16 of June, there are no clouds of high vertical development in the satellite images (not shown). However, in 17 of June, they are above the continent (35°W) and intensifying the upward movements. This occurs mainly because the dynamic effects of the change between the ocean to the terrestrial surface (Figure 22b), which contribute to the development of a mesoscale convective system, that reached the maximum at 1800 UTC.

In the events from 21 to 24 June (Figure 23), the water vapor content in low levels increased, however it was restricted in the layers up to 700 hPa and weaker than before June 21st. Thus, the results are consistent with Ramos (1975), who also found that, the upward moisture fluxes occurs only under influence of a meteorological system.

The eastern TSA basin is associated with the strong inversion of the trade winds. Therefore, when there is an atmospheric disturbance developed over areas with strong SST gradient, as in the central to western TSA, there is a break of stratiform nebulosity and development of cumuliform clouds (CHELTON; XIE, 2010) associated to the increasing of the MABL (CARRILLO et al., 2015). The development of these disturbances in this region are associated to cyclonic vorticity of the winds at low levels of the atmosphere, mainly due to the wind, when crossing from a cold oceanic environment to a warmer region (CHELTON; XIE, 2010).

4.2.6 Rainfall comparison in the simulated period

4.2.6.1 Period 10 to 16 June 2010

The WRF-ROMS 1 and WRF 1 experiments, with no sensible and latent heat exchange (Figure 12a, b) show precipitations in the ENEB, coming from frontal system. The experiments with coupled model WRF-ROMS 2 (Figure 25c) and WRF-ROMS 3 (Figure 25e), simulated higher amount of precipitation than the uncoupled model experiments WRF 2 (Figure 25d) and WRF 3 (Figure 25f). These results suggest that these events are not fully dependent from

Figure 22 – Longitudinal profile of atmospheric water vapor (upper panel), period 10-25 June 2010 average removed, and ocean temperature (bottom panel) from (a) 12 June 2010 at 0000 UTC, (b) 13 June 2010 at 0000 UTC, (c) 14 June 2010 at 0000 UTC and (d) 15 June at 0000 UTC, Isolines of 0.012kg / kg (upper panel, black line) and oceanic temperature (bottom panel, black line) with emphasis on the isotherm of 20 °C and 28.5°C.

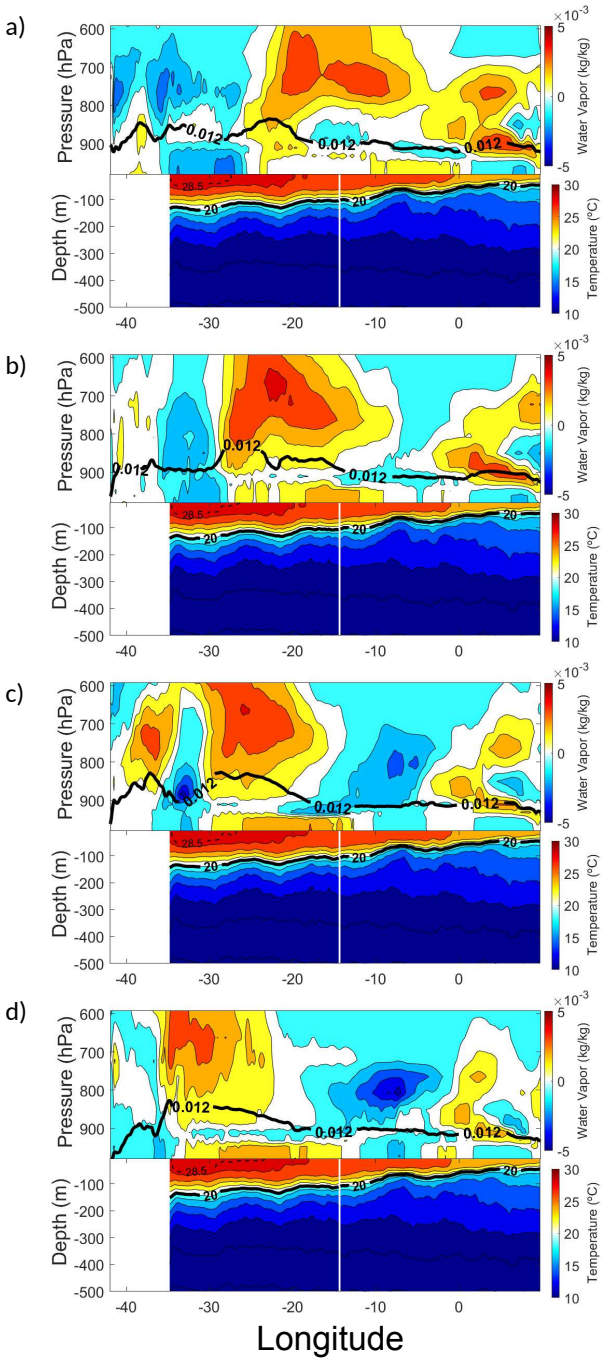

Source: The Author

Figure 23 – Longitudinal profile of atmospheric water vapor (upper panel), period 10-25 June 2010 average removed, and ocean temperature (bottom panel) from (a) 16 June 2010 at 0000 UTC, (b) 17 June 2010 at 0000 UTC, (c) 18 June 2010 at 0000 UTC and (d) 19 June at 0000 UTC, Isolines of 0.012kg / kg (upper panel, black line) and oceanic temperature (bottom panel, black line) with emphasis on the isotherm of 20 °C and 28.5°C.

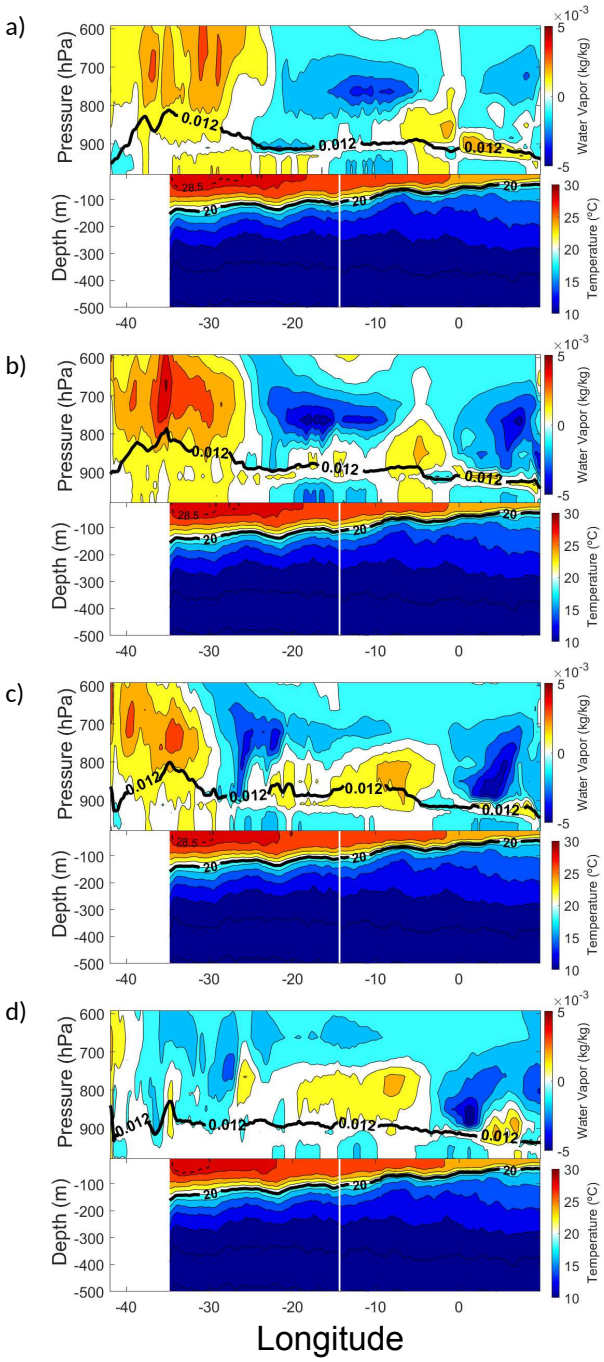

Source: The Author

Figure 24 – Longitudinal profile of atmospheric water vapor (upper panel), period 10-25 June 2010 average removed, and ocean temperature (bottom panel) from (a) 21 June 2010 at 0000 UTC, (b) 22 June 2010 at 0000 UTC, (c) 23 June 2010 at 0000 UTC and (d) 24 June at 0000 UTC, Isolines of 0.012kg / kg (upper panel, black line) and oceanic temperature (bottom panel, black line) with emphasis on the isotherm of 20 °C and 28.5°C.

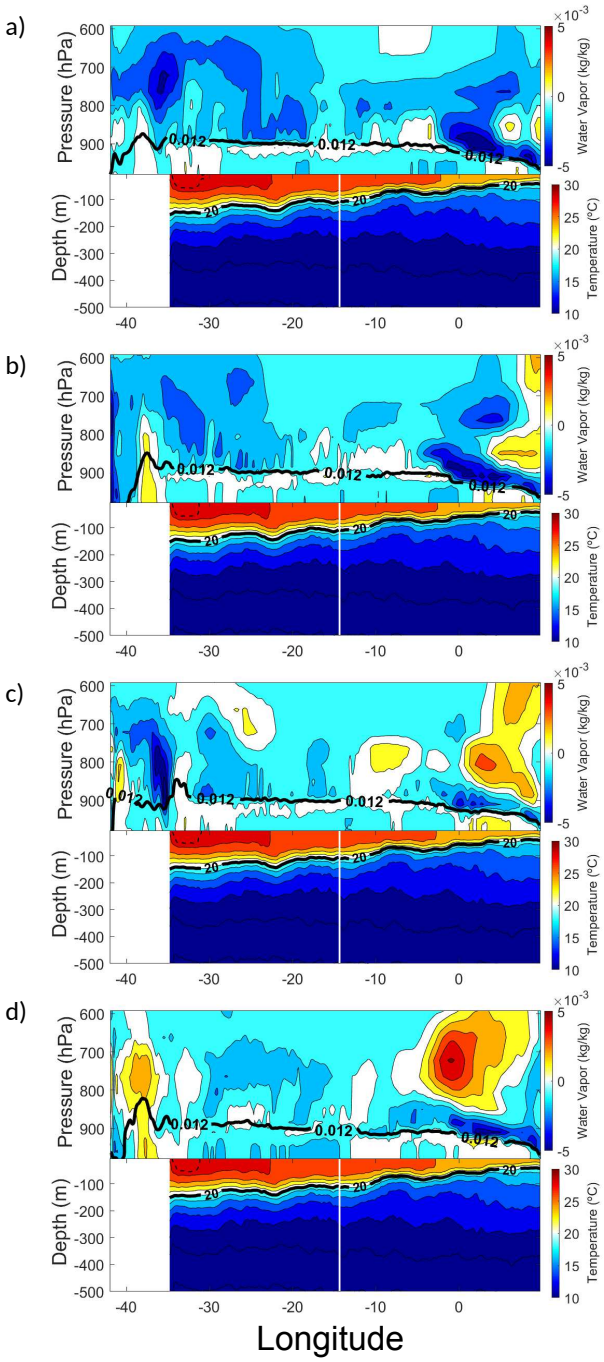

Source: The Author

Figure 25 – Cumulative rainfall in the period from 10 to 16 June 2010 simulated with the experiments: (a) WRF-ROMS 1, (b) WRF 1, (c) WRF-ROMS 2 (d) WRF 2, (e) WRF-ROMS 3 e (f) WRF 3

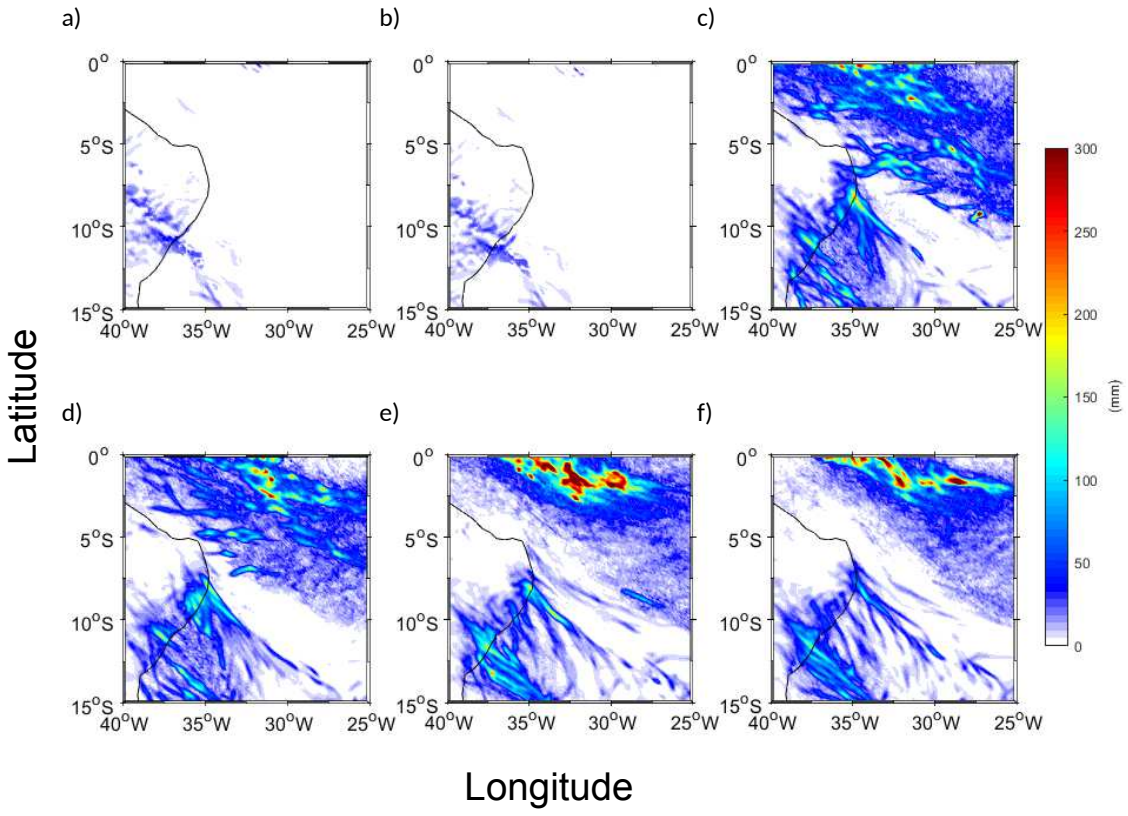

Source: The Author

heat fluxes, but primarily by dynamic processes from the frontal system. The influence of high moisture coming from Atlantic Ocean is the main source of precipitation for this period, once the frontal system simulated in WRF-ROMS 1 and WRF 1 was more southward from the position of the event than with activated fluxes experiments.

4.2.6.2 Period 16 to 19 June 2010

The period from 16th to 19th June (Figure 26) evidence the importance of heat exchange in extreme rainfall simulations. In WRF-ROM-E1 and WRF 1, the rainfall event was not simulated. The results of the WRF-ROMS 2 (Figure 26c) simulated the extreme rainfall event close to the measurements from Pernambuco Meteorological Agency (APAC) than WRF 2 (Figure 26d). With these scenarios, only WRF-ROMS 2 was capable to simulate the extreme rainfall event. In WRF-ROMS 3 (Figure 26e) and WRF 3 (Figure 26f) were not capable to simulate the accumulated precipitation.

Figure 26 – Cumulative rainfall in the period from 16 to 19 June 2010 simulated with the experiments: (a) WRF-ROMS 1, (b) WRF 1, (c) WRF-ROMS 2 (d) WRF 2, (e) WRF-ROMS 3 e (f) WRF 3.WRF-ROMS 3 e (f) WRF 3

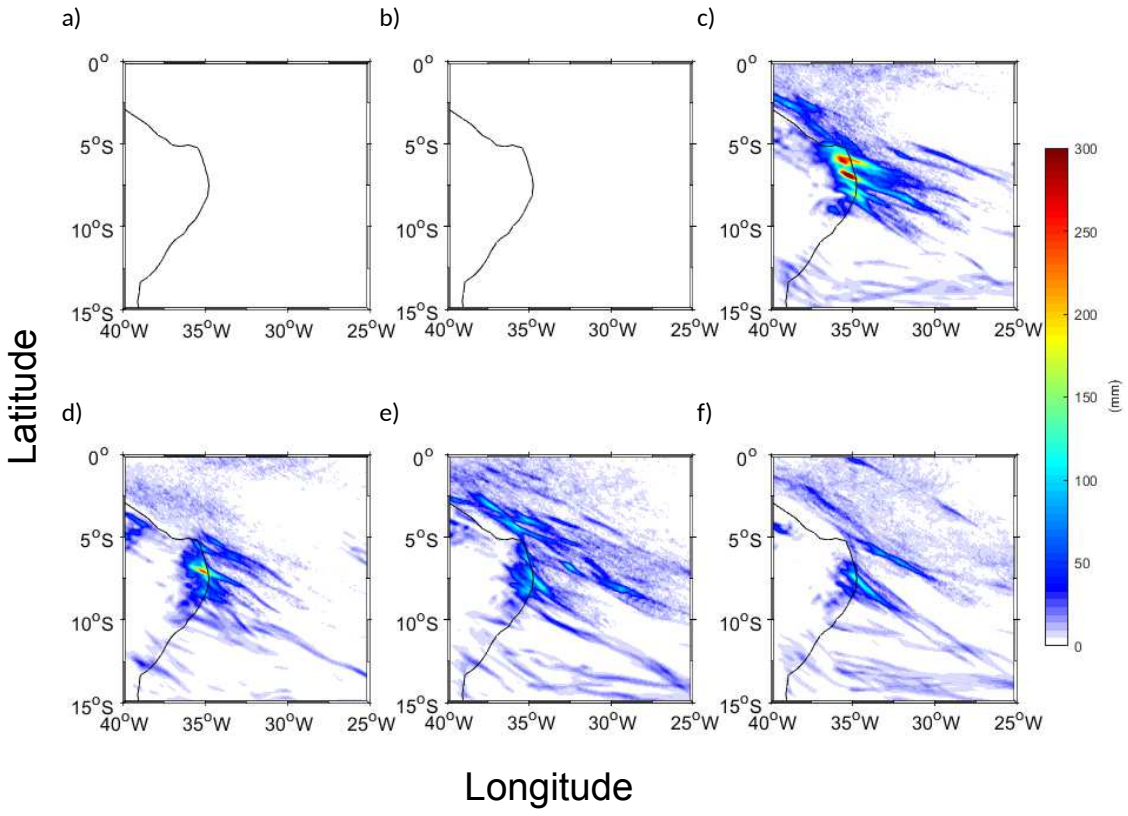

Source: The Author

4.2.6.3 Period 19 to 25 June 2010

Such as previous result, the rainfall period from 19 to 25 June, couldn't be simulated in WRF-ROMS 1 and WRF 1 (Figure 27a,b). Also, the WRF-ROMS 2 simulated higher accumulated precipitation than WRF 2 (Figure 27c,d) as in the previous results. Comparing WRF-ROMS 2 with WRF-ROMS 3 there is a difference in total rainfall, where the WRF-ROMS 2 are closest to the measurements.

4.3 DIFFERENT SST INPUT

To evaluate the changes in the simulated scenario due to SST, we performed changes in boundary conditions for SST. At first moment was simulated the period from 10 to 25 June 2010 with real conditions. In second moment, the SST was modified to conditions measured in 10 to 25 of June 2012. This change are made to verify the simulated patterns influenced by warm and cold SST.

The period between 10 to 25 June 2010 was influenced by SST positive anomalies in

Figure 27 – Cumulative rainfall in the period from 20 to 25 June simulated with the experiments: (a) WRF-ROMS 1, (b) WRF 1, (c) WRF-ROMS 2 (d) WRF 2, (e) WRF-ROMS 3 e (f) WRF 3

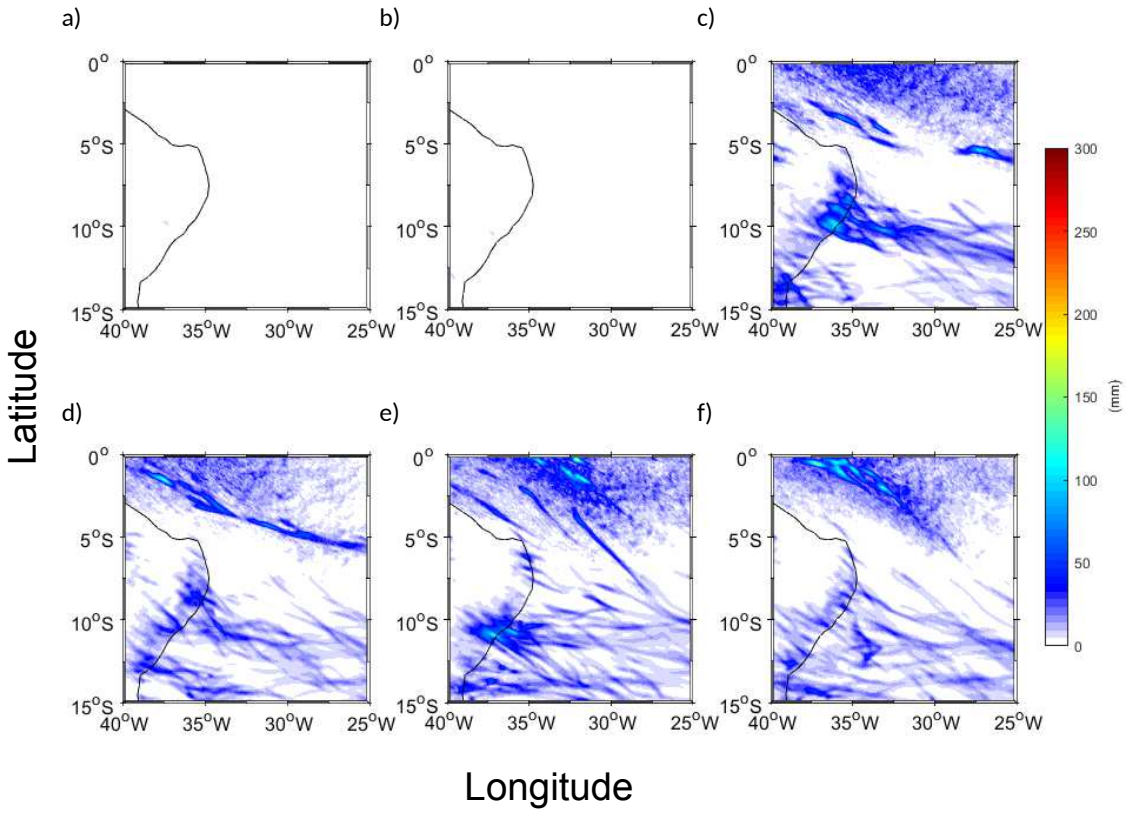

Source: The Author

TSA, measured by PIRATA (SERVAIN et al., 1998) buoys, where values reached more than 1°C degrees in SAWP Region. In this period flash floods occurred in ENEB Region, also accompanied by landslides, homeless and deaths due to the rainfall episode.

In other hand, the 2012 year was the one of most dryer year recorded in entire NEB. The reports by the Pernambuco official weather service, show that the regions where the two years later had floods, in this year was 40 per cent below the climatology (APAC, personal communication). Also it was marked by the beginning of five years 2012 - 2017 of droughts (MARENGO et al., 2017). The AVRHH composite from 10 to 25 June showed SST below climatology by about 0.5°C degrees.

4.3.1 Synoptic Comparison

Figure 28 shows the averaged sea surface temperature from 10 to 25 June in WRF-ROMS coupled simulations of the 2010 a) and 2012 SST conditions b). The results shows that the area of SAWP was warmer in 2010 than in 2012. Also, analyzing the SST in both cases it is evident that, in 2012 the 28.5°C isotherm is not present, showing an absence of the SAWP region by

Figure 28 – Averaged SST for 10 to 25 June with a) 2010 SST and b) 2012 SST boundary conditions. Black contours is the 28.5°C isotherm.

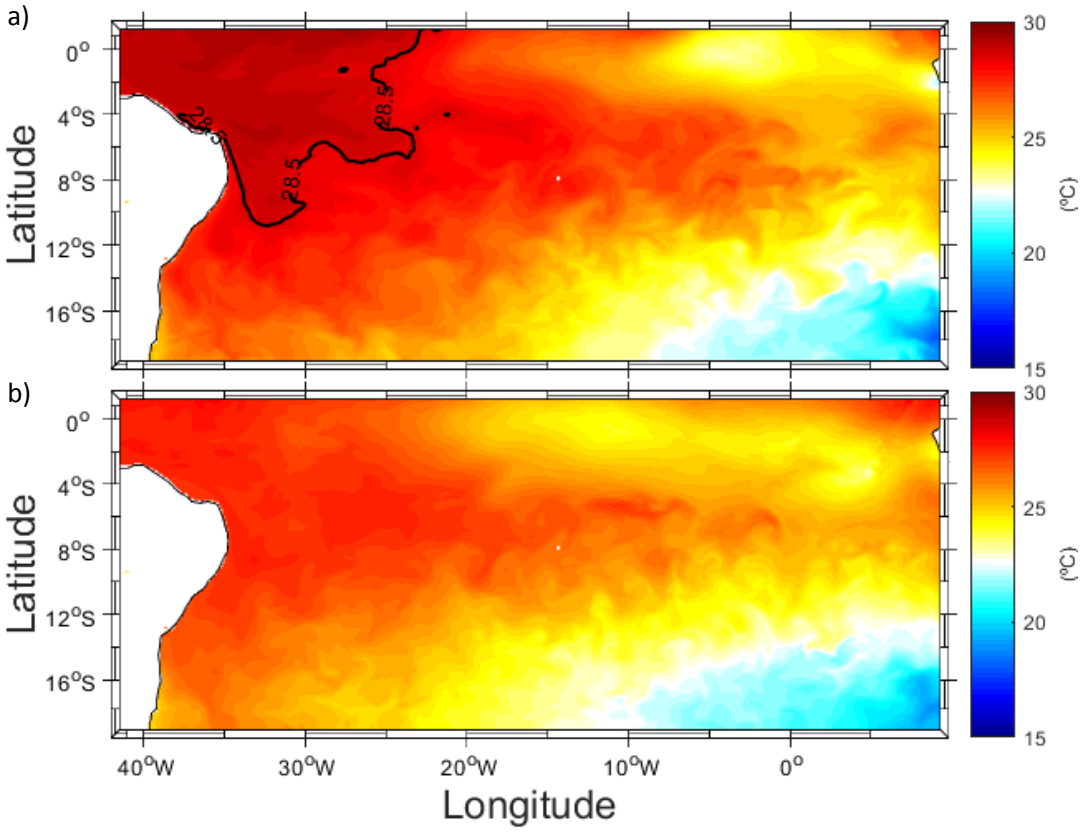

Source: The Author

Wang and Enfield et al. (2004) criteria.

The two-way coupled simulation permitted the free simulation of SST from ROMS, acquiring the WRF boundary conditions and controlled by WRF simulated MABL dynamics in an near real time-step condition. By changing the initial condition of SST with above situation, the atmosphere synoptic conditions won't change, except if, the variability was caused by SST initial condition modification.

The mean daily streamlines in 700 hPa (Figure 29) shows the synoptic system which caused the intense rainfall episodes in 17 and 18 June 2010. The first column shows the simulated with 2010 (normal) conditions. The sequence shows the average from 16, 17 and 18 of 2010, meanwhile the second column represent the same period, but for 2012 SST conditions.

The results shows that, the trough displaces from day 16 in central TSA and reach near coast in day 18 in both simulations. However it's observed in 2010 SST conditions, higher wind speed as a jet in day 17, more smoothed trough in day 18, an absence of intense wind speed also is observed in 2012 SST conditions in day 18. These dynamical configurations shows the dynamic of simulated system had changed with the SST initial conditions, but the atmosphere synoptic is represented in both simulations.

Figure 29 – Streamlines and wind speed in 850 hPa from day 16, 17 and 18 June 2010 in WRF-ROMS using 2010 SST a, b, c and 2012 SST boundary condition d, e, f.

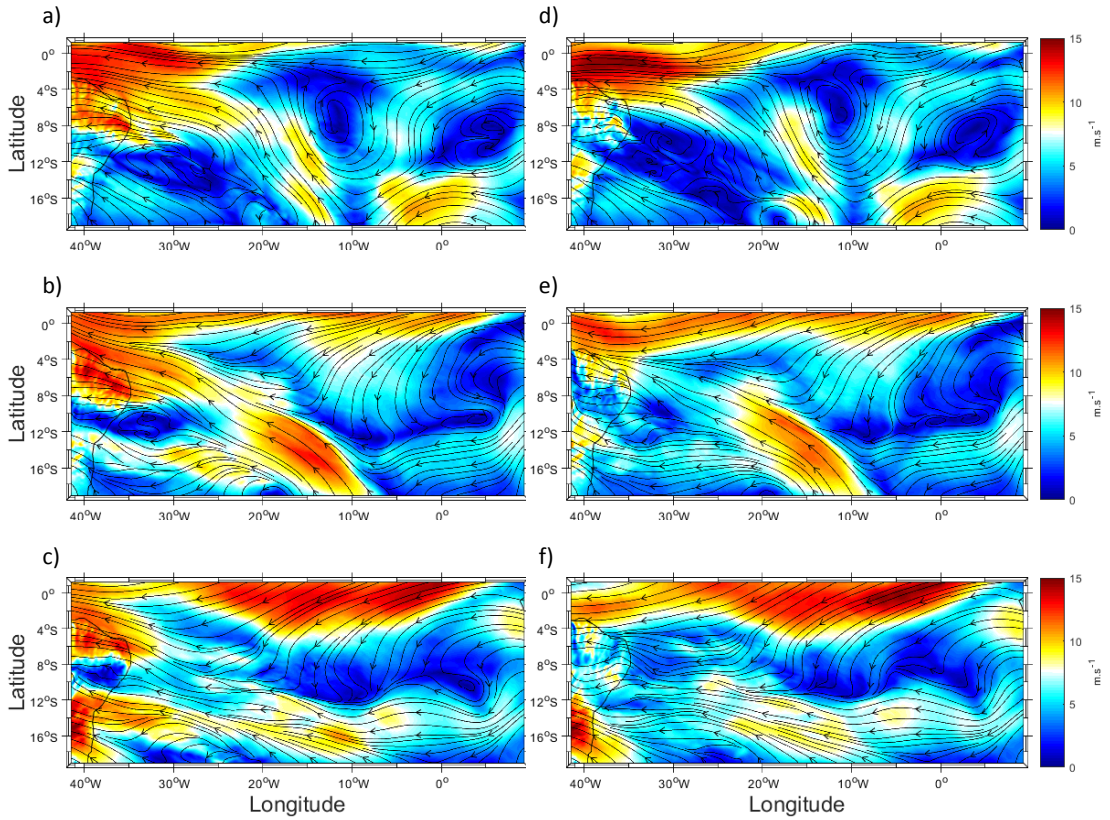

Source: The Author

4.3.2 MABL conditions

We performed the averaged SAWP area (between 34°W - 25°W; 12.5°S - 4°S), for SST and 2m air temperature (T2m) Figure 30. The positive values of gradient indicate that SST is warmer than T2m, meaning the positive values the SST loses heat for atmosphere. In simulations with 2010 SST there was a intense gradient between day 12 and day 14, and a decreasing after day 14. In opposite, the gradient in 2012 SST was more intense than 2010 SST.

The results shows that the 2012 SST simulations the gradient was more intense, but there was a quickly decreasing in simulated T2m in first time-steps and persisting for the entire period.

The profile of virtual temperature (Figure 31) was plotted to identify thermal instabilities in the MABL. The results show more heated MABL in 2010 than 2012 SST input. In dotted lines there is a day 17 vertical profile of MABL. In either SST conditions there is a warmer low atmosphere and more heated MABL.

The 2012 SST showed more shallow MABL in average, where the profiles comes warmer with height (about 1000m). However in day 17 June there is a smoothed warming with height,

Figure 30 – Time series of SST-T2m averaged in SAWP area during 10 to 25 June 2010. Light grey is period simulated with 2012 boundary conditions; Dark grey is period simulated with 2010 boundary conditions.

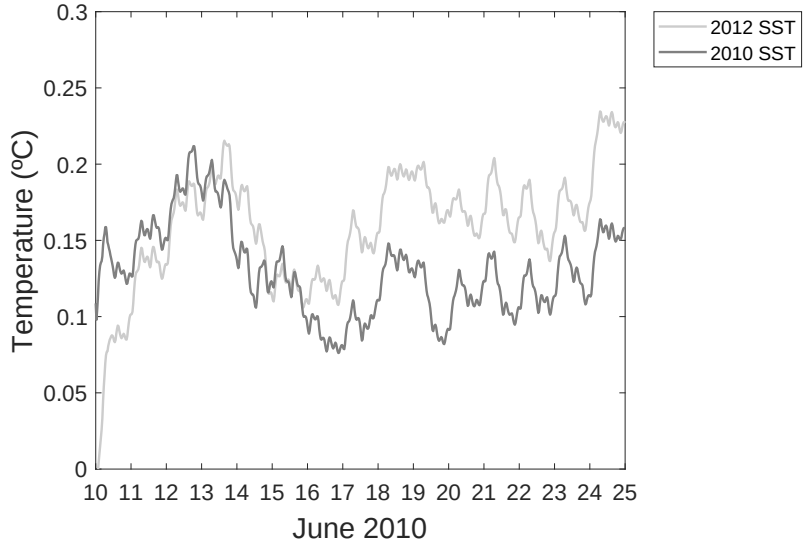

Source: The Author

Figure 31 – Vertical profile of the Virtual Temperature. Dotted lines are day 17 June, light grey is 2012 boundary conditions; dark grey is 2010 boundary conditions; solid line is the averaged period of 10 to 25 June 2010; light grey is 2012 boundary conditions; dark grey is 2010 boundary conditions.

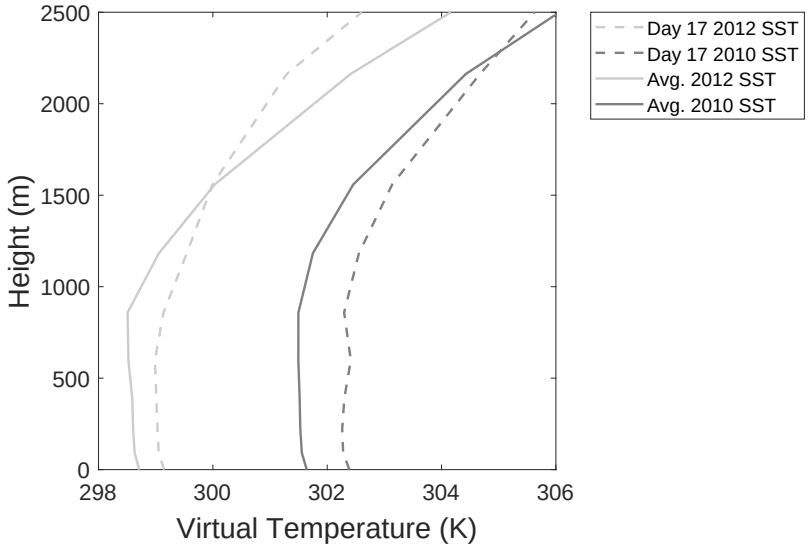

Source: The Author

which meaning more instability than mean condition for this simulation. In other hand, the more warmer conditions show a smoothed warming of vertical profile, which mean an higher MABL (PENG et al., 2016). Also, with the more heated MABL for day 17 June this cause more convective instabilities (WANG; ENFIELD, 2001).

The instabilities result in upward motion as shown in Figure 32. The results indicate that

Figure 32 – Vertical profile of the Vertical motion. Dotted lines are day 17 June, light grey is 2012 boundary conditions; dark grey is 2010 boundary conditions; solid line is the averaged period of 10 to 25 June 2010; light grey is 2012 boundary conditions; dark grey is 2010 boundary conditions.

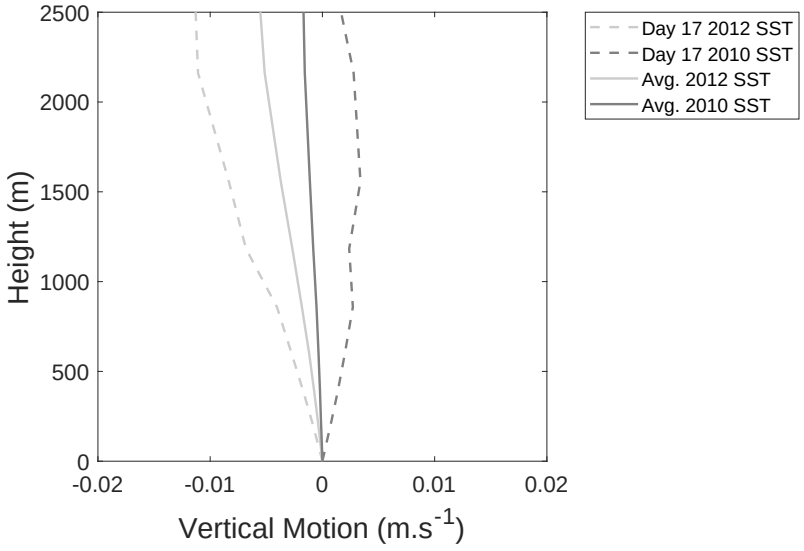

Source: The Author

are upward motions only in day 17 June in 2010 SST, meanwhile the movements are descendant in 2012 SST and null in average for 2010 SST. Due to influence of trade winds inversions over the ENEB and TSA Region (SCHUBERT et al., 1995) these simulated MABL structure was important to verify the aspect of vertical movement contrast in cold and warm SST input.

The lower troposphere over the tropical oceans can be efficiently mixed in vertical due to buoyant convection forced by surface evaporation, but the mixing are limited in the vertical by these trade wind inversions (LINDZEN; NIGAM, 1987). The trade wind inversion height are controlled by horizontally averaged values of sea surface temperature, divergence, and above-inversion atmospheric structure (SCHUBERT et al., 1995).

The results shows that for 2012 SST there was an environment favouring to descendent movements, meanwhile for 2010 SST conditions there is a upward movements which act as source of moisture to middle and upper atmosphere. Thus, the results shows that the cold (warm) waters acted to stabilise (destabilise) the atmosphere in the MABL.

For Latent Heat flux (Figure 33) there was a great difference between the simulations. The more warmer waters generated more LH fluxes causing more losses of water vapour to the atmosphere and cooling of surface ocean waters. The exchange of moisture and heat for atmosphere is the local term for destabilise, increasing the height and moistening the MABL (LINDZEN; NIGAM, 1987).

The results are consistent with different analyses for cold waters. In upwelling and oceanic cold fronts areas, the low values of temperature are responsible for decreasing latent

Figure 33 – Time series of Latent Heat averaged in SAWP area during 10 to 25 June 2010. Light grey is period simulated with 2012 boundary conditions; Dark grey is period simulated with 2010 boundary conditions.

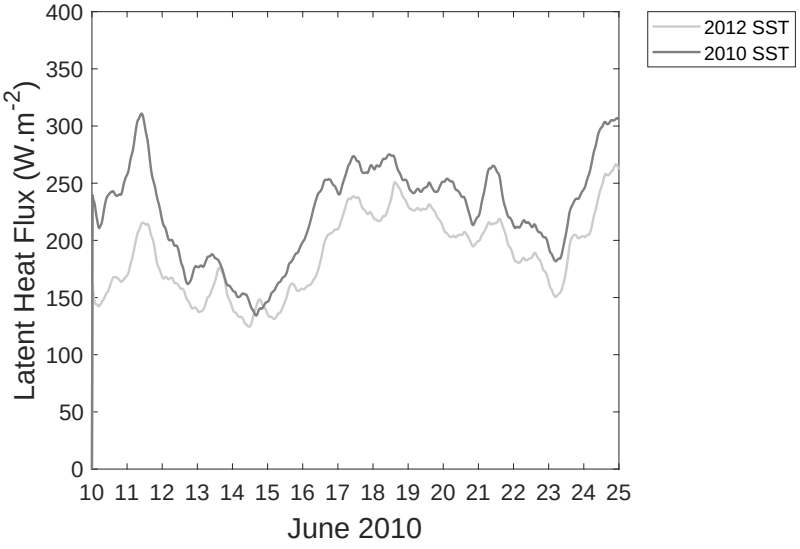

Source: The Author

heat and have less water vapour in these regions. However, it's important remember that the relative humidity is inversely proportional to air temperature, so in locals there is cold tongue and cold fronts there is a presence of stratiform cloudiness, associated to low and well mixed MABL (CARRILLO et al., 2015).

The less intense LH flux generates a dryer troposphere (Figure 34) in 2012 SST. The instabilities associated with more LH flux and warmer atmosphere simulate moisten MABL in 2010 SST. Also, the results show, at day 17, a moister atmosphere than period average and the more discrepant values presented in height above 1500m. The moisture above the boundary layer is the key to deep convection and high average precipitation rate (BROWN; ZHANG, 1997; HOLLOWAY; NEELIN, 2009).

Therefore the results shows that the influence of SST is a key factor supply the low- and mid- levels of atmosphere, resulting in warmer and moisten MABL and atmosphere above. As in North Atlantic Warm Pool (NAWP) where Caribbean Low Levels Jet carries the moisture from that region to land surrounded by, the SAWP can also act in the same way. The water vapour content and transport is the closest link to the rainfall variability over entire NEB. The precipitation is consequence of the transport of water vapour from ocean to the land (CAVALCANTI; GANDU; AZEVEDO, 2002).

The surface winds (Figure 35) increases over warm waters in association with decreased instabilities through enhanced vertical mixing by large eddies that deepens the MABL, in opposite, the wind speed decreases over cold waters in association with opposite effects (CHELTON; XIE, 2010). The results show these dynamics compared with in both simulations, where wind speed in 2010 SST was more intense than 2012 SST. Additionally, the vertical movements

Figure 34 – Vertical profile of the Water Vapour. Dotted lines are day 17 June, light grey is 2012 boundary conditions; dark grey is 2010 boundary conditions; solid line is the averaged period of 10 to 25 June 2010; light grey is 2012 boundary conditions; dark grey is 2010 boundary conditions.

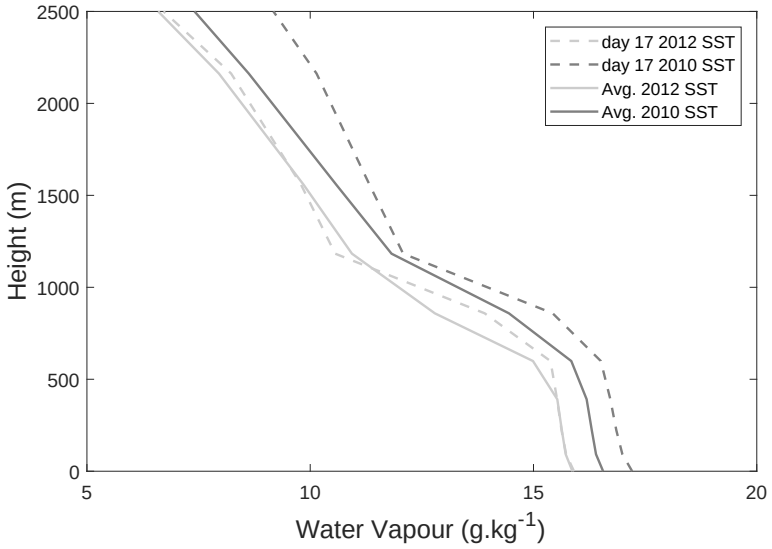

Source: The Author

obtained in 2012 SST suggest that downward motion can decelerate the horizontal flow. Also, the warmer SST in this regions acted to increase the SST gradient which acted to accelerate the horizontal flow.

It's important to mention the intensification of wind speed between day 13 to early day 17 June. In North Hemisphere the North Atlantic Subtropical High pressure (NASH) carries moisture to Caribbean Sea, where the winds are intensified to form maximum of easterlies trade winds, called Caribbean Low-Level Jet (WANG; LEE, 2007). In similar way, the previous results showed (Figure 29) that in the 2010, occurred stronger wind speed and more water vapour transport from ocean to the land.

The vertical profile of wind speed (Figure 36) shows the same magnitude in average until 1200m height. It means that the mean flow didn't change. However above this layer there was an intensification in the averaged wind speed of 2010 SST. For day 17, it is an intensification of the values reaching 12 m.s^{-}1 of magnitude, similar to the Caribbean Low Levels Jet (WANG; LEE, 2007). The difference is about 2 m.s^{-}1 in low levels and increase to about 4 m.s^{-}1 in 2500 m height.

The results complements the previously discussed, where the entire column transport higher quantity of water vapour to the land. It's important refer to the 1500 - 2500 m layer, with intense wind speed and more water vapour available in 2010 SST. The mid-level moisture transport can be associated to the deep convection in ENEB for this period. This dynamic in mid-level is attributed to lifting or even breaking of trade wind inversions, that cause the upward

Figure 35 – Time series of Wind Speed averaged in SAWP area during 10 to 25 June 2010. Light grey is period simulated with 2012 boundary conditions; Dark grey is period simulated with 2010 boundary conditions.

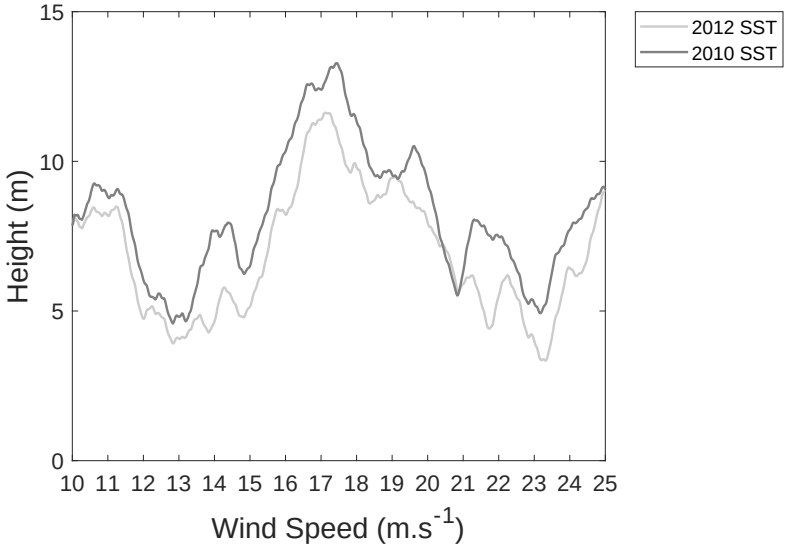

Source: The Author

Figure 36 – Vertical profile of the Wind Speed. Dotted lines are day 17 June, light grey is 2012 boundary conditions; dark grey is 2010 boundary conditions; solid line is the averaged period of 10 to 25 June 2010; light grey is 2012 boundary conditions; dark grey is 2010 boundary conditions.

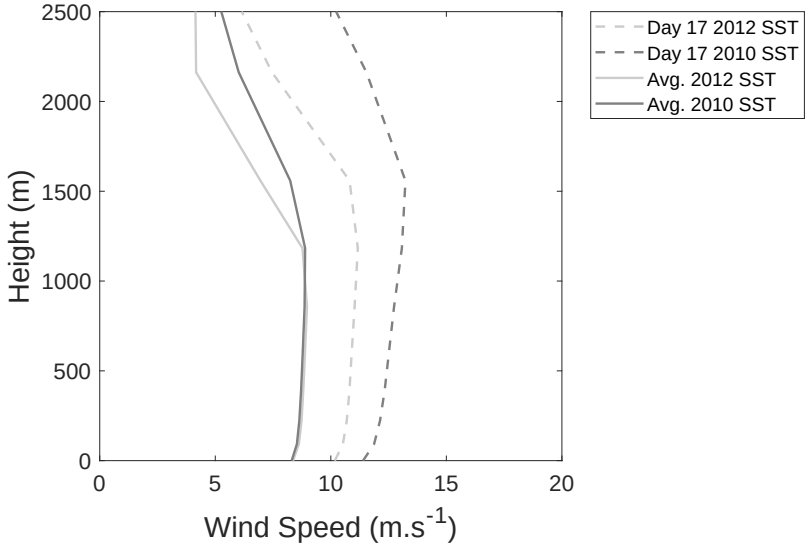

Source: The Author

motion of moisture from the PBL to free atmosphere above.

4.3.3 Rainfall Conditions

The rainfall Hovmöller is showed in Figure 37 for 2010 a) and for 2012 b) SST. The results shows the Extreme event in days 17 and 18, simulated with the 2010 SST, but didn't

Figure 37 – Daily rainfall Hovmöller (longitude 35°S and averaged latitude between 5°S to 10°S) for period simulated by: a) 2010 and b) 2012 SST boundary conditions.

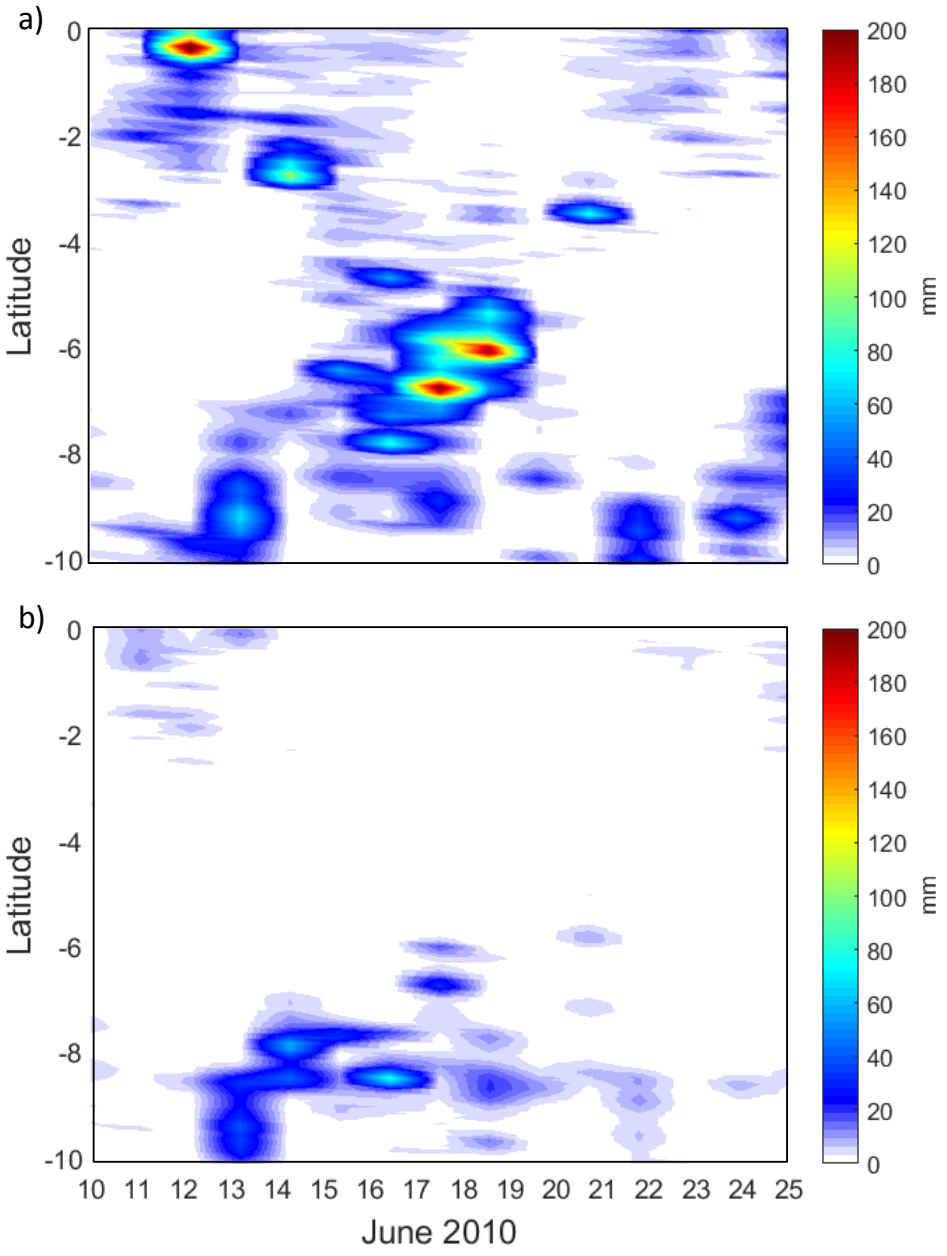

Source: The Author

simulate with the 2012 SST. According with previous results, the SAWP region as the MABL characteristics was the important key to simulate intense rainfalls in ENEB. In previous work (DRUYAN; FULAKEZA, 2011), they presented the influence of the Tropical Atlantic in rainfall climatology and showed decreasing in West African summer monsoon. They found that the cold SST influence negatively the African Easterlies Waves, consequently the rainfall regimes.

Also, Housou-gbo et al. (2015) showed the influence of SAWP in rainfall climatology

over Recife (ENEB) and found a direct correlation between the warmer SST in positive anomalies of rainfall over ENEB. The SAWP region acted similar to the NAWP (North Atlantic Warm Pool), showed in Wang and Lee (2007), acting as a moisture source to the land, carried by respectively low levels intense wind speed.

It's relevant highlight the influence of the trade winds inversion over the studied region. The trade wind inversions act as a barrier to the upward motions, preventing to moistening of the atmosphere mid-levels, and it is closely linked with triggering of deep convection (CARRILLO et al., 2015). Thus, there is a need for TWIL to be weaken or break, so, that trapped air in the well mixed MABL is transported to atmospheric medium level (RAMOS, 1975). The Easterlies Waves Disturbance (EWD) was capable to conduct this dynamics necessary for precipitation in the ENEB.

The experiment was carefully mounted to have only the SST influencing the simulations. So, the synoptic events which caused the extreme rainfall are present in either experiments. Therefore the rainfall conditions show that the extreme rainfalls corresponded directly with warmer SST in SAWP region, which can conclude the interaction ocean-atmosphere over SAWP region was the main factor to cause extreme rainfall in June 2010 over the ENEB.

The use of WRF-ROMS in two-way coupling allowed simulations between different SSTs to be performed so that both models corresponded in an interactive way. Thus the results also represent a tool for forecasting intense precipitations. The improvements of surface fluxes can lead to a better rainfall simulations being to a powerful tool to mitigate adversities.

4.4 MEAN CONDITIONS

4.4.1 Averaged Pattern

In period between 2009 to 2017 the ENEB suffers with different climate situations. In 2010 and 2011 the ENEB registered two floods, meanwhile since 2012 to 2016 low precipitations amount caused disruptions in the water supply. As shown in others works (MOURA et al., 2009; KOUADIO et al., 2012; HOUNSOU-GBO et al., 2015), the SST was connected with those events. In 2009 to 2011 high conditions of SST was recorded, meanwhile 2012 to 2016 low or near climatology conditions was presented.

To emphasize the results obtained in the previous topics, averages were made for events of EWD under those conditions of SST anomalies. Mean values for positive, negative and near normal anomalies were performed and compared with the methodologies of the previous topics. Figure 38 shows the mean conditions of EWD under different SST conditions.

As observed in Figure 38, the SAWP arises only under the positively anomalous conditions of SST. Years with normal and low conditions, whilst with values above 26 degrees, both the temperature and the area of coverage of the heated waters were weaker and smaller than high conditions of SST. It suggest that SAWP appears only under high SST anomalies. But

Figure 38 – Mean condition for SST in a) High SST conditions, b) Low SST conditions, c) near Normal and d) Entire period averaged.

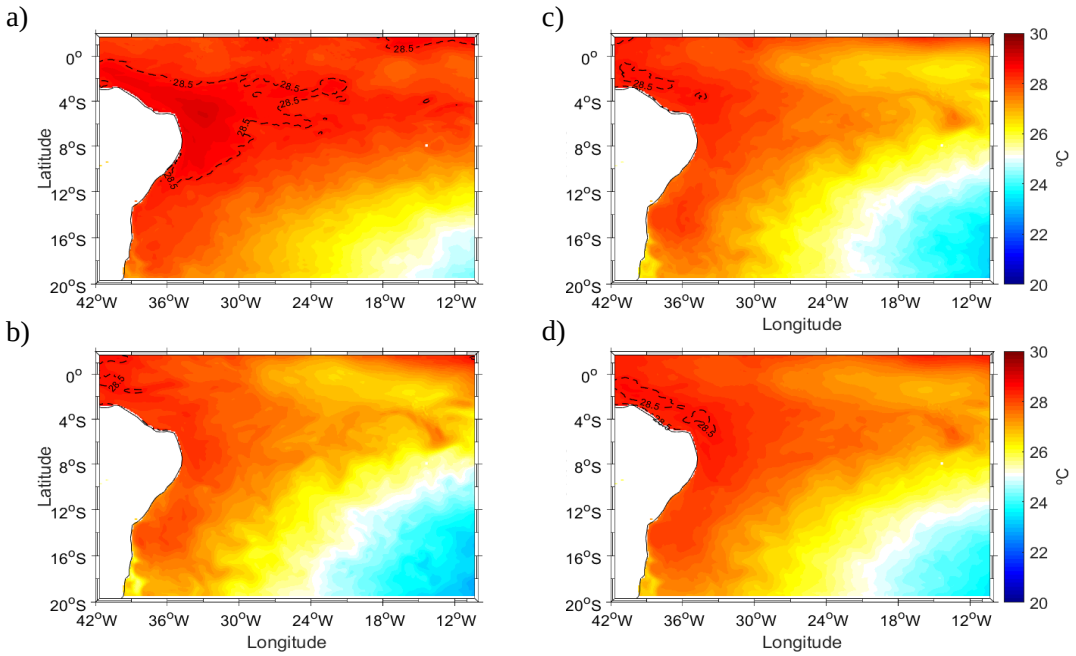

Source: The Author

climatological analysis must been done to verify this issues.

The precipitable water is presented in Figure 39 in different SST conditions. Following the previous results, its shows coherence with high and low SST conditions for 2010 in previous results. Under high conditions, the higher precipitable water was presented, in other hand, lower precipitable water in lower SST conditions. The results are in agreement with Foltz and McPhaden (2006) and Cintra et al. (2015), which shows the latent heat and warmer waters dynamics in direct relationship. Also, its corroborates with works (MOURA et al., 2009; KOUADIO et al., 2012; HOUNSOU-GBO et al., 2015) of correlations between the TSA SST and rainfall regimes over the ENEB.

The pattern in Figure 39a shows relationship with high SST and ITCZ region. It means that the high SST favors the ITCZ southward. So it means, following Schubert et al. (1995), weakening of TWIL of regions surrounding the ITCZ or equatorial trough region. It's possible to suggest that these systems associated to equatorial through can be more bouyant and moisten then southward displacement.

Even the low SST conditions, in ENEB presented good precipitable waters available. It means that the EWD can cause precipitations in ENEB even in adverse conditions. This fact is linked to threshold temperatures of 26 °C which is a convection trigger factor (SABIN; BABU; JOSEPH, 2013). But it not appear to be true for semiarid NEB region (SILVA; GUEDES, 2012). The precipitations in 15 June 2012 was about 100 mm in Eastern Pernambuco recorded by APAC,

Figure 39 – Atmospheric integrated water vapour in a) High SST conditions, b) Low SST conditions, c) near Normal and d) Entire period averaged.

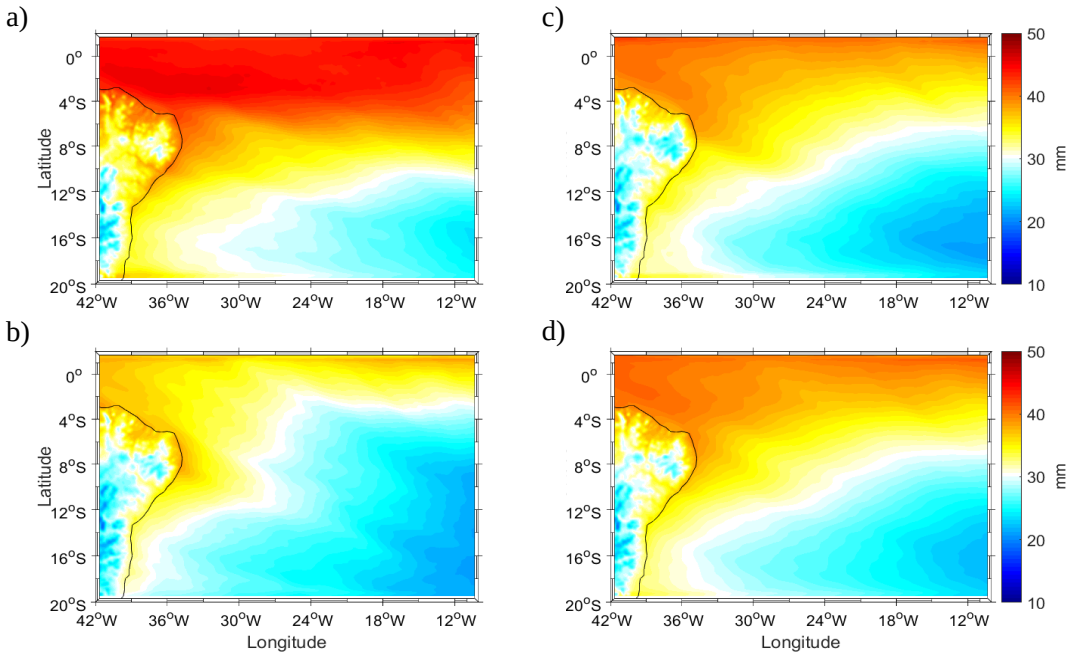

Source: The Author

showing that the intense events of precipitation can occur under low SST conditions also.

The averaged low level structure of atmospheric water vapor over SAWP also was ascertained. The Figure 40 show the patterns with different conditions for SST, showing similarity with previous experiments (4.3 section). The moisten case was in warmer SST conditions meanwhile the drier for lower SST anomalies.

Although the atmosphere is drier with colder SST conditions, intense weather events could occur. This result confirms the previous statement (RAMOS, 1975) showing relationship with the atmospheric phenomena acting to break the TWIL and forming precipitations. Whilst is valid to state that on less unstable conditions, the precipitations should be by warm clouds (LIU; ZIPSER, 2009).

Although it is possible to occur intense events, even with lower temperature conditions, the appearance of intense and extreme events are more likely in high SST conditions. Figure 41 shows the vertical structure of the virtual temperature for the different SST conditions. The result shows that in years with SST above average the atmosphere becomes warmer and humid. These conditions reflect the same pattern as in previous results for the year 2010.

In short, the hotter and moister atmosphere will favor upward motions. In addition, a higher MABL and the availability of water vapor at medium levels. In previous analyzes, these conditions favor deep convection due to warmer SST are associated with warmer and moister troposphere, reducing Sea Level Pressure (SLP), weaker easterlie winds, less vertical wind shear,

Figure 40 – Water vapour profile in SAWP area. Dotted light grey mean condition; Dotted dark grey near normal condition; Solid ligh grey is low SST conditions; Solid dark grey is the high SST conditions.

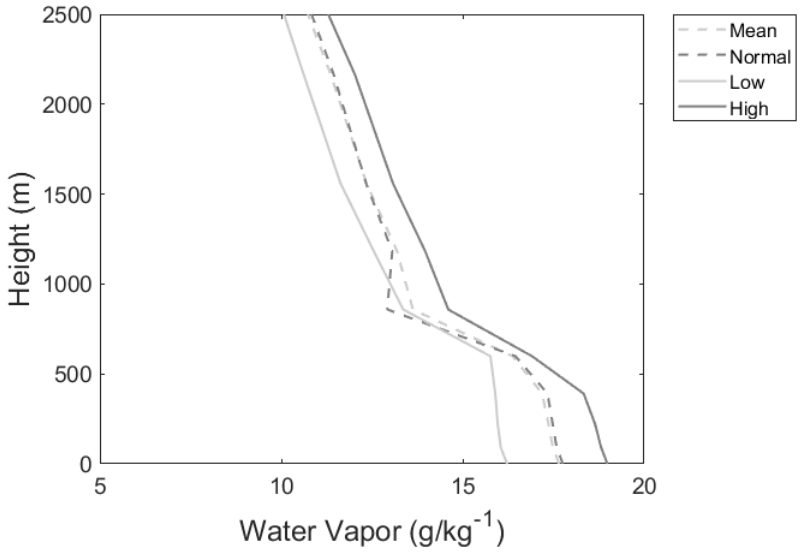

Source: The Author

and weakened subsidence aloft (WANG; ENFIELD, 2001). This concludes that SAWP when present increases the probability of extreme events under the ENEB region.

4.4.2 Synoptic Patterns

To ascertain the dynamics in the atmosphere ocean interface, some synoptic analyzes were made based on the results obtained. Figure 42a, b, c comprises the period from February 20 to 22, 2009 respectively, as well as Figure 42d, and, f from June 30 to July 2, 2009. It is worth noting that both meteorological systems were EWD.

For the year 2009, there is an important relation between the period of occurrence of meteorological systems. In fact, in the period of February, with the ITCZ more to the south, there was a greater presence of water vapour in the atmosphere. While in June the steam becomes less. The main characteristic observed in the two events is the increase of the isoline of 0.012 g.kg^{-}1 in surface waters lower than 28.5 °C. However, in the June event, the isoline is restricted to low levels even with SAWP acting. Another important factor to be analyzed is the increase of water vapour to medium and high levels in the June event, showing that the meteorological system, although weak, showed upward vertical movements and provided humidity for high levels.

Figure 43 shows the events for the year 2011. Both in April, the first event Figure 43a, b, c days 14,15 and 16 April and the second event days 30 April, 01 and 02 May. The year 2011 was marked by a very active SST, with a well-formed SAWP with a relatively large area. It can be observed that the first event the atmosphere presented a very humid and relative to the year of 2009. During the passage of EWD on the SAWP, there is an increase of the isoline of 0.012

Figure 41 – Virtual temperature profile in SAWP area. Dotted light grey mean condition; Dotted dark grey near normal condition; Solid ligh grey is low SST conditions; Solid dark grey is the high SST conditions.

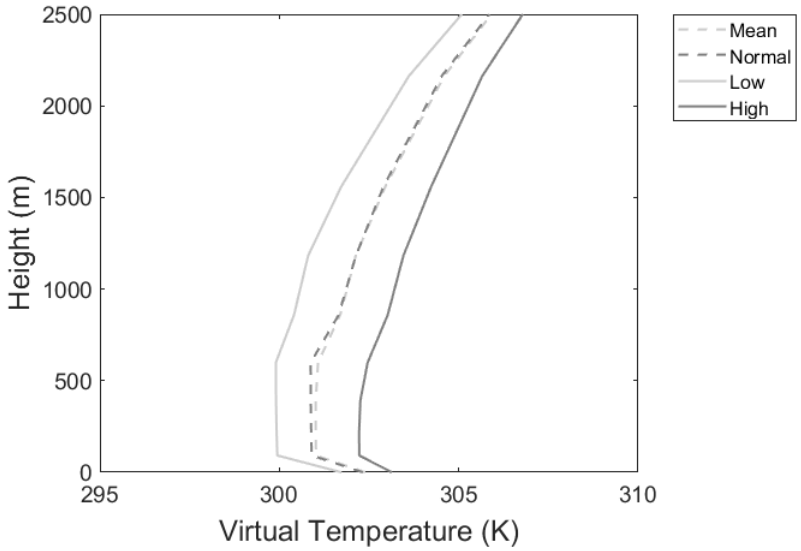

Source: The Author

g.kg^{-}1 but does not rise above the level of 800 hPa . In contrast, the event at the end of April was more intense as well as a greater increase of the isoline of 0.012 g.kg^{-}1. It is worth noting that both systems appeared to be embedded in the equatorial ditch, so the presence of high water vapour content may be related to the origin of the meteorological system, as seen in previous results (2010 analysis) and 2009.

Figure 44 shows the days of the meteorological events of several years, in which: Figure 44a (2012), Figure 44b (2013), Figure 44c (2014), Figure 44d (2015 March), Figure 44e (2015 June) and Figure 44f (2016). The results show that even if there are negative anomalies or neutrality of SST there may be availability of water vapour at medium levels and intense events. Although, when observed in area, there was a smaller area of water vapour availability in events with lower SST. In addition, the difference between the availability of steam between the periods of March 2015 and June 2015 is observed. It is verified that the availability of water vapour is higher in March than in June, a result similar to that found for the It was also observed that the isolate of 0.012 g.kg-1 did not have an expressive increase in the cases in which the SST were low, nevertheless, there is a slight increase in the height of this one, mainly when there are larger values in the availability of steam at medium levels.

The results obtained for the average conditions show that the interaction of the atmosphere in the EWD events is directly related to the meteorological systems. The presence of TWIL inhibiting free convection from low levels to high levels restricts the interaction in MABL. Then, in episodes of SAWP the MABL appears higher which tends to form hot clouds (LIU; ZIPSER, 2009) where the top of the clouds occur at the base of TWIL. In situations where SAWP does

Figure 42 – Longitudinal profile of atmospheric water vapor (upper panel), 10-days period average removed, and ocean temperature (bottom panel) from 20 (a), 21 (b), 22 (c) February 2009 and 30 (d) June, 01 (e), 02 (f) July 2009 at 00UTC. Isolines of 0.012kg / kg (upper panel, black line) and oceanic temperature (bottom panel, black line) with emphasis on the isotherm of 20 °C and 28.5°C.

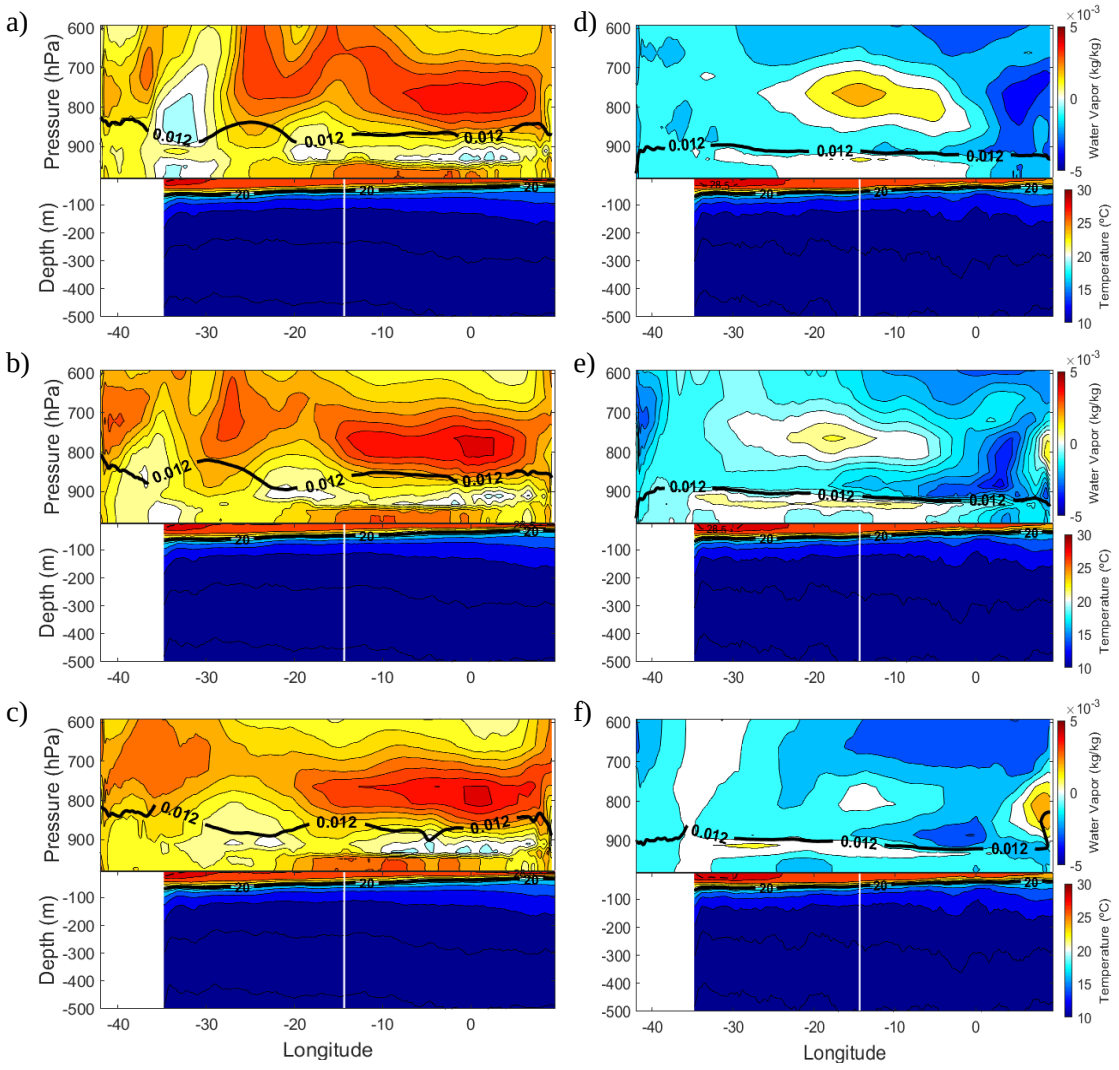

Source: The Author

Figure 43 – Longitudinal profile of atmospheric water vapor (upper panel), 10-days period average removed, and ocean temperature (bottom panel) from 14 (a), 15 (b), 16 (c) April 2011 and 30 (d) April, 01 (e) May, 02 (f) May 2011 at 00UTC. Isolines of 0.012kg / kg (upper panel, black line) and oceanic temperature (bottom panel, black line) with emphasis on the isotherm of 20 °C and 28.5°C.

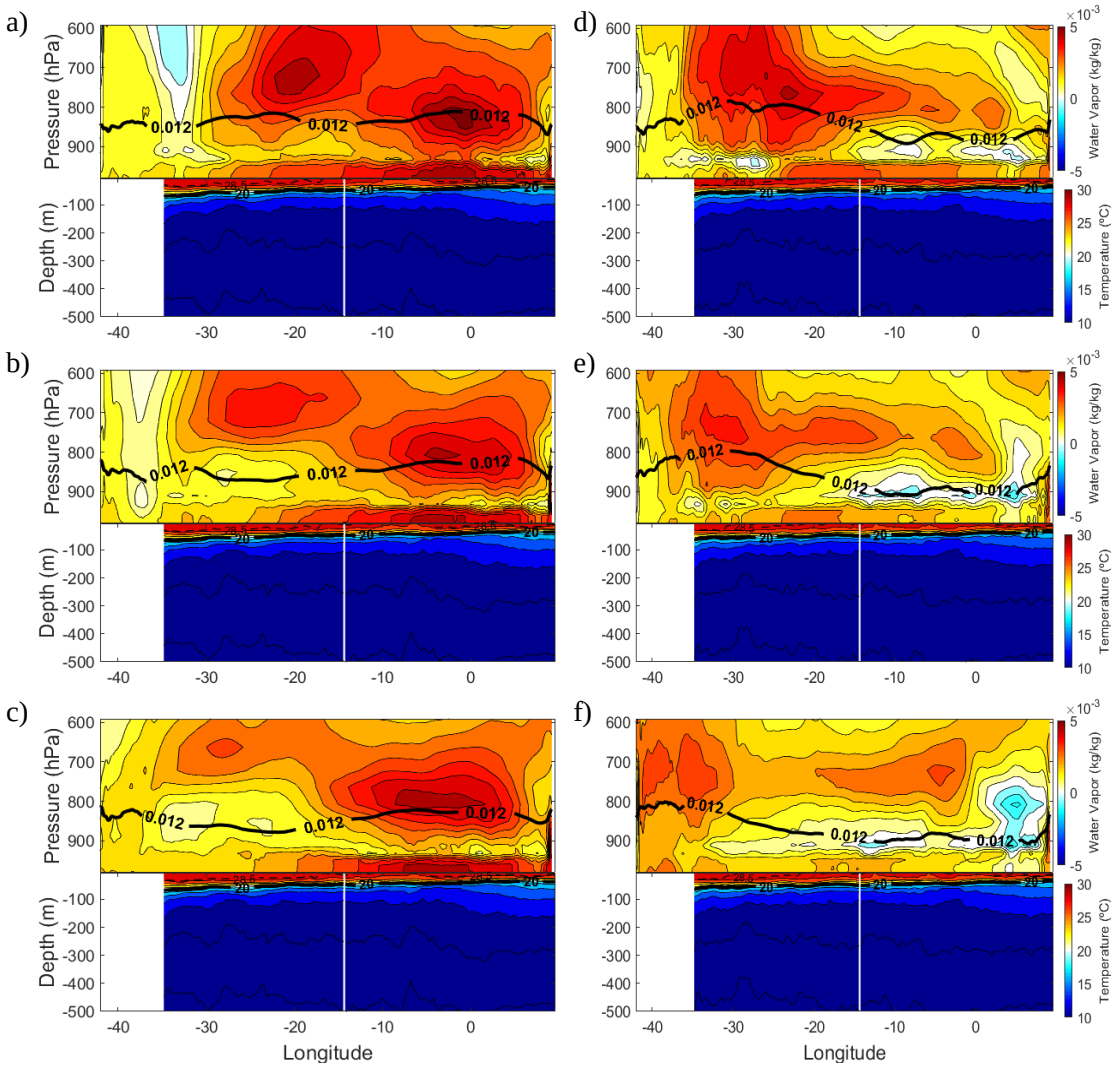

Source: The Author

Figure 44 – Longitudinal profile of atmospheric water vapor (upper panel), 10-days period average removed, and ocean temperature (bottom panel) for the maximum convection over ENEB region for 2012 (a), 2013 (b), 2014 (c) March 2015 (d), June 2015 (e), 2016 (f). Isolines of 0.012kg / kg (upper panel, black line) and oceanic temperature (bottom panel, black line) with emphasis on the isotherm of 20 °C and 28.5°C.

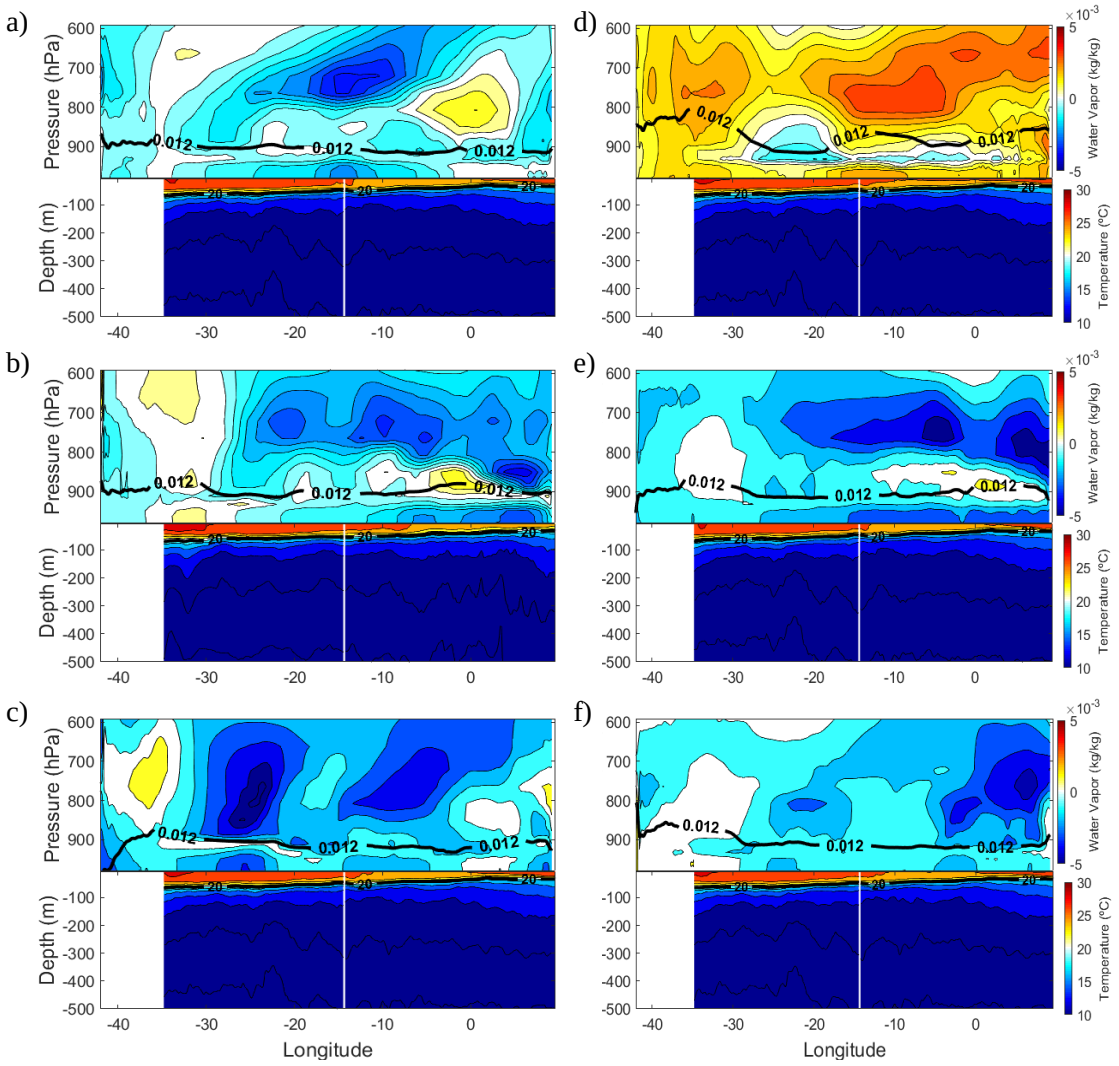

Source: The Author

not appear and negative anomalies of SST are observed, TWIL and lower MABL cause clouds to be lower, or even not to occur spontaneously.

However, in the presence of a meteorological system acting on the region, even on low SST conditions there is a supply of water vapor to medium atmosphere and intense precipitations can occur. It is noteworthy that the area of influence of SST seems to influence the comprehensiveness of the system, since in anomalously low SST the availability of water vapor at medium levels is restricted (WANG; ENFIELD, 2003), but deeper investigations must be made.

Also, it was observed that the EWDs that occurred in the period from February to April had more availability of water vapor than those in May, June and July. Also, it was observed that the EWDs that occurred in the period from February to April had more availability of water vapor than those in May, June and July. This behavior is related to the origin of the disturbances coming from the northeast (influenced by ITCZ), while the others, coming from southeast.

5 CONCLUSION AND PERSPECTIVES

The result shows that the coupled model has main influence from meteorological model and initial data. However, the coupling technique improve the surface fluxes and cause chain effects that will influence in rainfall simulations.

The initial data have an important factor to simulations. There is a need to investigate the best way and data to improve initial boundary conditions to better resolve the meteorological and oceanic patterns to improve the forecasting.

The benefit to use coupling technique was to influence in updating SST each 10 min over surfaces fluxes. These surface fluxes also influenced the forecasting of the others surface meteorological variables in a chain effect. Also, for oceanic modelling the better resolving of surface meteorological variables will improve the surface and mixed layer dynamics.

The modeling results evidenced that the heat and moisture fluxes in the western tropical South Atlantic were the main mechanism for the supplying of water vapor for the extreme events occurred in the ENEB, from June 10 to 25, 2010. The positive sea surface temperature anomalies in the SAWP region played an important role for the intensification of meteorological systems that caused extreme rainfall.

The easterly wave was intensified when crossing the region with the highest SST, that contributed to increase the vorticity between 850 and 700 hPa, leading to extreme rainfall event during 17 and 18 June.

The breakdown of the trade winds inversion occurred only under the presence of an atmospheric system over the SAWP.

The zone of thermal gradient in the central TSA, acted as a zone of disturbances development, that were transported by the trade winds, reaching the ENEB from 19 to 25 June.

As the MABL is advected across a strong SST gradient associated with the cold tongue, to warmer waters, substantial changes occur in the thermodynamic structure, surface fluxes, and cloud properties (Pyatt et al. 2005). As expected, in the experiments with sensible and latent fluxes, the warmest SSTs in the WSTA increased the height of MABL over SAWP and a lower MABL height was present over the “Cold Tongue” region, in the eastern STA.

In both simulations, with fluxes exchanges in the WRF and WRF-ROMS, the experiments with different boundary conditions, corroborated with the physical processes in the ocean-atmosphere interface. The most realistic results, comparing with in situ data, were those with FNL database, which showed better results in the water vapor content and accumulated rainfall in the period.

The continuous feedback of the heat and moisture exchange, and SST, in the coupled sim-

ulations increased the vertical motion over the SAWP, intensifying the water vapor convergence, as well as the total precipitation, that was near to the in-situ measurements.

The SAWP region acted to increase instabilities that caused extreme rainfalls. In first moment the high SST induced more LH flux which generates more buoyancy and providing moisture into MABL.

The instabilities generates ascendant vertical movements moistening the troposphere above the MABL. The increasing in wind speed caused the intense column water vapour transport to land provided by instabilities over the SAWP.

The result show that the positive anomalies of the SAWP region was the key factor to generate extreme precipitations episode over ENEB. These episode was intensified by warmer water over SAWP, similar to which occurs in other places of the Earth, some of them reaching to tropical storms such in Caribbean Sea.

Therefore, studies of ocean-atmosphere interaction in the TSA and its influences in the ENEB rainfall can be optimized with coupled models (ex. COAWST), as well as being an important tool for scenarios of climate change.

The prospects of this work are in the advancement of studies with a tool, that proved to be powerful, for simulations coupled between ocean and atmosphere. The advancement of technologies in computational mathematical resolution allows the use of massive systems of simultaneous physical solvers.

In this study only the superficial ocean and troposphere dynamics were used. However, as shown in the validation results, there are still gaps for improvements. One such improvement will be the use of three-way coupling with ROMS-WRF-SWAN. The SWAN coupled with the other two, has been showing improvements in surface winds due to friction of the surface winds and the ocean waves.

Another application will be in the operationalization of the COAWST in three-way coupling to forecast extreme events in the NEB. The model proved to be satisfactory with the examples shown here.

Because the coupled tool is relatively new, other horizons are open for investigation. The physical parameterizations are not appropriate among the three models, for example. As each model solves individually, it is the obligation of the researchers to improve the physical techniques that will solve the physical problems for the region of interest.

In addition, it was shown, in the idealized experiment, that the tool is also powerful for investigating events on different conditions of SST. In a climate change scenario, experiences can be realized with a model that has interaction at three levels, improving the results in adverse scenarios.

With the advent of computational power, improvements in simulations can also be

implemented. Because the ocean-atmosphere interaction is in small-scale, the higher resolution, will improve details and physical solutions. Today such conditions are limiting for studies with high resolution of coupled modeling.

For future work it is necessary to use the COAWST for the dry period. It is important to ascertain the skill of the model in the periods when the atmosphere is naturally drier, preferably using the techniques shown in the methodology of this work.

Another factor was the need for better detailing of oceanic data. Since the primary outcome is the input data, the better physical characterization of the oceans will improve the atmospheric results and vice versa.

The work showed that the interaction ocean atmosphere are linked from their climatology to "fast" weather systems, even with ocean being a fluid with "slow" thermodynamics. Therefore, it is essential to verify the oceanic influence in the all meteorological systems that occur throughout the NEB.

BIBLIOGRAPHY

ANDREOLI, R. V.; KAYANO, M. T. Tropical Pacific and South Atlantic Effects on Rainfall Variability Over Northeast Brazil. **International Journal of Climatology**, v. 26, n. May 2006, p. 1895 – 1912, 2006. Citado 2 vezes nas páginas 21 and 24.

____. A importância relativa do atlântico tropical sul e pacífico leste na variabilidade de precipitação do Nordeste do Brasil. **Revista Brasileira de Meteorologia**, v. 22, n. 1, p. 63–74, 2007. ISSN 0102-7786. Citado 2 vezes nas páginas 21 and 24.

ANTHES, R. A. **Regional Models of the Atmosphere in Middle Latitudes**. 1983. 1306–1335 p. Citado na página 43.

ANTHES, R. A. et al. Estimation of skill and uncertainty in regional numerical models. **Quarterly Journal of the Royal Meteorological Society**, v. 115, n. 488, p. 763–806, 1989. ISSN 1477870X. Citado 2 vezes nas páginas 42 and 43.

ARAGÃO, J. O. R. de. O Impacto do ENSO e do Dipolo do Atlântico no nordeste do Brasil. **Bulletin de I'Institut français d'études andines**, v. 27, n. 3, p. 839 – 844, 1998. Citado na página 21.

BERRY, G.; THORNCROFT, C.; HEWSON, T. African Easterly Waves during 2004—Analysis Using Objective Techniques. **Monthly Weather Review**, v. 135, p. 1251–1267, 2007. ISSN 0027-0644. Citado na página 30.

BIGG, G. R. et al. The role of the oceans in climate. **International Journal of Climatology**, v. 23, n. 10, p. 1127–1159, 2003. ISSN 08998418. Citado na página 31.

BOURRAS, D. et al. Response of the atmospheric boundary layer to a mesoscale oceanic eddy in the northeast Atlantic. **Journal of Geophysical Research Atmospheres**, v. 109, n. 18, p. 18114, 2004. ISSN 01480227. Citado na página 22.

BROWN, R. G.; ZHANG, C. Variability of Midtropospheric Moisture and Its Effect on Cloud-Top Height Distribution during TOGA COARE*. **Journal of the Atmospheric Sciences**, v. 54, n. 23, p. 2760–2774, 1997. ISSN 0022-4928. Citado 5 vezes nas páginas 22, 32, 66, 68, and 79.

BURPEE, R. W. **The Origin and Structure of Easterly Waves in the Lower Troposphere of North Africa**. 1972. 77–90 p. Citado na página 30.

CARLSON, T. N. Some remarks on African disturbances and their progress over the tropical Atlantic. **Monthly Weather Review**, v. 97, n. 10, p. 716–726, 1969. ISSN 0027-0644. Citado na página 30.

CARRILLO, J. et al. Characterization of the Marine Boundary Layer and the Trade-Wind Inversion over the Sub-tropical North Atlantic. **Boundary-Layer Meteorology**, Springer Netherlands, v. 158, n. 2, p. 311–330, 2015. ISSN 15731472. Citado 6 vezes nas páginas 22, 28, 61, 68, 79, and 83.

CAVALCANTI, E. P.; GANDU, A. W.; AZEVEDO, P. V. D. E. Transporte e balanço de vapor d'água atmosférico sobre o nordeste do brasil. **Revista Brasileira de Meteorologia**, v. 17, n. 2, p. 207–217, 2002. Citado 3 vezes nas páginas 21, 24, and 79.

CHAN, J.; DUAN, Y.; SHAY, L. Tropical cyclone intensity change from a simple ocean-atmosphere coupled model. **Journal of the Atmospheric Sciences**, v. 58, n. 2, p. 154–172, 2001. ISSN 0022-4928. Citado na página 32.

CHELTON, D. E.; XIE, S.-P. Coupled Ocean-Atmosphere Interaction at Oceanic Mesoscales. **Oceanography Magazine**, v. 23, n. 4, p. 52–69, 2010. Citado 3 vezes nas páginas 54, 68, and 79.

CINTRA, M. M. et al. Physical processes that drive the seasonal evolution of the Southwestern Tropical Atlantic Warm Pool. **Dynamics of Atmospheres and Oceans**, Elsevier B.V., v. 72, p. 1–11, 2015. ISSN 03770265. Citado 5 vezes nas páginas 21, 27, 57, 58, and 60.

CLEMENT, A. C.; SEAGER, R.; MURTUGUDDE, R. Why are there tropical warm pools? **Journal of Climate**, v. 18, n. 24, p. 5294–5311, 2005. ISSN 08948755. Citado 2 vezes nas páginas 31 and 32.

COUTINHO, E. D.; FISCH, G. Distúrbios ondulatórios de leste (dols) na região do centro de lançamento de alcantra-ma. **Revista Brasileira de Meteorologia**, v. 27, n. 2, p. 193–203, 2007. Citado 2 vezes nas páginas 31 and 33.

DAILEY, P. S. et al. On the relationship between North Atlantic sea surface temperatures and U.S. hurricane landfall risk. **Journal of Applied Meteorology and Climatology**, v. 48, n. 1, p. 111–129, 2009. ISSN 15588424. Citado na página 32.

DIEDHIOU, A. et al. over series over over over over circulatiøns aløng evident these panels ' Før the along IOøN) over Atlantic , a large. v. 25, n. 15, p. 2805–2808, 1998. Citado na página 30.

DIEDHIOU, A.; MACHADO, L. A. T.; LAURENT, H. Mean Kinematic Characteristics of Synoptic Easterly Disturbances over the Atlantic. **Advances in Atmospheric Sciences**, v. 27, n. 3, p. 483–499, 2010. Citado 2 vezes nas páginas 30 and 31.

DRUYAN, L. M.; FULAKEZA, M. The sensitivity of African easterly waves to eastern tropical Atlantic sea-surface temperatures. **Meteorology and Atmospheric Physics**, v. 113, n. 1, p. 39–53, 2011. ISSN 01777971. Citado na página 82.

FAIRALL, C. W. et al. Bulk parameterization of air-sea fluxes for Tropical Ocean-Global Atmosphere Coupled-Ocean Atmosphere Response Experiment. **Journal of Geophysical Research**, v. 101, n. C2, p. 3747, 1996. ISSN 0148-0227. Citado 3 vezes nas páginas 35, 41, and 46.

FEREIRA, A. G.; MELO, N. G. D. S. Principais sistemas atmosféricos atuantes sobre a região Nordeste do Brasil e a influência dos Oceanos. **Revista Brasileira de Climatologia**, v. 1, p. 15–28, 2005. ISSN 3554. Citado 2 vezes nas páginas 24 and 25.

FOLTZ, G. R.; MCPHADEN, M. J. The role of oceanic heat advection in the evolution of tropical North and South Atlantic SST anomalies. **Journal of Climate**, v. 19, n. 23, p. 6122–6138, 2006. ISSN 08948755. Citado 5 vezes nas páginas 21, 27, 57, 58, and 60.

FRANK, N. L. the "Inverted V" Cloud Pattern—an Easterly Wave? **Monthly Weather Review**, v. 97, n. 2, p. 130–140, 1969. ISSN 0027-0644. Citado na página 30.

GOMES, H. B. et al. Easterly Wave Disturbances over Northeast Brazil: An Observational Analysis. **Advances in Meteorology**, v. 2015, p. 1–20, 2015. ISSN 1687-9309. Citado 7 vezes nas páginas 21, 23, 24, 30, 31, 32, and 33.

GOPALAKRISHNAN, S. G. et al. Toward Improving High-Resolution Numerical Hurricane Forecasting: Influence of Model Horizontal Grid Resolution, Initialization, and Physics. **Weather and Forecasting**, v. 27, n. 3, p. 647–666, 2012. ISSN 0882-8156. Citado 2 vezes nas páginas 47 and 58.

GRAY, W. M. Global View of the Origin of Tropical Disturbances and Storms. **Monthly Weather Review**, v. 96, n. 10, p. 669–700, 1968. ISSN 0027-0644. Citado na página 23.

HAIDVOGEL, D. B. et al. Model evaluation experiments in the North Atlantic Basin: Simulations in nonlinear terrain-following coordinates. **Dynamics of Atmospheres and Oceans**, v. 32, n. 3-4, p. 239–281, 2000. ISSN 03770265. Citado na página 37.

HALLAK, R.; FILHO, A. J. P. Metodologia para análise de desempenho de simulações de sistemas convectivos na região metropolitana de São Paulo com o modelo ARPS: sensibilidade a variações com os esquemas de advecção e assimilação de dados. **Revista Brasileira de Meteorologia**, v. 26, n. 4, p. 591–608, 2011. ISSN 0102-7786. Citado na página 42.

HÄNSEL, S. et al. Assessing Homogeneity and Climate Variability of Temperature and Precipitation Series in the Capitals of North-Eastern Brazil. **Frontiers in Earth Science**, v. 4, n. March, p. 1–21, 2016. ISSN 2296-6463. Citado na página 21.

HASTENRATH, S. Exploring the climate problems of Brazil's Nordeste: A review. **Climatic Change**, v. 112, n. 2, p. 243–251, 2012. ISSN 01650009. Citado 2 vezes nas páginas 21 and 24.

HOLLOWAY, C. E.; NEELIN, J. D. Moisture Vertical Structure, Column Water Vapor, and Tropical Deep Convection. **Journal of the Atmospheric Sciences**, v. 66, n. 6, p. 1665–1683, 2009. ISSN 0022-4928. Citado 2 vezes nas páginas 66 and 79.

HONG, S.; LIM, J. **The WRF single-moment 6-class microphysics scheme (WSM6)**. 2006. 129–151 p. Citado na página 41.

HOUNSOU-GBO, G. A. et al. Tropical Atlantic Contributions to Strong Rainfall Variability Along the Northeast Brazilian Coast. **Advances in Meteorology**, v. 2015, p. 13, 2015. Citado 12 vezes nas páginas 21, 22, 24, 27, 32, 33, 57, 58, 60, 68, 83, and 84.

IACONO, M. J. et al. Radiative forcing by long-lived greenhouse gases: Calculations with the AER radiative transfer models. **Journal of Geophysical Research Atmospheres**, v. 113, n. 13, p. 1–8, 2008. ISSN 01480227. Citado na página 41.

JACOB, R. et al. M x n communication and parallel interpolation in ccsm3 using the model coupling toolkit. **Int. J. High Perf. Comp. App.**, v. 19, p. 293–308, 2005. Citado na página 33.

JOHNSON, R. H. et al. Trimodal Characteristics of Tropical Convection. **Journal of Climate**, v. 12, n. 1979, p. 2397–2418, 1999. Citado 3 vezes nas páginas 22, 23, and 28.

JONES, P. W. First- and Second-Order Conservative Remapping Schemes for Grids in Spherical Coordinates. **Monthly Weather Review**, v. 127, n. 9, p. 2204–2210, 1999. ISSN 0027-0644. Citado na página 34.

KAIN, J. S. The Kain–Fritsch Convective Parameterization: An Update. **Journal of Applied Meteorology**, v. 43, n. 1, p. 170–181, 2004. ISSN 0894-8763. Citado na página 41.

KAYANO, M. T. Low-level high-frequency modes in the Tropical Atlantic and their relation to precipitation in the equatorial South America. **Meteorology and Atmospheric Physics**, v. 276, p. 263–276, 2003. ISSN 01777971. Citado 2 vezes nas páginas 30 and 31.

KIRBY, J. T.; CHEN, T.-M. Surface waves on vertically sheared flows: Approximate dispersion relations. **Journal of Geophysical Research: Oceans**, v. 94, n. C1, p. 1013–1027, 1989. ISSN 2156-2202. Citado na página 35.

KLOESEL, K. a.; ALBRECHT, B. a. Low-Level Inversions over the Tropical Pacific—Thermodynamic Structure of the Boundary Layer and the Above-Inversion Moisture Structure. **Monthly Weather Review**, v. 117, n. 1, p. 87–101, 1989. ISSN 0027-0644. Citado na página 31.

KORACIN, D.; ROGERS, D. P. Numerical Simulation of the response of the marine atmosphere to ocean forcing. **Journal of Atmospheric Sciences**, v. 47, p. 592 – 611, 1990. Citado 2 vezes nas páginas 23 and 61.

KOUADIO, Y. K. et al. Heavy Rainfall Episodes in the Eastern Northeast Brazil Linked to Large-Scale Ocean-Atmosphere Conditions in the Tropical Atlantic. **Advances in Meteorology**, v. 2012, p. 1–16, 2012. ISSN 1687-9309. Citado 10 vezes nas páginas 21, 22, 23, 24, 27, 32, 33, 68, 83, and 84.

KOUSKY, V. E. Frontal Influences on Northeast Brazil. **Monthly Weather Review**, v. 107, n. 9, p. 1140–1153, 1979. ISSN 0027-0644. Citado 2 vezes nas páginas 24 and 31.

____. **Diurnal Rainfall Variation in Northeast Brazil**. 1980. 488–498 p. Citado 2 vezes nas páginas 24 and 31.

LARGE, W. G.; MCWILLIAMS, J. C.; DONEY, S. C. Oceanic vertical mixing _ a review and a model with a nonlocal boundary layer parameterization.pdf. **Reviews of Geophysics**, n. 94, p. 363–403, 1994. ISSN 8755-1209. Citado na página 38.

LI, Z.; PU, Z. Numerical Simulations of the Genesis of Typhoon Nuri (2008): Sensitivity to Initial Conditions and Implications for the Roles of Intense Convection and Moisture Conditions. **Weather and Forecasting**, v. 29, n. 6, p. 1402–1424, 2014. ISSN 0882-8156. Citado na página 58.

LINDZEN, R. S.; NIGAM, S. On the Role of Sea Surface Temperature Gradients in Forcing Low-Level Winds and Convergence in the Tropics. **Journal of Atmospheric Sciences**, v. 44, p. 2418 – 2436, 1987. Citado 5 vezes nas páginas 22, 23, 28, 61, and 78.

LIU, C.; ZIPSER, E. J. "Warm rain" in the tropics: Seasonal and regional distributions based on 9 yr of TRMM data. **Journal of Climate**, v. 22, n. 3, p. 767–779, 2009. ISSN 08948755. Citado 4 vezes nas páginas 28, 32, 85, and 87.

LUMPKIN, R.; GARZOLI, S. L. Near-surface circulation in the Tropical Atlantic Ocean. **Deep-Sea Research Part I: Oceanographic Research Papers**, v. 52, n. 3, p. 495–518, 2005. ISSN 09670637. Citado 2 vezes nas páginas 25 and 26.

LUTJEHARMS, J. R. E.; PENVEN, P.; ROY, C. Modelling the shear edge eddies of the southern Agulhas Current. **Continental Shelf Research**, v. 23, n. 11-13, p. 1099–1115, 2003. ISSN 02784343. Citado na página 37.

MA, L. M.; TAN, Z. M. Improving the behavior of the cumulus parameterization for tropical cyclone prediction: Convection trigger. **Atmospheric Research**, Elsevier B.V., v. 92, n. 2, p. 190–211, 2009. ISSN 01698095. Citado na página 41.

MACCREADY, P.; GEYER, W. R. Esturarine salt flux through an isohaline surface. **Journal of Geophysical Research**, v. 106, p. 11629 – 11637, 2001. Citado na página 37.

MARENGO, J. A. et al. Climatic characteristics of the 2010-2016 drought in the semiarid Northeast Brazil region. **Anais da Academia Brasileira de Ciências**, p. 1–13, 2017. ISSN 0001-3765. Citado 4 vezes nas páginas 21, 24, 40, and 74.

MOSCATI, M. C. d. L.; GAN, M. A. Rainfall variability in the rainy season of semiarid zone of northeast Brazil (NEB) and its relation to wind regime. **International Journal of Climatology**, v. 27, n. 4, p. 493–512, mar 2007. ISSN 08998418. Citado 2 vezes nas páginas 21 and 24.

MOURA, A. D.; SHUKLA, J. On the dynamics of droughts in Northeast Brazil: Observations, theory, and numerical experiments with a general circulation model. **Journal of Atmospheric Sciences**, v. 38, n. 12, p. 2653–2675, 1981. ISSN 0022-4928. Citado 2 vezes nas páginas 21 and 24.

MOURA, G. B. d. A. et al. Relação entre a precipitação do leste do Nordeste do Brasil e a temperatura dos oceanos. **Revista Brasileira de Engenharia Agrícola e Ambiental**, v. 13, n. 4, p. 462–469, 2009. ISSN 1807-1929. Citado 5 vezes nas páginas 21, 27, 32, 83, and 84.

NCEP. **NCEP FNL Operational Model Global Tropospheric Analyses, continuing from July 1999**. 2000. —- p. Disponível em: <http://rda.ucar.edu/datasets/ds083.2>. Citado na página 39.

NEVES, D.; ALCÂNTARA, C. R.; SOUZA, E. P. D. Estudo de Caso de um Distúrbio Ondulatório de Leste sobre o Estado do Rio Grande do Norte - Brasil Case Study of an Easterly Wave Disturbance Over Rio Grande do Norte State - Brazil. n. 1972, p. 490–505, 2016. Citado na página 30.

NOGUES-PAEGLE, J.; MO, K. Linkages between Summer Rainfall Variability over South America and Sea Surface Temperature Anomalies. **J. Climate**, v. 15, p. 1389–1407, 2002. Citado 2 vezes nas páginas 21 and 24.

PENG, S. et al. Detecting the structure of marine atmospheric boundary layer over the Northern South China Sea by shipboard GPS sondes. **Atmospheric Science Letters**, v. 17, n. 10, p. 564–568, 2016. ISSN 1530261X. Citado 3 vezes nas páginas 22, 31, and 77.

PENVEN, P. et al. Generation of cyclonic eddies by the Agulhas Current in the lee of the Agulhas Bank. **Geophysical Research Letters**, v. 28, n. 6, p. 1055–1058, 2001. ISSN 00948276. Citado na página 37.

____. Simulation of a coastal jet retention process using a barotropic model. **Oceanologica Acta**, v. 23, n. 5, p. 615–634, 2000. ISSN 03991784. Citado na página 37.

PYATT, H. E. et al. Evolution of Marine Atmospheric Boundary Layer Structure across the Cold Tongue – ITCZ Complex. **Journal of Climate**, p. 737–753, 2005. ISSN 0894-8755. Citado 4 vezes nas páginas 22, 23, 28, and 31.

RAMOS, R. P. L. Precipitation characteristics in the Northeast Brazil dry region. **Journal of Geophysical Research**, v. 80, n. 12, p. 1665–1678, 1975. ISSN 01480227. Citado 4 vezes nas páginas 21, 24, 83, and 85.

RAO, V. B.; LIMA, M. C.; FRANCHITO, S. H. Seasonal and Interannual Variations of Rainfall over Eastern Northeast Brazil. **Journal of Climate**, v. 6, n. 9, p. 1754–1763, sep 1993. ISSN 0894-8755. Citado 4 vezes nas páginas 21, 24, 31, and 40.

REED, R. J.; KLINKER, E.; HOLLINGSWORTH, A. The structure and characteristics of African easterly wave disturbances as determined from the ECMWF operational analysis/forecast system. **Meteorology and Atmospheric Physics**, v. 38, n. 1-2, p. 22–33, 1988. ISSN 01777971. Citado na página 30.

REED, R. J.; NORQUIST, D. C.; RECKER, E. E. The Structure and Properties of African Wave Disturbances as Observed During Phase III of GATE. **Monthly Weather Review**, v. 105, n. 3, p. 317–333, mar 1977. ISSN 0027-0644. Citado na página 30.

REED, R. J.; RECKER, E. E. Structure and Properties of Synoptic-Scale Wave Disturbances in the Equatorial Western Pacific. **Journal of the Atmospheric Sciences**, v. 28, n. 7, p. 1117–1133, 1971. ISSN 0022-4928. Citado na página 30.

RENAULT, L. et al. Coupled atmosphere-ocean-wave simulations of a storm event over the Gulf of Lion and Balearic Sea. **Journal of Geophysical Research: Oceans**, v. 117, n. 9, p. 1–25, 2012. ISSN 21699291. Citado 3 vezes nas páginas 23, 44, and 47.

ROBERTSON, A.; MECHOSO, C. Interannual and interdecadal variability of the South Atlantic Convergence Zone. **Monthly weather review**, p. 2947–2957, 2000. ISSN 0027-0644. Citado na página 24.

RODRIGUES, R. R. et al. The impacts of inter-El Niño variability on the tropical Atlantic and northeast Brazil climate. **Journal of Climate**, v. 24, n. 13, p. 3402–3422, 2011. ISSN 08948755. Citado 2 vezes nas páginas 21 and 24.

RODRIGUES, R. R.; ROTHSTEIN, L. M.; WIMBUSH, M. Seasonal Variability of the South Equatorial Current Bifurcation in the atlantic Ocean: A Numerical Study. **Journal of Physical Oceanography**, v. 37, n. 1, p. 16–30, 2007. ISSN 0022-3670. Citado na página 26.

SABIN, T. P.; BABU, C. A.; JOSEPH, P. V. SST-convection relation over tropical oceans. **International Journal of Climatology**, v. 33, n. 6, p. 1424–1435, 2013. ISSN 08998418. Citado na página 84.

SCHUBERT, W. H. et al. Dynamical Adjustment of the trade wind inversion layer. **Journal of Atmospheric Sciences**, v. 52, p. 2941 – 2952, 1995. Citado 7 vezes nas páginas 22, 23, 28, 32, 33, 61, and 78.

SERRA, Y. L.; KILADIS, G. N.; HODGES, K. I. Tracking and mean structure of easterly waves over the Intra-Americas Sea. **Journal of Climate**, v. 23, n. 18, p. 4823–4840, 2010. ISSN 08948755. Citado na página 30.

SERVAIN, J. et al. A Pilot Research Moored Array in the Tropical Atlantic (PIRATA). **Bulletin of the American Meteorological Society**, v. 79, p. 2019–2031, 1998. ISSN 00030007. Citado 3 vezes nas páginas 21, 39, and 74.

SHCHEPETKIN, A. F.; MCWILLIAMS, J. C. Quasi-Monotone Advection Schemes Based on Explicit Locally Adaptive Dissipation. **Monthly Weather Review**, v. 126, n. 6, p. 1541–1580, 1998. ISSN 0027-0644. Citado na página 37.

____. The regional oceanic modeling system (ROMS): A split-explicit, free-surface, topography-following-coordinate oceanic model. **Ocean Modelling**, v. 9, n. 4, p. 347–404, 2005. ISSN 14635003. Citado na página 37.

SHE, J.; KLINK, J. M. Flow near submarine canyons driven by constant winds. **Journal of Geophysical Research**, v. 105, n. C12, p. 28671 – 28694, 2000. Citado na página 37.

SILVA, T. L. d. V.; GUEDES, R. V. S. Análise do Comportamento Atmosférico em Situação de Seca: Uma abordagem Operacional para Pernambuco. **Revista Brasileira de Geografia Física**, v. 04, p. 937 – 950, 2012. ISSN 1984-2295. Citado 2 vezes nas páginas 21 and 84.

SKAMAROCK, W. et al. A Description of the Advanced Research WRF Version 3. **Technical Report**, n. June, p. 113, 2008. ISSN 1477870X. Citado 3 vezes nas páginas 36, 37, and 44.

STRAMMA, L.; ENGLAND, M. On The water masses and mean circulation of South Atlantic Ocean. **Journal of Geophysical Research**, v. 104, n. C9, p. 863 – 883, 1999. Citado 4 vezes nas páginas 9, 25, 26, and 27.

STRAMMA, L. et al. Upper ocean circulation in the western tropical Atlantic in boreal fall 2000. **Deep-Sea Research Part I: Oceanographic Research Papers**, v. 52, n. 2, p. 221–240, 2005. ISSN 09670637. Citado na página 25.

TAI, K.-S.; OGURA, Y. An Observational Study of Easterly Waves over the Eastern Pacific in the Northern Summer Using FGGE Data. **Journal of the Atmospheric Sciences**, v. 44, n. 2, p. 339–361, jan 1987. ISSN 0022-4928. Citado na página 30.

THORNCROFT, C.; HODGES, K. African easterly wave variability and its relationship to Atlantic tropical cyclone activity. **Journal of Climate**, v. 14, n. 6, p. 1166–1179, 2001. ISSN 08948755. Citado na página 30.

TORRES, R. R.; FERREIRA, N. J. Case Studies of Easterly Wave Disturbances over Northeast Brazil Using the Eta Model. **Weather and Forecasting**, v. 26, n. 2, p. 225–235, 2011. ISSN 0882-8156. Citado 4 vezes nas páginas 21, 24, 30, and 33.

TRENBERTH, K. E. Changes in precipitation with climate change. **Climate Research**, v. 47, n. 1-2, p. 123–138, 2011. ISSN 0936577X. Citado na página 31.

WALLCRAFT, A. J. et al. Value of bulk heat flux parameterizations for ocean SST prediction. **Journal of Marine Systems**, Elsevier B.V., v. 74, n. 1-2, p. 241–258, 2008. ISSN 09247963. Citado na página 39.

WANG, C.; ENFIELD, D. B. The tropical Western Hemisphere warm pool. **Geophysical Research Letters**, v. 28, n. 8, p. 1635–1638, 2001. Citado 9 vezes nas páginas 21, 22, 32, 57, 58, 60, 68, 77, and 86.

____. A Further Study of the Tropical Western Hemisphere Warm Pool. **Physical Oceanography**, v. 16, p. 1476–1493, 2003. Citado 2 vezes nas páginas 32 and 91.

WANG, C. et al. Influences of the Atlantic warm pool on western hemisphere summer rainfall and Atlantic hurricanes. **Journal of Climate**, v. 19, n. 12, p. 3011–3028, 2006. ISSN 08948755. Citado 5 vezes nas páginas 22, 57, 58, 60, and 68.

WANG, C.; LEE, S. K. Atlantic warm pool, Caribbean low-level jet, and their potential impact on Atlantic hurricanes. **Geophysical Research Letters**, v. 34, n. 2, p. 1–5, 2007. ISSN 00948276. Citado 6 vezes nas páginas 22, 32, 57, 58, 60, and 80.

WARNER, J. C. et al. Development of a Coupled Ocean–Atmosphere–Wave–Sediment Transport (COAWST) Modeling System. **Ocean Modelling**, v. 35, n. 3, p. 230–244, 2010. ISSN 14635003. Citado 7 vezes nas páginas 23, 33, 34, 35, 36, 41, and 44.

WARNER, J. C.; PERLIN, N.; SKYLLINGSTAD, E. D. Using the Model Coupling Toolkit to couple earth system models. **Environmental Modelling and Software**, v. 23, n. 10-11, p. 1240–1249, 2008. ISSN 13648152. Citado 3 vezes nas páginas 33, 34, and 44.

WARNER, J. C. et al. Development of a three-dimensional, regional, coupled wave, current, and sediment-transport model. **Computers & Geosciences**, v. 34, n. 10, p. 1284–1306, 2008. ISSN 00983004. Citado na página 44.

WILKS, D. S. **Statistical Methods in the Atmospheric Sciences**. [S.l.]: Academic Press, 2006. v. 91. 627 p. (International Geophysics Series, v. 91). Citado na página 43.

WILLMOTT, C. **Some comments on the evaluation of model performance**. 1982. 1309–1313 p. Citado na página 43.

YAMAZAKI, Y.; RAO, V. B. Tropical Cloudiness over the South Atlantic Ocean. **Journal of the Meteorological Society of Japan**, v. 55, n. 2, p. 205–207, 1977. Citado na página 30.

ZAMBON, J. B.; HE, R.; WARNER, J. C. Investigation of hurricane Ivan using the coupled ocean–atmosphere–wave–sediment transport (COAWST) model. **Ocean Dynamics**, v. 64, n. 11, p. 1535–1554, 2014. ISSN 16167228. Citado 3 vezes nas páginas 35, 44, and 46.

ZENG, X. B. et al. Marine Atmospheric Boundary Layer Height over the Eastern Pacific : Data Analysis and Model Evaluation. **Journal of Climate**, v. 17, n. 21, p. 4159–4170, 2004. ISSN 0894-8755. Citado 2 vezes nas páginas 22 and 31.